AN ABSTRACT OF THE DISSERTATION OF

Zhefu Wang for the degree of Doctor of Philosophy in Mechanical Engineering

Presented on July 16, 2008.

Title: Applications of the Thermal Wave Technique in Liquid Thermal Conductivity Measurements and Flow Field Diagnostics.

Abstract approved:_____

Richard B. Peterson

The thermal wave technique has been explored for the use of liquid thermal conductivity measurement and flow property diagnostics in this dissertation. For liquid thermal conductivity measurements, an experimental technique based on the thermal wave approach is developed. A stainless steel strip functions as both a heating element and a sealing cover for a chamber containing a test liquid. A periodic current passing through this metal strip generates a periodic Joule heating source. An infrared detector measures the temperature response at the front surface of the stainless steel strip. The phase and magnitude of the temperature response were measured by a lock-in amplifier at various frequencies. A one-dimensional, two-layered transient heat conduction model is developed to predict the temperature response. The phase information of this temperature response shows high sensitivity to the change of

thermal properties of the liquid layer and is employed to match experimental data to find the thermal properties of the test liquid. The measured thermal conductivities of water and ethylene glycol agree quite well with data from the literature and support the validity of this measurement technique. An aqueous fluid consisting of gold nanoparticles was also tested and anomalous thermal conductivity enhancement was observed. Our measurement results also showed a divergence of thermal transport behavior between nanofluids and pure liquids. This suggests a need to carefully examine the role of the measurement technique in the heat transfer experimental studies of nanofluids.

For the study of flow property diagnostics, a heat transfer system with a periodic boundary condition in a steady flow field is examined. Due to linearity and homogeneity of the heat transfer system under certain conditions, a thermal wave field generated by a periodic heating flux at the boundary of the flow field may be used to detect important flow field parameters, such as the velocity gradient at the wall, and therefore, the wall shear stress. A wall shear stress sensor design with a heater and two temperature sensors on a silicon dioxide substrate is analyzed. The heater with a periodic heating source generates an oscillating temperature field which interacts with the flow field. The temperature sensors pick up the temperature response that contains information on the velocity gradient at the wall. Based on the above sensor design, a two-dimensional conjugate heat convection model is developed with a periodic heating flux at the solid/fluid interface and a linear velocity profile in the fluid domain. Two designs are studied, one with a silicon heat sink under the silicon dioxide

substrate and another without the heat sink. The effects of the two main design parameters, the operating frequency and the distance between the heater and the temperature sensor, are discussed. A reasonable sensitivity of the phase information to the velocity gradient suggests a practical sensor design. A preliminary experimental test on a water channel flow has been conducted to support the concept of applying the thermal wave method to wall shear stress measurements.

Applications of the Thermal Wave Technique in Liquid Thermal Conductivity Measurements and Flow Field Diagnostics

by

Zhefu Wang

A DISSERTATION

submitted to

Oregon State University

in partial fulfillment of
the requirements for the
degree of

Doctor of Philosophy

Presented July 16, 2008
Commencement June 2009

Doctor of Philosophy dissertation of Zhefu Wang presented on July 16, 2008

APPROVED:

Major Professor, representing Mechanical Engineering

Head of the School of Mechanical, Industrial, and Manufacturing Engineering

Dean of the Graduate School

I understand that my dissertation will become part of the permanent collection of Oregon State University libraries. My signature below authorizes release of my dissertation to any reader upon request.

Zhefu Wang, Author

ACKNOWLEDGEMENTS

Firstly, I would like to thank my advisor, Dr. R. Peterson, for his guidance throughout my research, for his support during my study in OSU, and for his advise on organizing and writing this thesis.

Also, I want to thank my committee members, Dr. S. Apte, Dr. M. K. Drost, Dr. B. Paul, and Dr. T. Miller, whose inspiring questions about my research and many valuable suggestions significantly improved this research work.

This research was supported by the Oregon Nanoscience and Microtechnology Institute (ONAMI) and the Army Research Laboratory (ARL).

I thank all the friends and classmates in OSU. Special thanks to my personal friend, Jim Pearson, who helped improve my English for a long time.

Most of all, I thank my family which is the source of strength and courage all the time. I would like to dedicate this thesis to my family.

TABLE OF CONTENTS

TABLE OF CONTENTS (Continued)

Page

TABLE OF CONTENTS (Continued)

Page

LIST OF FIGURES

Figure: Page

LIST OF FIGURES (Continued)

LIST OF FIGURES (Continued)

LIST OF TABLES

NOMENCLATURE

A	parameter defined in equation 3.15
B	parameter defined in equation 3.16
c	velocity gradient
c_p	specific heat, J/kg·K
d	distance between the heater and the solid/fluid interface
g_0	volume heating source, W/m^3
i	complex number constant
k	thermal conductivity, W/m·K
l	distance between the heater and the sensor
q	surface heating flux, W/m^2
q_0	constant of the heating source
t	time, s
u	velocity component in the x direction, m/s
v	velocity component in the y direction, m/s
w	velocity component in the z direction, m/s
x	coordinate, m
y	coordinate, m
z	coordinate, m

G_0 parameter defined in equation 3.18

H height of the computation domain, m

L thickness of the layer or length of the computational domain, m

T temperature, °C

T_s thickness of the silicon dioxide layer

T_∞ ambient temperature

$\overline{T}$ dimensionless temperature

Greek

α thermal diffusivity, m^2/s

ρ density, kg/m^3

ψ phase, degree

ω frequency, radian

δ thickness of the heater

ξ parameter defined in equation 3.19 and 3.20

Subscript

0 constant of heat flux in equation 3.8

1 layer one or region one

2 layer two or region two

amp preamplifier

k thermal conductivity

m measured

mag magnitude of the temperature oscillation

ps power switch

s solid

v degree of freedom

new temporary temperature in equation 3.2

Superscript

* scale of dimension

¯ dimensionless mark

Applications of the Thermal Wave Technique in Liquid Thermal Conductivity Measurements and Flow Field Diagnostics

1. INTRODUCTION

This study exploits thermal wave approach for material thermal property determination and flow property diagnostics. A thermal wave is a heat transfer phenomenon describing how temperature oscillation propagates in the material domain and has been used to determine thermal properties of thin films in semiconductor devices historically [1~3]. This dissertation comprises two research projects: first one is development of an experimental technique capable of determining thermal conductivity of liquids with application to nanofluids; second is exploration of utilizing thermal wave approach for flow field measurement applications, such as flow diagnostics near surfaces and in microfluidic systems.

1.1 NANOFLUID THERMAL CONDUCTIVITY MEASUREMENTS

The global energy crisis necessitates new technology for more efficient utilization of current energy resources. Heat exchangers are key components in energy systems and the space for the improvement of heat transfer efficiency has attracted many researches over several decades to this area of study. Based on the basic heat

convection process in heat exchangers, the factors that determine the heat transfer efficiency can include the heat exchange surface area, the local temperature gradient, and the thermal conductivity of the heat transfer liquid.

Heat transfer within microchannels has been studied extensively [4] because of the large increase of the heat transfer surface area in the devices with microchannels. This is still a very active research area of heat and mass transfer enhancement. The local temperature gradient is the main topic of the classical theories about convection heat transfer and boiling heat transfer. Still, for many applications within the area of single phase heat convection, the low thermal conductivity of many common working fluids remains the bottleneck for improving heat transfer in heat exchangers.

Over one decade ago, a new class of heat transfer fluids emerge [5, 6], called nanofluid. This new type of fluid was reported to show an anomalous enhancement of the effective thermal conductivities compared to the base fluid and claimed to be the working fluid for the next generation heat transfer applications. Nanofluids are suspension flows with nanometer-scale (1 ~ 100 nm) particles or fibers dispersed in the base fluids. The base fluids include water, ethylene glycol, engine oil, etc. The particles include oxides, metals, carbon nanotubes, etc.

Heat transfer enhancement of particle flows can have multiple impacts on important engineering applications, for example, electronics cooling, miniaturized energy and chemical systems and process intensification. Impacts in the various economic sectors span from aerospace to automotive industry. However, previous work about particle flows with millimeter-to-micrometer sized particles had very limited

applications because of clogging problems, suspension stability, surface erosion, and compatibility with the pumping systems. Recently developed nanofluids appear to be able to overcome many of those drawbacks of the conventional suspension flows due to the extremely small particle size [7].

The classical theory of particle/fluid systems successfully describes the thermal transport process of composite systems with micrometer or larger particle sizes [8]. The composite system is treated as a homogeneous and isotropic material domain. The zero thermal resistance at the solid/liquid interfaces and no relative motion between liquid and particle are the two important assumptions. Then, the so-called effective thermal conductivity is introduced into the formula of Fourier's law. Although this theory fails to explain a nanofluid's apparent abnormal capability for transferring heat, the concept of effective thermal conductivity continues to be used in the experimental study of nanofluids. Most of these experimental studies use the effective thermal conductivity to define the enhancement level, as well.

In the experimental study of the effective thermal conductivities of nanofluids, several important issues remain. First, disagreement about the enhancement level of the effective thermal conductivities appears in the experimental results among different research teams [9, 10] and among different measurement techniques [11, 12]. Although anomalous enhancement was reported in most researches to date, other studies report findings in line with predicted thermal conductivity of nanofluids. Second, although the elements of heat transfer enhancement mechanisms in nanofluids were studied extensively, such as particle sizes, compositions, ingredients, and surfactants etc., the

role of the measurement techniques in the experimental studies has not been examined in detail. It would be desirable to have independent experimental techniques developed to provide new information about the thermal transport process of nanofluids and, therefore, help to explain the discrepancy among the measurement results.

The factors concerning the thermal conductivity measurement of nanofluids can be categorized into two groups. One concerns the material characteristics, such as thermal properties of base liquid and particles, volume fraction, particle size, surface treatment, etc. Another is about the processing parameters related to the experimental apparatus, such as temperature, temperature gradient, pressure and other parameters. The first class of factors has been studied extensively while only the temperature effect in the second class had been examined [11]. A natural question to ask is that given a well-characterized nanofluid, what will its effective thermal conductivity be? Is it a constant similar to a pure liquid, or could it be a function of temperature or temperature gradient? Other parameters may also enter into consideration of effective thermal conductivity. These questions will be important for building an empirical formula for effective thermal conductivity and expediting the process of nanofluid applications in heat transfer. Due to the close relationship between the processing parameters and the measurement results, data inconsistency problems mentioned above need to be studied with the processing parameters taken into account.

In light of the above discussion, a phase detection technique based on a thermal wave approach is developed to measure thermal conductivities of liquids with application of nanofluids. Special attention will be paid to the effect of the processing

parameters in the measurements. A periodic Joule heating source generated from a time-varying electrical current passing through a thin stainless steel strip produces a temperature fluctuation on the front surface of the stainless steel strip. An infrared detector monitors this temperature fluctuation on the front surface. This stainless steel strip also works as the front surface of the test cell that contains the nanofluids. The temperature signal is recorded by both an oscilloscope and a lock-in amplifier, the later of which gives magnitude and phase information about the signal. The validity of this measurement technique is assessed by using water and ethylene glycol. A gold nanolfuid with concentration of 0.058 g/L and average particle size of 4.5 nm is also tested. Resutls show anomalous enhancement of thermal conductivity. Our measurements suggest a potential relationship between the effective thermal conductivity of nanofluids and the temperature gradient by recording the measurement at different frequencies. This preliminary result indicates a need for further study of the effect of temperature gradients on the effective thermal conductivity using different measurement techniques.

1.2 WALL SHEAR STRESS MEASUREMENTS

Measurements of the wall shear stress are of both fundamental and practical importance. The wall shear stress is used to define the characteristic length and velocity scale of turbulent boundary layers. Furthermore, the structure of these boundary layers is described by these characteristic scales. For laminar flow, or low Reynolds number flow, separation control has become a very active research area and quantitative information concerning the wall shear stress is critical for determining flow patterns. It also contributes toward an understanding into the separation mechanisms, as well.

Boundary layer flow control, such as separation delay, lift enhancement, drag reduction, transition postponement, and vortex control of delta wings, is a broad area with great engineering significance. One of the most important inputs of these control schemes will be wall shear stress. Micro air/underwater vehicles are under development for both civilian and military applications. To achieve autonomous vehicle control, the reliable and accurate measurement of wall shear stress, or the velocity gradient on the airfoil, will be critical.

Direct and indirect methods are the two main categories of wall shear stress measurements. For the direct method, the shear stress acting on the sensor surface is directly converted to a physical signal that can be measured. The indirect method, in most cases, measures the flow velocity gradient at the wall using thermal, optical, or other signals. The information on the wall shear stress is then extracted from the primary data recorded.

Among the above measurement techniques, MEMS-based thermal sensors hold great potential and have attracted several research development efforts. The following focuses on MEMS-based thermal sensor techniques.

Thermal sensors in wall shear stress measurements has been based on the simple heat convection principle: assuming all the other conditions are the same, the temperature or the heat flux at the wall is a function of the flow velocity gradient at the wall, and, therefore, a function of the wall shear stress. By applying a constant heat flux to the wall or keeping a constant wall temperature, the correlation between the wall temperature amplitude and the wall shear stress can be deduced.

However, two main drawbacks prevent this kind of sensor from wider application [13]. First is the temperature drift problem. The assumption that all other conditions remain the same cannot hold in real-world measurements. The wall shear stress is very sensitive to the ambient temperature shift and this type of error cannot be easily corrected. Second, the supporting structure of the thermal sensor introduces complexity into the measurement. The compensation of the heat transfer interaction between the sensor and the support structure is very difficult.

Emerging micromachining techniques are thought to provide solutions for the above problems of thermal shear stress sensors. However, although the small time and length scale of MEMS-based sensors do improve the performance of shear stress measurements in terms of spatial and temporal resolution and sensitivity, fundamental limitations such as temperature drift are not resolved [13].

The basic principle of the phase-sensitive thermal sensor we propose here is: by imposing a periodic heating flux with a known frequency on the wall surface, the responding wall temperature signal at the same frequency will not be at the same phase as the heating signal. This phase shift will be a strong function of the flow velocity gradient on the wall when the heating signal is in a certain frequency range. As a whole, this heat transfer approach, including conduction in the substrate and convection in the flow, is a linear system. Therefore, the system transient response from unwanted perturbations, such as ambient temperature drift or the turbulence in the main stream, can be decoupled from the system frequency response of the periodic heating signal. This implies the temperature drift will no longer be a source of error because the absolute temperature value is not the indicator of the wall shear stress.

The small characteristic length and time scales corresponding to the exciting frequency suggest that the heat transfer interaction among the heating element, the substrate, and the flow field is limited to a small region and will have little effect on the wall shear stress value itself. Special designs, such as a vacuum cavity under the heating element to improve thermal insulation, may not be necessary. Another benefit of the design proposed here is that measurements of different wall shear stress magnitudes or different flow patterns, e.g. laminar or turbulent, can be accommodated by tuning the exciting frequency. Scaling analysis shows that the sensitivity of the measurement can be tailored by changing this excitation frequency.

In the study presented within this thesis, a two-dimensional conjugate heat convection model is developed with a periodic heating flux at the solid/liquid interface

and a linear velocity profile in the liquid domain. The complex combination method is employed to convert the governing equation and the boundary conditions from the time domain to the frequency domain. In this work, a wall shear stress sensor design with a heater and two temperature sensors on a silicon dioxide substrate is analyzed. The heater with a periodic heating source generates a temperature oscillation field which interacts with the flow field. The temperature sensors pick up the temperature response that contains the information on the velocity gradient at the wall. Based on the above sensor design, a two-dimensional conjugate heat convection model is developed with a periodic heating flux at the solid/fluid interface and a linear velocity profile in the fluid domain. The simulation results show that the temperature signal, especially the phase information, can be a strong function of the velocity gradient at the wall. Two designs are studied, one with a silicon heat sink under the silicon dioxide substrate and another without the heat sink. The effects of the two main design parameters, the operating frequency and the distance between the heater and the temperature sensor, are discussed. A reasonable sensitivity of the phase information to the velocity gradient suggests a practical sensor design.

A preliminary experimental test is conducted to prove the concept of utilizing the thermal wave for the measurement of the wall shear stress. A thin stainless steel strip adjacent to a flow field of a water channel flow is heated by a periodic current. Different mass flow rates in the channel lead to different velocity gradients on the surface of the stainless steel strip. The temperature signal at the other surface of the stainless steel strip is monitored by an infrared detector. The experimental results show a dependence of the

phase shift of the temperature signal on the mass flow rate. Due to the thin penetration depth of the thermal wave in our case, the results suggest that the phase information could be used for the measurement of the wall shear stress.

2. LITERATURE REVIEW

2.1 NANOFLUIDS THERMAL CONDUCTIVITY ENHANCEMENT

Nanofluids are composite fluid systems with nanometer scale (1 ~ 100 nm) particles or fibers dispersed in base fluids, such as water, ethylene glycol, engine oil, etc. The particles include oxides, metals, carbon nanotube, etc.

The potential heat transfer enhancement appears to be the driving force for the study of thermal transport properties of nanofluids over the last decade after the pioneering work of Masuda et al. [5]. The name "nanofluid" was first used by Choi [6]. Following these two seminal works, many studies of the anomalous effective thermal conductivity have been reported in the literature.

Up to the present, most of the experimental studies in this area are measurement of effective thermal conductivities of composite liquid systems; essentially nanofluids [9, 10, 14~18]. Meanwhile, other interesting thermal transport properties were reported in the literature, such as high critical heating flux in boiling heat transfer [19, 20], higher thermal conductivities at higher operating temperature [11, 21], and enhancement in forced convection [22, 23].

The classical theory of particle-fluid systems originally proposed by Maxwell [8] successfully described thermal transport process of the composite system with micrometer or larger-sized particles. One prediction from this theory is that the effective thermal conductivity shall be independent on the particle size. However, experimental studies of nanofluid thermal conductivity show that the particle size is strongly related

to the enhancement level [24]. More importantly, the effective thermal conductivity of nanofluids is far beyond the prediction of conventional theory [6, 9, 14~18].

Although the conventional theory fails to explain a nanofluid's abnormal capability for transferring heat, the concept of effective thermal conductivity continues to be used in the experimental studies of nanofluids. However, Vadasz [25] argued that this kind of effective thermal conductivity may not exist in a transient process, which is typical of current measurement techniques, especially the transient hot-wire method. By introducing a heat transfer coefficient at the solid-liquid interface, he suggested that the transient hot-wire method may tend to overestimate the measured thermal conductivity of a composite fluid. However, to date no experimental data is available to provide the value of the heat transfer coefficient at the solid-liquid interface to verify his theory.

Many theoretical works have been proposed to explain heat transport mechanisms of unusual enhancement in nanofluids. Some of them include: Brownian motion of the particles in the base liquid [26], the interfacial layer between the liquid and solid phase [27, 28], ballistic nature of heat transport due to the nanometer scale of the particle size [7], clustering of nanoparticles [29], and themophoretic effects [30]. Still, most of the studies about the enhancement mechanisms are limited in both theoretical approaches [25] and scaling analysis [7, 30]. Jang and Choi [26] proposed a microconvection mechanism which is based on the possibility that the Brownian motion of nanoparticles could improve the heat transfer coefficient between the base fluid and the particles. Also, Prasher et al. [31] conducted a scaling analysis of different possible mechanisms and suggested a similar conclusion – that the convection induced by the

Brownian motion is mainly responsible for the enhancement. More recently, Eapon et al. [32] reported the experimental results of silica nanofluids using the transient hot-wire method and found good agreement between the Maxwell mean-field model and his measurement results. He further claimed that the microconvection mechanism cannot be the source of the anomalous enhancement.

The past experimental studies of nanofluids reveal several fundamental issues. First, measurements from different groups and under different techniques generate inconsistent results although most of the studies claim abnormal increase of the effective thermal conductivity. Although anomalous enhancement was reported in most of the research work [6, 9, 11, 14~18, 21], some measurements still presented no unpredicted thermal conductivity of nanofluids [10, 12]. Zhang et al. (2006) [10] conducted experimental measurements of the effective thermal conductivity on several oxide nanofluids using the transient hot-wire method and the results were found to be in line with the prediction of the conventional model. Putnam et al. (2006) [12] used the optical deflection beam method for gold nanoparticle solutions and no anomalous enhancement of the effective thermal conductivity was reported. Second, the role of the measurement technique on experimental results has not been examined in detail. Vadasz [25] suggests that applying a measurement technique conventionally used for pure liquids to a composite liquid may lead to misinterpretation of experimental data.

2.2 MEASUREMENT TECHNIQUES IN NANOFLUID STUDIES

For the experimental study of the effective thermal conductivity of nanofluids, the majority of the experimental data reported so far are from the transient hot-wire method [9, 10, 14, 16~18], which is conventionally used to measure the thermal properties of pure liquids. Other measurement techniques found in the literature include the temperature oscillation technique [11], optical beam deflection method [12], and 3ω method [21].

The transient hot-wire method has been a standard technique for the measurement of the liquid thermal properties for a long time [33]. A system diagram of a typical transient hot-wire experimental apparatus is shown in Figure 2.1. For a line heating source in a semi-infinite material domain with a step input, the analytical solution of the temperature on the line source can be found as a function of time. The desired information on the thermal properties of the material domain, such as thermal conductivity and thermal diffusivity, can be derived from the relation between the temperature on the line heating source and the time. In the context of real measurements, assumptions and conditions need to be considered to ensure accurate measurement. First, the time range of the measurement has to be carefully determined to satisfy the semi-infinite material domain assumption. Second, researchers usually use a small diameter platinum wire as both the heating source and the temperature sensor to guarantee the validity of the line heating source assumption. Third, electric insulation issue needs to be considered carefully because of the high electric current in the experiment. To date, most of the experimental studies on the effective thermal

conductivity of nanofluids have used this technique [9, 10, 14, 16~18]. Among them, Murshed et al. [14] developed a double hot-wire method to determine both the thermal conductivity and thermal diffusivity.

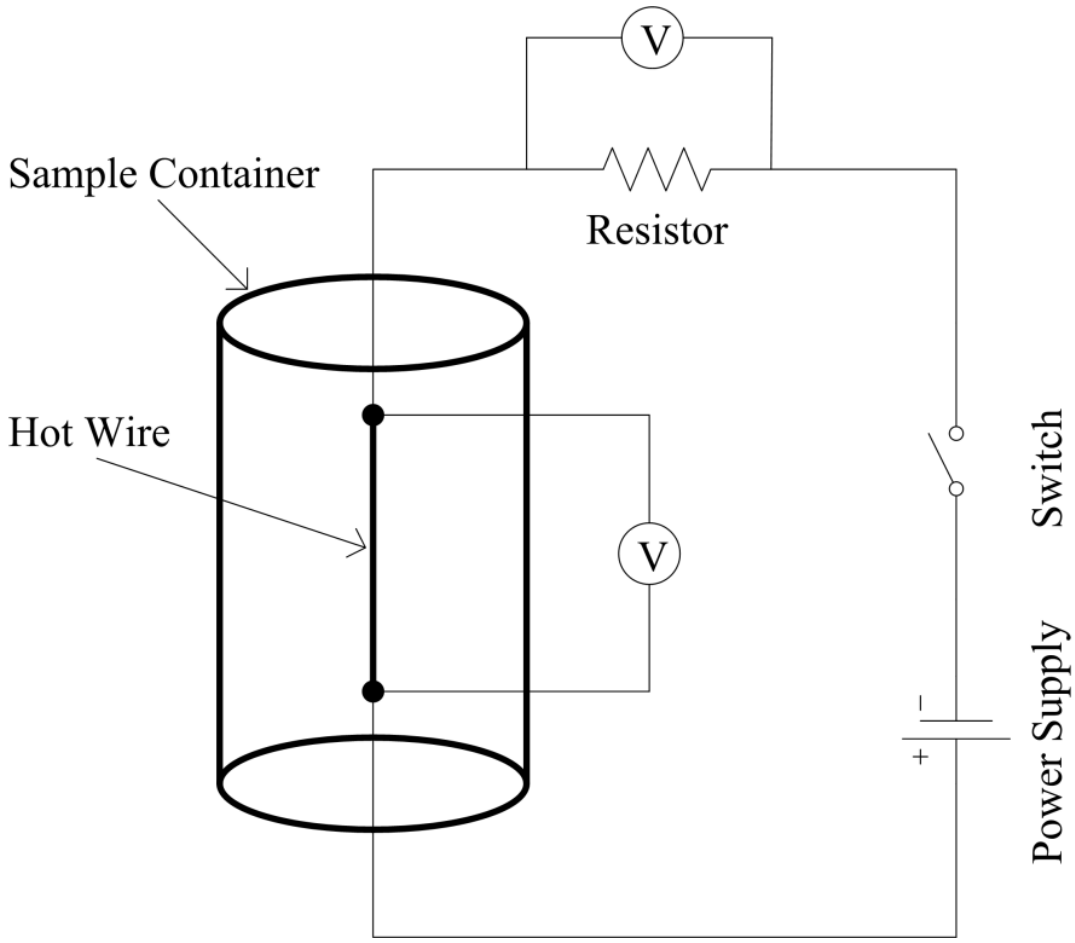

Figure 2.1: Schematic of a typical transient hot-wire experimental apparatus

Das et al. [11] used a so-called temperature oscillation technique to determine the thermal conductivity of nanofluids. Two parallel reference layers confined the testing liquid and Peltier elements on the external surfaces of the reference layers

provided the temperature fluctuation. The operating frequency of this temperature fluctuation is of the order of about 0.03 HZ and the space for the testing liquid is a cylindrical geometry with a diameter of 40 mm and a thickness of 8 mm. Although the formula of the thermal conductivity in terms of the measured temperatures was given in the paper, how the experimental data led to the results was not described in detail. For example, it was not clear whether the magnitude or the phase of the temperature fluctuation was used to calculate the effective thermal conductivity of the test fluid. Another issue was that the one-dimensional model in this work may not be valid because the penetration depth of the thermal wave was very large due to the low operating frequency and the edge effects of the test cell may have introduced significant error into the measurement.

The optical beam deflection method developed by Putnam and Cahill [34] was originally used for measurements of thermodiffusion in liquid mixtures. A pair of thin film line heaters generates an oscillating temperature field in the test liquid. The resultant gradient of the index of refraction deflects the laser beam which is normal to the test cell. The deflection angle measured was then used to match to the analytical model and determine the thermal conductivity of the test fluid. Suspensions of Au nanoparticles were tested and no anomalous enhancement of the thermal conductivity was found in this study [12].

Similar to the transient hot-wire method, the 3ω method has been extensively used in the characterization of material thermal properties [35~37]. This technique consists of a thin conductive wire embedded in a material domain and functions as both

a heater and a temperature sensor. In this method, a sinusoidal current with a frequency ω passes through the thin wire and generates a Joule heating source with a 2ω frequency component. A temperature fluctuation with a 2ω frequency induced from the Joule heating source leads to the resistance fluctuation of the heating wire which is at 2ω frequency also. At this point, a new voltage component with 3ω frequency results from multiplying of the current of ω frequency with the resistance fluctuation of 2ω frequency. This voltage with 3ω frequency can be measured and used to extract the information on the thermal properties of the material domain. Wang et al. [21] used this method to measure the thermal conductivity and thermal diffusivity of nanofluids with oxide particles. Their results show a temperature dependence of thermal conductivity enhancement.

2.3 THERMAL WAVE BASED MEASUREMENT TECHNIQUES

Because the measurement technique developed in this thesis is based on a basic heat transfer phenomenon called thermal wave [38], this section will introduce previous experimental studies that utilize thermal wave for determining material thermal properties.

The study of thermal properties of solid materials using the thermal wave principle can be traced back to Angstrom's method to measure the thermal diffusivity of metals [39]. Normally a periodic heating source in the material domain or a heating flux at a system boundary generates a temperature oscillation propagating into the material domain. The basic heat conduction equation is solved and the temperature signal can

then be matched to the solution to find the thermal properties of the sample. In most cases, both magnitude and phase information of the temperature signal are used. The key experimental instrument will be a lock-in amplifier which can measure the magnitude and phase shift of the temperature signal.

Characterization of thin film thermal properties attracted many researches from about thirty years ago due to thermal management issues in semiconductor devices. The thermal conductivities of thin films were demonstrated to be significantly different from that of bulk materials and measurement technique based on the thermal wave principle became a popular tool to explore thermal transport phenomena in micro/nano scale devices.

Studies of different thin film materials appear in the literatures, such as polymer [40], silicon nitride [1], silicon dioxide [2], gallium arsenide [3], diamond [41], etc. Chen et al. [3] reported a thermal wave technique that could determine the thermal diffusivity of thin films in both parallel and perpendicular directions. Their work proved that the interfaces and boundaries of thin films would cause the anisotropy of the thermal properties in thin films.

The heating sources of the experimental apparatus include the modulated surface heating laser [3, 40] and deposited metal thin film heater [2, 41, 42]. Yu et al. [43] studied different laser heating configurations in the thermal wave techniques: uniform illumination, a line, and a point were investigated. The conclusion was that the uniform illumination method tended to introduce error into the results due to the two-dimensional edge effect. They also suggested that the phase information would produce

more robust measurement results because of its independence of the thermal energy absorbed. Indermuehle and Peterson [2] deposited a thermally thin nichrome film on the dielectric sample film and the nichrome film functioned as the heating source of the thermal wave measurements.

The approaches of temperature sensing included microfabricated thin film resistance temperature sensors [1, 3, 41], infrared temperature detectors [2], and interferometric calorimetry [40]. Saenger [40] developed a measurement method in which the calorimeter as the substrate of the sample could be interferometrically reflected and provided the information on the thermal wave in the sample. The phase lag of the measured thermal wave was then used to determine the thermal properties of the sample. In the study of Indermuehle and Peterson, an infrared detector was employed to monitor the temperature response on the surface of the sample [2]. Operating frequencies up to 20 kHz was reported in this work. Zhang and Grigoropoulos [1] patterned a thin tungsten strip on the sample as the temperature sensor and three independent experimental methods were tested for the measurement of silicon nitride thin films. The temperature sensor in the work of Chen et al. [3] was a deposited gold thin film, about 100 nm thick, and it had two operating frequency ranges: less than 200 Hz for the parallel direction and 20 kHz to 90 kHz for the perpendicular direction.

2.4 WALL SHEAR STRESS MEASUREMENTS

Measurements of wall shear stress have broad technical applications in many areas, such as aerospace [44, 45], turbo machinery [46], industrial process control, micro air/under water vehicle [47, 48], and biomedical applications [49], to name just a few. Haritonidis [50] overviewed the measurement techniques for wall shear stress and more recent surveys in this area can be found in the works of Fernholz et al. [51] and, Naughton and Sheplak [13].

Direct and indirect methods are the two main categories of the wall shear stress measurements [50]. For the direct method, the shear stress acting on the sensor surface is directly converted to a physical signal that can be measured. An example is the floating element sensor. A floating mass supported by springs will be displaced by the integrated wall shear force and the displacement indicates the value of the wall shear stress [52]. The indirect method, in most cases, measures the flow velocity gradient at the wall using pressure, thermal, optical, or other signals. Then the information on the wall shear stress can be extracted. Some examples include oil-film interferometry, optical sensors, liquid crystal coatings, and thermal sensors.

Early wall shear stress measurement instrumentation includes the Preston tube and Stanton tube, which were both based on the Bernoulli's principle [53]. The flow decelerates at the front of the tube which is mounted on the wall and the corresponding pressure drop indicates the level of wall shear stress. For the Preston tube, the flow pattern needs to be determined beforehand to ensure reliable results of the wall shear stress [53]. For example, if the velocity profile at the location of the tube conforms to

the law of the wall, the pressure drop measured can be correlated to the wall shear stress. The Stanton tube can be considered as a Preston tube with a very small tube diameter and it normally operates in the linear region of the velocity profile [54, 55].

When an oil film is spread on a solid flat surface and its thickness is so thin that the gravity force and pressure gradient can be ignored, the thickness distribution of the oil film can be directly related to the wall shear stress. Using interferometry, the thickness distribution of the oil film can be determined and, then, the wall shear stress on the oil film surface will be derived. This is the basic principle of oil-film interferometry which is described in detail in the work of Tanner and Blows [56]. The liquid crystal coating method is similar to the oil-film technique. The unique response of the liquid crystal coating to the shear stress applied on it will lead to a change of the optical properties in the liquid crystal [13].

The optical laser-based wall shear stress sensor is said to provide the most accurate measurement results compared to other techniques up to now [13, 57]. A laser beam generates a diverging fringe pattern in the viscous sublayer of a boundary layer. When the seeding particles pass through this fringe pattern, the Doppler shift of scattered light by those particles will be measured and related to the velocity gradient inside the viscous sublayer. Its current drawback is that the density of seed particles tends to be low inside the viscous sublayer, especially in the turbulent boundary layer with high Reynolds number, and, therefore, the limited data rate will lead to unsteady measurements [57].

Thermal sensors in wall shear stress measurements is based on the simple heat convection: assuming all other conditions are kept the same, the temperature or the heat flux at the wall is a function of the flow velocity gradient at the wall, and, therefore, a function of the wall shear stress [13]. When a constant heat flux is applied to the wall or a constant wall temperature is kept at the wall, the correlation between the wall temperature magnitude and the wall shear stress can be found. By solving the governing equation with a linear velocity profile on the plate with an assumption of a thin thermal boundary layer, classical theory predicted that the heat rate removed by the flow is proportional to the 1/3-power of the velocity gradient [58]. More details about the thermal wall shear stress sensor will be discussed in the next section.

A recent study of wall shear stress sensors tries to reproduce the haircell design of animals, such as spiders, bats and fish, with microfabrication techniques [59]. A cantilever beam attached to a cilium-like polymer hair picks up the drag force from the flow field and transfers the force to a moment that acts on the base of the cantilever beam. A doped silicon strain gauge at the base of the cantilever beam is then used to measure the moment acting on the base. The wall shear stress can be determined from the measured drag force on the polymer haircell.

2.5 MEMS SHEAR STRESS SENSORS

Among the wall shear stress measurement techniques, MEMS-based sensors hold great potentials [13, 51] due to the miniaturization of the sensors using microfabrication technology. This development can improve dramatically the spatial

and temporal resolutions as well as the sensitivity of the measurement results. In this section, we will introduce the two types of MEMS-based sensors for wall shear stress measurements: float-element sensors and thermal sensors. Since our sensor design is based on a heat transfer phenomena, we will focus our discussion on MEMS-based thermal sensor.

As mentioned in the last section, the float element sensor transfers the shear stress acting on the sensor surface to a displacement by a four-tether [60, 61] or cantilever-beam structure [62]. Various tranducing mechanisms are employed to convert the displacement to an electrical signal, such as differential capacitance [62], piezoresistance [63, 64], and photodiode-based optical technique [65]. Although this kind of design is claimed to be easily contaminated by dust and moisture from the medium [44], some requirements from special flow features may make this sensor desirable. For example, Jiang et al. [62] developed a float-element sensor based on capacitive sensing for the measurement of low level shear stress because they found that hot-wire anemometry was not suitable for the particular flow features they were interested in [66]. Also, Barlian et al. [52] presented a floating element-based shear stress sensor for underwater applications. In this design, they used a four-tether floating element structure and a piezoresistance scheme for signal transduction.

Thermal MEMS wall shear stress sensor tends to be the promising candidate of the next generation sensor. It is claimed to be able to provide reliable quantitative information of wall shear stress and attracts many researches in the last decade [13]. A flexible shear-stress sensor skin based on heat transfer principle was developed by Xu et

al. [45] for the unmanned aerial vehicles. This sensor system was reported to successfully detect the flow separation along the leading edge of the airfoil in the real flight test. Soundararajan et al. [49] reported a study on the shear stress exerting on the lumen of the blood vessel which can closely regulate the biological activities of vascular endothelial cells. A thermal MEMS wall shear stress sensor was tested under low Reynolds number which is common in human microcirculation and the measurement results suggest the possibility of using this kind of sensor to directly measure the unsteady shear stress in the complicated arterial geometries.

Compared to the research of other sensor design, MEMS wall shear stress sensor based on heat transfer approach arouses many engineering interests due to its practical potential. Lin et al. [44] conducted both experimental and numerical studies on the thermal MEMS sensor and concluded that the 1/3 power law of the hot-film theory is not valid anymore because the thin thermal boundary layer will not exist for a MEMS thermal sensor. Chao et al. [67] discussed the effect of conjugate heat transfer on MEMS-based thermal shear stress sensor. Their numerical simulation demonstrates that the results of the shear stress measurements can be significantly distorted by the buoyancy effect because of the large operating temperature difference between the heating element and the medium.

Investigations of the sensor characterization can be found in the literature as well. Sheplak et al. [68] presented a detailed report about the static and dynamic characteristics of a thermal sensor with a vacuum cavity underneath the heating element. The effect of heat conduction interaction between the support substrate and the heating

element on the dynamic response was discussed. A recent work about thermal MEMS sensor characteristics was reported by Chandrasekaran et al. [69]. A dynamic calibration technique was developed using acoustic plane wave excitation for both the mean and fluctuating shear stresses. Xu et al. [70] reported characterization of a thermal shear stress sensor for underwater applications.

3. THEORY DERIVATION

In this chapter, the first section will introduce basic mathematical characteristics of the heat transfer governing equations and then present the heat transfer model which will govern the heat transfer phenomena of our study. Special focus is on the validity of applying the complex combination method to our governing equations. Section two extends the discussion of the governing equations to a scaling analysis. Section three presents an analytical solution of a one-dimensional, two-layered transient heat conduction problem, which is the theoretical basis of the principle of liquid thermal conductivity measurement in our study. The last section describes a numerical computation procedure for a two-dimensional conjugate heat transfer model with a periodic heat flux and a linear velocity profile, which reveals the operating principle of the wall shear stress measurement.

3.1. BASICS OF THE GOVERNING EQUATION

Flow fields with well-structured velocity profiles are very common in many science and technology applications and of engineering significance. For example, the universal law of the wall describes the structure of the turbulent boundary layer with finite wall shear stress. Due to the ultimate domination of the viscous force in the flow regime right next to the wall, a linear velocity gradient profile exists in the so-called viscous sublayer [71]. Another example concerns microfluidic technology. The small

channel size in microfluidic systems implies a low Reynolds number flow, and in turn the flow behavior can be well-defined. Here we are interested in a class of convection heat transfer problem with a periodic heating flux at the boundary of a steady flow field. Also, the fluid/thermal transport and thermodynamic properties are assumed to be independent of the temperature field in some narrow temperature range. This class of heat transfer phenomena could have extensive engineering applications, such as flow diagnostics near surfaces and in microfluidic systems.

Linearity and homogeneity are two important properties of the differential equations that govern heat transfer phenomena. Linearity means that the dependent variable in the differential equations or boundary conditions and its derivatives are of the first degree and the coefficient terms contain only the independent variables. When the dependent variable in the differential equation or boundary condition is multiplied by an arbitrary constant, the new differential equation or boundary condition will be identical to the original one after simple rearrangement. A differential equation or boundary condition satisfying these conditions is called homogeneous.

Linearity of the governing equations implies that superposition can be used to solve complicated heat transfer problems by separating the original problem into several simple subproblems [72]. The final solution can be synthesized by superimposing those solutions of the subproblems together. This will expedite the process of solving complex engineering problems and help identify the critical information in signal processing and data analysis.

Variation of parameters can be employed to solve heat conduction problems with periodic boundary conditions and source terms [72]. If the governing equations and boundary conditions are linear, the solution can be decoupled into two parts: a sustained part and a transient part. The transient part will approach a steady-state solution as time progresses and have no effect on the sustained part. Although this method can provide a complete solution, the process to obtain the whole solution is complicated. The so-called complex combination method is normally employed to find only the sustained solution if the transient part of the solution is of little engineering interest.

The complex combination method assumes the solution format based on the mathematical properties of the governing equation and the boundary conditions [72]. There are two conditions for using this method: the governing equation and the boundary conditions must be linear and the problem needs to be entirely homogeneous except for the periodic terms. A new problem in complex form is constructed to eliminate the transient term in the differential equation. Superposition is normally employed to ensure the condition of homogeneity by isolating the subproblem with only the periodic boundary condition from the whole problem.

Historically, the above theories and methods have been developed for heat conduction. The convection problems are far more complex due to the non-linear terms in the energy governing equations, such as the velocity term. However, in some simple flow patterns with constant thermal properties, the mathematical methods outlined above, such as superposition and complex combination, could be used to simplify this type of heat convection problem.

With no internal heat generation or viscous dissipation, the general three-dimensional convection heat transfer equation with constant thermal properties can be written as:

$$k\left(\frac{\partial^2 T}{\partial x^2}+\frac{\partial^2 T}{\partial y^2}+\frac{\partial^2 T}{\partial z^2}\right)=\rho c_p\left(\frac{\partial T}{\partial t}+u\frac{\partial T}{\partial x}+v\frac{\partial T}{\partial y}+w\frac{\partial T}{\partial z}\right) \tag{3.1}$$

where k is the thermal conductivity, c_p is the heat capacity, and ρ is the density of the liquid. All the material properties are assumed to be constant throughout this work. The variables $u=u(x,y,z)$, $v=v(x,y,z)$, and $w=w(x,y,z)$ are the velocity components in the x, y, and z directions respectively. The velocity components are functions of position only and independent of temperature and time. Therefore, the energy equation is decoupled from the known velocity field.

Since our goal is to explore the possibility of applying the complex combination method to convection, the simplest problem with an essential convection component will be addressed in this work. With the above linear governing equation, we assume that there is only one boundary condition which will be non-homogeneous, that of a pure sinusoidal function. Based on the above discussion, the complex combination method can be applied and the solution is assumed to have the following form:

$$T\left(x,y,z,t\right)=T_{new}\left(x,y,z\right)e^{i\omega t} \tag{3.2}$$

where ω is the frequency of the periodic boundary condition and i is the complex constant. Upon substituting Eq. (3.2) into Eq. (3.1), the differential equation can be written as:

$$k\left(\frac{\partial^2 T}{\partial x^2}+\frac{\partial^2 T}{\partial y^2}+\frac{\partial^2 T}{\partial z^2}\right)=\rho c_p\left(i\omega T+u\frac{\partial T}{\partial x}+v\frac{\partial T}{\partial y}+w\frac{\partial T}{\partial z}\right) \tag{3.3}$$

Note T_{new} is changed back to T again for simplicity because we will always deal with the complex T in the following development.

Eq. (3.3) is the new governing equation without the transient term and, instead, a complex source term replaces the time derivative of temperature. Compared to Eq. (3.1), this equation can yield to a numerical solution in a straightforward manner. Several points about this equation deserve our attention. First, the dependent variable – temperature, is a complex number, which contains both magnitude and phase information. Second, this equation is still linear and the solutions at different frequencies can be decoupled from one another. Third, the solution of the above equation will be only the sustained part of the total solution. In real engineering practice, the dynamic response of the system needs to be examined carefully because the temperature signal measured could contain some frequency components generated from the transient terms.

3.2. SCALING ANALYSIS

A scaling analysis can reduce the number of variables and parameters of the problem and provide insight into the physics of heat transfer phenomena. To explain the basic principle of this study, a two-dimensional flow field with a linear velocity profile

on a flat plate will be considered, as shown in Fig. 3.1. A periodic heat flux is applied on the wall between two specified x-locations.

The important assumptions of the flow field are: (*i*) the velocity component in the *y* direction, *v*, is zero; (*ii*) the velocity component in the *x* direction, *u*, is a linear function of y, or $u=cy$ with *c* as the velocity gradient and a constant value. The two-dimensional convection heat transfer governing equation of this flow field will be written as:

$$k\left(\frac{\partial^2 T}{\partial x^2}+\frac{\partial^2 T}{\partial y^2}\right)=\rho c_p\left(\frac{\partial T}{\partial t}+cy\frac{\partial T}{\partial x}\right) \tag{3.4}$$

The boundary conditions of this problem can be assumed to be homogeneous by setting the temperature or temperature gradient at the boundaries to zero except that at the heating area. Therefore, the complex combination method converts the governing equation to:

$$\alpha\left(\frac{\partial^2 T}{\partial x^2}+\frac{\partial^2 T}{\partial y^2}\right)=i\omega T+cy\frac{\partial T}{\partial x} \tag{3.5}$$

The first step of the scaling analysis is to normalize the differential equation. The scales of temperature, *x* length, and *y* length are marked with a star superscript and the normalized temperature, *x* length, and *y* length are designated with a bar:

$$T=T^*\overline{T}\,; \qquad x=x^*\overline{x}\,; \qquad y=y^*\overline{y}$$

Based on the conventional theory of the thermal wave method [72], the length scale can be chosen as the penetration depth of the thermal wave. This so-called penetration depth is developed in transient heat conduction analysis and is a

characteristic length that indicates how far the wave, or the temperature oscillations, travels before decaying to a negligible level.

$$x^* = y^* = \sqrt{\alpha/\omega} \tag{3.6}$$

The governing equation in the dimensionless form will become:

$$\frac{\partial^2 \overline{T}}{\partial \overline{x}^2} + \frac{\partial^2 \overline{T}}{\partial \overline{y}^2} = i\overline{T} + \frac{c}{\omega}\overline{y}\frac{\partial \overline{T}}{\partial \overline{x}} \tag{3.7}$$

A new non-dimensional number is found in Eq. (3.7), which is the ratio between the flow velocity gradient and the operating frequency. It is instructive to examine how different values of the non-dimensional number c/ω lead to different solutions.

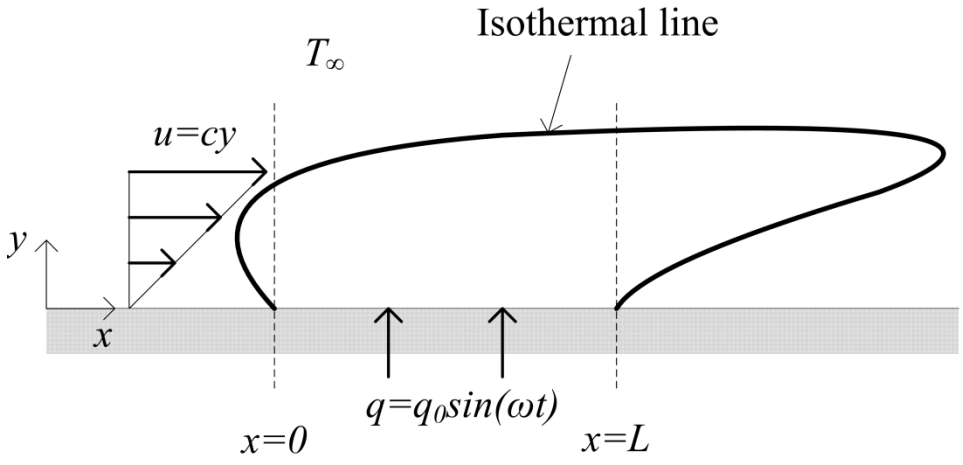

Figure 3.1: Schematic of scaling analysis

If c/ω approaches zero, the second term on the right side of the equation will vanish. The governing equation is reduced to the pure heat conduction model. In other words, under this situation, the system will not contain any information about the flow

velocity gradient c. When c/ω is much larger than unity, the complex term in the equation can be ignored and the governing equation will be approximated as the conventional heat convection model with a constant heat flux on the wall [73]. No phase information about the temperature signal will be present in the solution.

Only when c/ω is of the same order as unity will the system contain the information on both the complex term and the convection term. Therefore, the relationship between the velocity gradient and the temperature signal, especially the phase part, can be established. Another reasonable prediction will be that the temperature signal shall be more sensitive to change of the velocity gradient if the operating frequency is lower.

One important aspect of this heat transfer phenomena is the amplitude of the temperature signal. Scaling analysis about the heating flux boundary condition will be able to provide some insight about the temperature amplitude. For example, the heating flux boundary condition can be written as:

$$q = -k\frac{\partial T}{\partial y}\Big|_{x,y=0} = q_0 \sin(\omega t) \tag{3.8}$$

By substituting the penetration depth of thermal wave as our length scale into the above boundary condition equation, the scale for temperature is:

$$T^* = \frac{q_0}{k}\sqrt{\frac{\alpha}{\omega}} \tag{3.9}$$

The above formula suggests that the temperature amplitude decreases with the increase of the exciting frequency in a square root relation. This provides a guideline for

choosing the operating frequency and the magnitude of the heating flux in engineering design.

3.3. ANALYTICAL SOLUTION OF CONDUCTION PROBLEM

The phase detection measurement method employed here was modified from the phase-sensitive measurement technique for determining thermal properties of a dielectric thin film [2]. Figure 1 shows the principles of the thermal conductivity measurement of nanofluids.

This is a one-dimensional, two-layered transient heat conduction model with a periodic volume heating generation source in the first layer. The first layer will be the stainless steel strip with a thickness of 12.5 μm, and the substrate layer is the testing liquid, such as water, ethylene glycol, or nanofluids.

The important assumptions of this model include:

1. One-dimensional model only. Two-dimensional effect is neglected.
2. No convection occurs, pure conduction only.
3. The liquid substrate is modeled as semi-infinite solid domain.
4. The front surface of the stainless strip steel is assumed to be thermal insulted.
5. No thermal resistance between the stainless steel layer and the liquid substrate.
6. Constant thermal properties

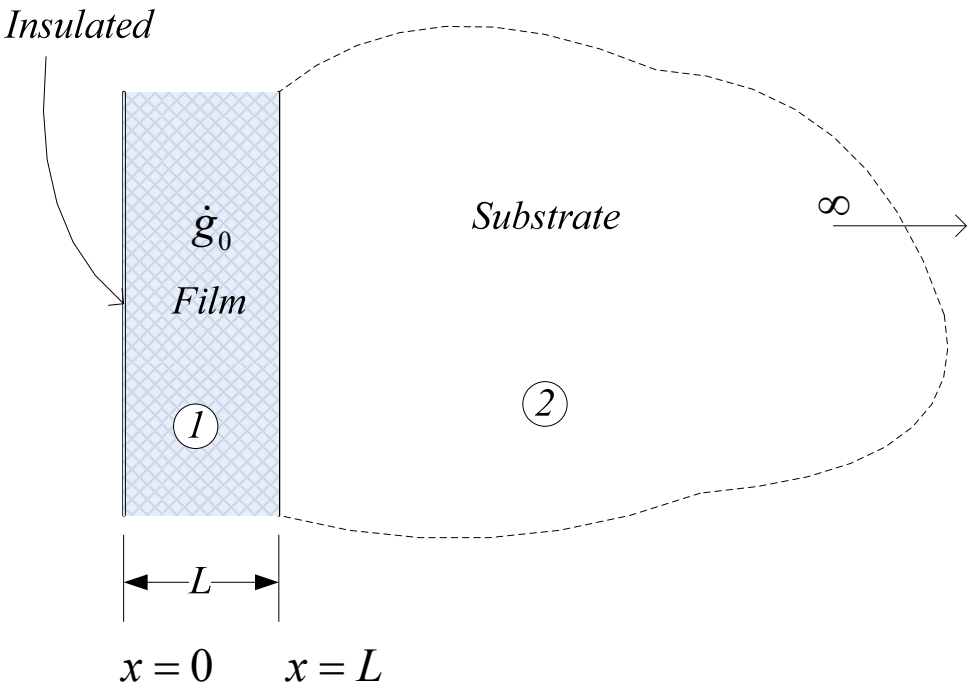

Figure 3.2: Principle of liquid thermal conductivity measurement

The governing differential equation for the first layer is

$$\frac{\partial^2 T_1}{\partial x^2} + \frac{g_0 \sin(\omega t)}{k} = \frac{1}{\alpha_1}\frac{\partial T_1}{\partial t} \tag{3.10}$$

And the governing equation for the second layer is:

$$\frac{\partial^2 T_2}{\partial x^2} = \frac{1}{\alpha_2}\frac{\partial T_2}{\partial t} \tag{3.11}$$

Assume that there is no thermal resistance between two layers and the solution is piecewise continuous. Both of the governing equations are linear and all the boundary

conditions are homogeneous except the heating source term. Therefore, using the method of complex combination, the solution format can be assumed as:

$$T(x,t) = \overline{T}(x)e^{i\omega t} \tag{3.12}$$

The analytical solution of the above differential equations can then be easily obtained because the partial differential equation is now converted to the ordinary differential equation. The complex form of the temperature expression of the heating layer, T_1, and that of the substrate layer, T_2, is shown in Eq. (3.13) and (3.14).

$$T_1(x,t) = \left(A_1 e^{-\xi_1 x} + B_1 e^{\xi_1 x} + G_0\right)e^{i\omega t} \tag{3.13}$$

$$T_2(x,t) = A_2 e^{-\xi_2 x} e^{i\omega t} \tag{3.14}$$

where:

$$A_1 = \frac{-G_0}{\left(e^{-\xi_1 L} + e^{\xi_1 L}\right) + \frac{k_1\xi_1}{k_2\xi_2}\left(e^{\xi_1 L} - e^{-\xi_1 L}\right)} \tag{3.15}$$

$$A_2 = \frac{k_1\xi_1\left(e^{-\xi_1 L} - e^{\xi_1 L}\right)}{k_2\xi_2 e^{-\xi_2 L}} A_1 \tag{3.16}$$

$$B_1 = A_1 \tag{3.17}$$

$$G_0 = \frac{\alpha_1 g_0}{i\omega k_1} \tag{3.18}$$

$$\xi_1 = \sqrt{i\frac{\omega}{\alpha_1}} \tag{3.19}$$

$$\xi_2 = \sqrt{i\frac{\omega}{\alpha_2}} \tag{3.20}$$

Substituting the above defined parameters into the temperature expression of the heating layer, the temperature at the front surface of this heating layer in the complex form can be expressed as:

$$T_1\left(x=0,t\right)=e^{i\omega t}G_0\left(1-\frac{2}{\left(e^{-\xi_1 L}+e^{\xi_1 L}\right)+\frac{k_1\xi_1}{k_2\xi_2}\left(e^{\xi_1 L}-e^{-\xi_1 L}\right)}\right) \tag{3.21}$$

In the form of real number, the temperature signal on the front surface of the stainless steel strip can be written as:

$$T_1\left(x=0,t\right)=T_{mag}\sin\left(\omega t+\psi\right) \tag{3.22}$$

Where T_{mag} is the magnitude of this temperature oscillation, and ψ is the phase shift between the heating signal and the above temperature signal. A curve of the magnitude and phase shift under various frequencies can be obtained from the model developed above, which will be shown in Chapter Four.

By slightly varying the thermal conductivity of the testing liquid in the model, the sensitivities of both magnitude and phase of the temperature signal to the thermal conductivity of the testing liquid can be found. The simulation result shows that the phase of the temperature signal is very sensitive to the change of thermal conductivity of the testing liquid, for example, 20% thermal conductivity enhancement corresponds to 0.8 to 1.2 degree of phase shift. However, the sensitivity of the magnitude is so low that it is not practical to use the magnitude signal to detect the thermal conductivity enhancement. Therefore, only the phase information will be used to predict thermal

conductivity enhancement in the discussion below. The magnitude will be employed to test whether our model matches the experimental data or not.

The linearity of our model needs to be examined carefully before the experimental apparatus design. As the above analysis shows, the heating source term in the model is a perfect sinusoidal function. However, the Joule heating source in the experiment is a positive going square wave, not an ideal sinusoidal wave which oscillates around zero. This implies that the heating source term can be decomposed into the DC and AC components. Further, the AC component in form of a square wave can be written as a series summation of harmonic sinusoidal functions according to Fourier's expansion,

$$g(t)=\frac{g_0}{2}+\sum_{k=1}^{\infty}\frac{2g_0}{(2k-1)\pi}\sin\left[(2k-1)\omega t\right] \tag{3.23}$$

Because of the linear nature of our heat conduction model, the solution also can be decomposed into AC and DC parts corresponding to the AC and DC heating source components. The DC part of the solution is the steady-state solution of the heat conduction problem with a constant heating source. It can be used to estimate the maximum temperature difference between the heating strip and the surrounding fluid and has no effect on the AC part of the solution. Each harmonic sinusoidal function in the AC part of the heating source term leads to a solution at the same frequency as shown in Eq. (3.23). The sum of these solutions at different frequencies comprises the AC part of the final solution. Because the solutions at different frequencies can be decoupled from one and another, we will focus on the solution at fundamental frequency

only and explore the relationship between the temperature signal and thermal properties of the liquid.

3.4. NUMERICAL SOLUTION OF CONVECTION PROBLEM:

In this section, the standard finite difference method is employed to solve a two-dimensional conjugate heat transfer problem with a periodic heating flux on the solid surface and a linear velocity profile in the flow field. The reason to study this heat transfer phenomena is that this configuration reveals the basic physics of heat transfer mechanism for most of the thermal wall shear stress sensor design. By imposing a periodic heating flux with a known frequency on the wall surface, the responding wall temperature signal at the same frequency will not be at the same phase of the heating signal. This phase shift is a strong function of the flow velocity gradient on the wall when the heating signal is in a certain frequency range and can be employed to determine the flow velocity gradient at the wall, and therefore the wall shear stress.

This computation domain is divided into two regions, as shown in Figure 3.3. Region one is the solid domain and region two is the liquid domain with a linear velocity profile. The heating source is a surface heating flux at the interface of the two regions.

As discussed in Section 3.1, the method of complex combination can be employed to simplify the particular partial differential equation. The region one is the solid domain and the governing equation is a heat conduction equation, as shown in Eq.

(3.24). The region two is the liquid flow domain with a linear velocity profile, as shown in Eq. (3.25).

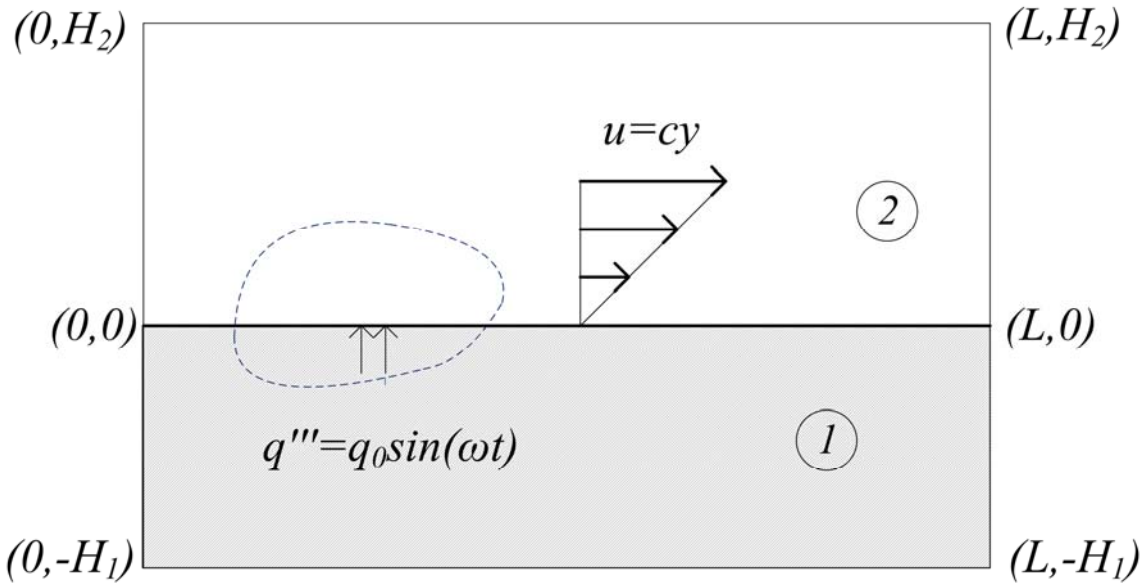

Figure 3.3.: Schematic of conjugate heat transfer model

For region one:

$$\alpha_1\left(\frac{\partial^2 T}{\partial x^2}+\frac{\partial^2 T}{\partial y^2}\right)=i\omega T \tag{3.24}$$

For region two:

$$\alpha_2\left(\frac{\partial^2 T}{\partial x^2}+\frac{\partial^2 T}{\partial y^2}\right)=i\omega T+cy\frac{\partial T}{\partial x} \tag{3.25}$$

The dimensions of the computational domain, L and H, are placed distant enough from the heating source so that the temperature signal near the boundaries

decays to zero. The temperatures at the boundaries of the computation are all set to zero except that there is a heating source at the interface of the solid and fluid domains.

$$T\Big|_{x=L,y} = T\Big|_{x=0,y} = T\Big|_{x,y=0} = T\Big|_{x,y=H} = 0 \tag{3.26}$$

The heating source is applied at the section between L_1 and L_2 on the interface and can be expressed as:

$$q = -k\frac{\partial T}{\partial y}\Big|_{x=L_1 \sim L_2, y=0} = q_0 \sin(\omega t) \tag{3.29}$$

Because of the linearity of this heat transfer system, both the heat conduction in the solid domain and the heat convection in the fluid domain, the discussions about decoupling in Section 3.2 are still valid. Again, the steady-state solution of this heat convection problem, or the DC part of the solution, will have no effect on the AC part of the solution. Each harmonic sinusoidal item in the AC part of the solution will be independent from one another. Therefore, we will focus on the solution at fundamental frequency only and explore the relationship between the temperature signal and the velocity gradient of the liquid flow.

The standard finite difference discretization scheme is employed to discretize the computation domain. As the governing equations show, the second derivatives of temperature T with respect to x and y, and the first derivative of temperature T with respect to x need to be discretized. Eq. (3.30) and (3.31) are the standard finite difference approximation of the second derivatives of temperature T with respect of x and y. Eq. (3.32) shows the first derivative of temperature T with respect to x. With these approximations of derivatives in terms of differences, the discretized governing

equations for the fluid and solid domain can be constructed. Also, in order to improve the computation efficiency, the step sizes in the y direction of the solid and liquid domain are set differently. For example, if the fluid domain is air and the solid domain is silicon dioxide, the large difference of thermal diffusivities will cause different thermal penetration depth in the solid and fluid domain. If the same grid size were employed for different material domain, large computation space will be wasted due to mismatch of the thermal properties.

$$\frac{\partial^2 T}{\partial x^2} \approx \frac{T_{x+\Delta x,y} + T_{x-\Delta x,y} - 2T_{x,y}}{\Delta x^2} \tag{3.30}$$

$$\frac{\partial^2 T}{\partial y^2} \approx \frac{T_{x,y+\Delta y} + T_{x,y-\Delta y} - 2T_{x,y}}{\Delta y^2} \tag{3.31}$$

$$\frac{\partial T}{\partial x} \approx \frac{T_{x+\Delta x,y} - T_{x-\Delta x,y}}{\Delta x} \tag{3.32}$$

The nodes at the solid/liquid interface need special attention. Figure 3.4 illustrates how the discretization of an interface node (x,y) is expressed from the energy balance of the cell (x,y). The upper half of the cell (x,y) is assigned to be the liquid domain and the lower half is the solid domain.

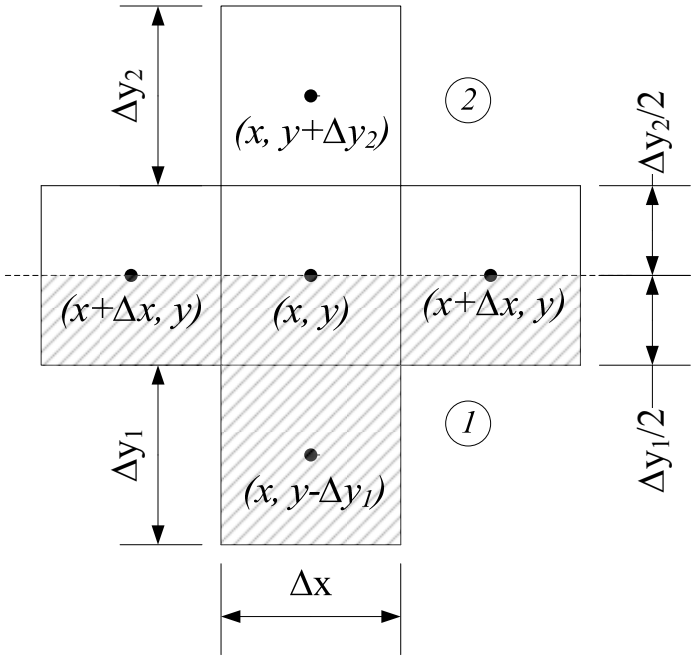

Figure 3.4: Schematic of the interface nodes and cells in conjugate heat transfer model

Eq. (3.33) shows the energy conservation governing equation of the interface cell (x, y). In the x direction, the mean thermal properties are adopted for those interface cells. In the y direction, the different thermal properties are assigned to the different material domains. The right hand side of the equation is the change of the energy stored in the cell (x,y) and the left hand side is the amount of the energy transferred from the adjacent cells. Because there is no velocity component in the y direction and the velocity component in the x direction is zero on the wall, no convection term will appear in the governing equation of the interface cell.

$$\left[\left(\rho c_p\right)_1 \Delta x \frac{\Delta y_1}{2} + \left(\rho c_p\right)_2 \Delta x \frac{\Delta y_2}{2}\right]\left(i\omega T_{x,y}\right)$$
$$= \left(k_m \left.\frac{\partial T}{\partial x}\right|_{x+\Delta x,y} - k_m \left.\frac{\partial T}{\partial x}\right|_{x,y}\right)\frac{\Delta y_1 + \Delta y_2}{2} + \left(k_2 \left.\frac{\partial T}{\partial y}\right|_{x,y+\Delta x} - k_1 \left.\frac{\partial T}{\partial y}\right|_{x,y}\right)\Delta x \tag{3.33}$$

A heating source term is added to the governing equation for the nodes with the heating flux, as shown in Eq. (3.34). The location of the heating flux can be right on the interface or a few micrometers below the interface.

$$k_1\left(\frac{\partial^2 T_{x,y}}{\partial x^2} + \frac{\partial^2 T_{x,y}}{\partial y^2}\right) + g_0 = \left(\rho c_p\right)_1 i\omega T_{x,y} \tag{3.34}$$

4. LIQUID THERMAL CONDUCTIVITY MEASUREMENTS

This chapter describes an experimental technique based on the thermal wave approach for the measurement of liquid thermal conductivity. A periodic current passing through a thin stainless steel strip generates a periodic Joule heating source adjacent to a liquid layer. An infrared detector measures the temperature response at the front surface of the stainless steel strip. The phase and magnitude of the temperature response were measured by a lock-in amplifier at various frequencies from 22 to 502 Hz. A one-dimensional, two-layered transient heat conduction model was developed to predict the temperature response on the front surface of the stainless steel strip, as shown in Chapter 3. The phase information of this temperature response shows high sensitivity to the change of thermal properties of the liquid layer and is employed to match experimental data to find the thermal properties. The measured thermal conductivities of water and ethylene glycol agreed well with data from the literature and supported the validity of this measurement technique. An aqueous fluid consisting of gold nanoparticles was tested and anomalous thermal conductivity enhancement is observed. The first section of this chapter outlines the experimental details of this study. Section 4.2 reports the test results of the standard reference liquids and a nanofluid. The last section in the chapter presents the uncertainty analysis of our experiments.

4.1 EXPERIMENTAL SETTING

4.1.1 Test Cell Preparation

The test cell holds the liquid being measured. The cell is constructed by machining an open chamber (10×6×1.5 mm) into the front surface of a piece of delrin plate (35×20×10 mm), as shown in Figure 4.1. A stainless steel strip (30 mm×8 mm×12.5 μm) is adhesively bonded onto the delrin surface through use of a transfer tape. This strip covers the open side of the chamber. The metal strip works as both the heating element and the sealing surface of the test cell. Two small copper bars are soldered on the two ends of the strip to reduce the electric noise and the contact resistance between this heating strip and the contact pad. Two small stainless steel tubes connect the chamber to the outside supply lines for liquid purging and refill. A polycarbonate plate covers the stainless steel strip for protection. The sample mounting arrangement is the same as that in reference [2] except that the specimen is replaced by the test cell.

Figure 4.2 shows the electric resistance of the stainless steel strip used in the experiment. The measured resistance is 0.418 Ω.

This low electrical resistance has several effects on our measurement systems. First, a large current of up to 2 Amp is needed to deliver a heating effect high enough to make the temperature oscillation detectable. A MOSFET-based power switch combined with the power supply and the TTL trigger signal is developed to accommodate the requirement of high current, as shown in Figure 4.3. Second, the low voltage across the

heating strip due to the low resistance prohibits the direct sampling of the heating voltage signal as the reference signal to the lock-in amplifier. Also, the power switch introduces some phase shift into the measurements which needs to be compensated by other additional measurements.

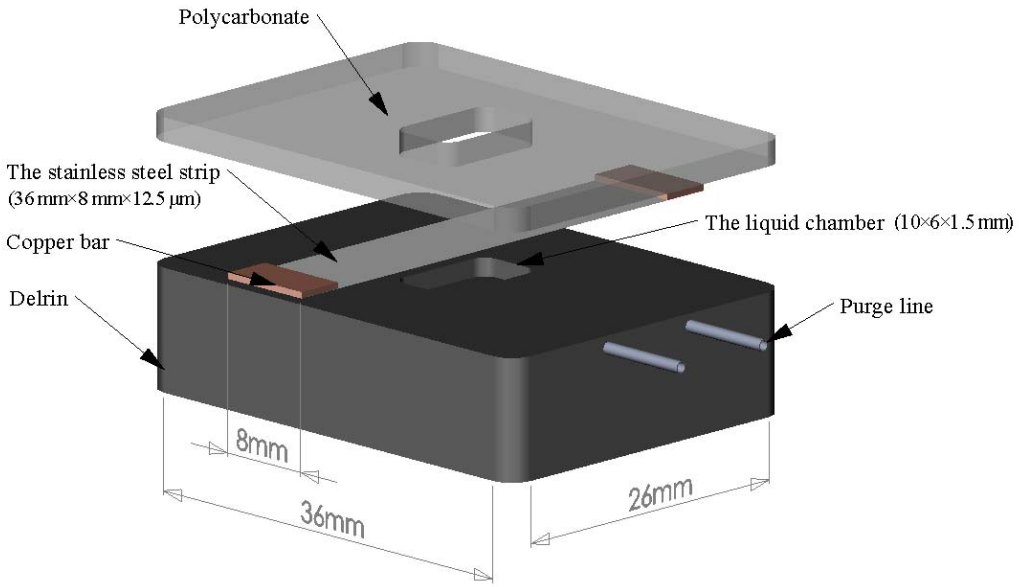

Figure 4.1: Test cell design – liquid thermal conductivity measurement

4.1.2 Apparatus

The instrumentation diagram for the experiment is shown in Figure 4.4, which can be divided into three sections: electrical heating, temperature sensing, and signal processing sections.

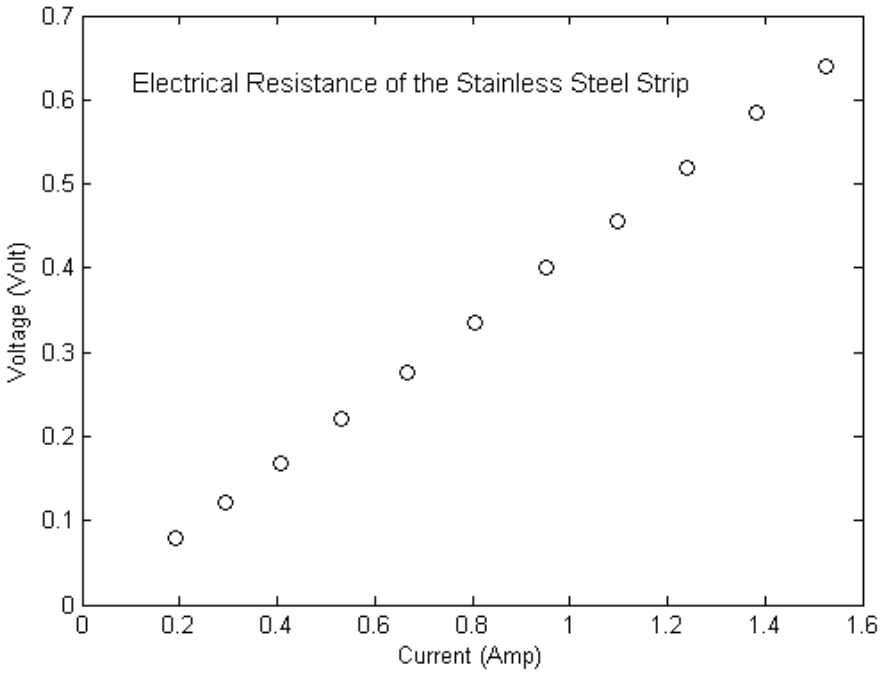

Figure 4.2: Resistance of the stainless steel strip – liquid thermal conductivity measurement

A periodic Joule heating source is generated by a periodic current passing through the stainless steel strip. This periodic current is provided by the MOSFET-based power switch, as shown in Figure 4.3. The TTL square waveform from the lock-in amplifier (Stanford research systems Model SR830) is the trigger signal to the MOSFET, while the programmable power supply (Tek Model PS2520G) provides a constant voltage to the power switch. With this design, a very clear voltage square waveform up to 500 Hz can be obtained across the stainless steel strip as viewed by an oscilloscope.

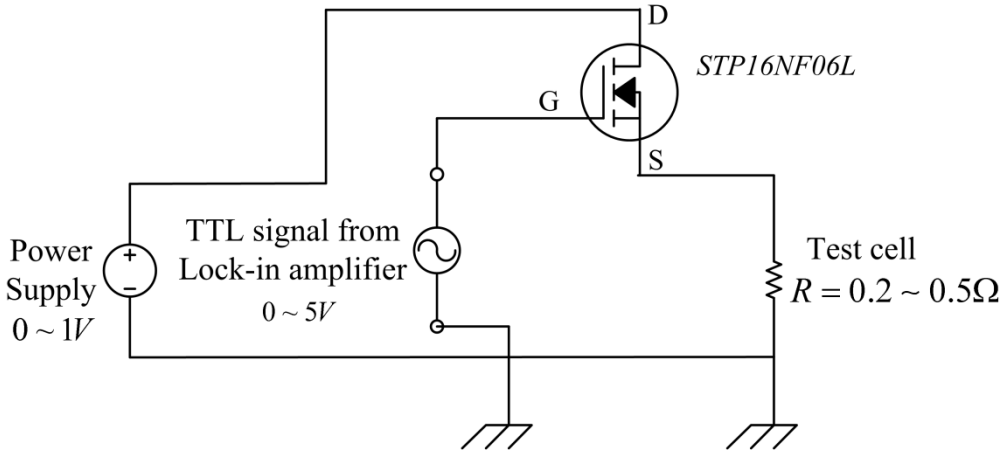

Figure 4.3: Diagram of the power switch – liquid thermal conductivity measurement

This periodic heating source in the metal strip causes the temperature oscillation on the front surface of the strip, which in turn leads to an oscillating thermal radiation signal. A Zinc Selenide infrared lens (Janos Technology Model A1200-012) focuses this oscillating thermal radiation signal onto an infrared detector (EG&G Judson Model J15D12-M204-S01M). With a bias current circuit, this Mercury Cadmium Telluride (HgCdTe) photoconductive detector converts the absorbed infrared radiation energy into a small voltage signal. Then, a low noise voltage preamplifier (EG&G Judson Model PA-101) increases the signal strength by a factor of 100 or 1000, depending on the setting. The resulting voltage signal is supplied to the lock-in amplifier for further signal processing. Note that the preamplifier filters out the DC component so that the lock-in amplifier receives an AC signal only.

The signal processing section includes the lock-in amplifier, an oscilloscope (Tek Model TDS220), and a Labview workstation. The lock-in amplifier and the oscilloscope

are connected to the Labview workstation through a GPIB bus for data logging. There are two separate paths to record and process the temperature signals here. The first is to use the lock-in amplifier to record the magnitude and phase shift of the temperature signal as input with respect to the TTL trigger signal as reference. The second uses the oscilloscope to record the time-varying waveforms of the temperature signal. The recorded data is then sent to the Labview workstation for further analysis.

4.1.3 Assumption Discussion

In the process of designing the test cell and measurement apparatus, consideration of several basic assumptions was important to ensure reliable measurement data.

First, the pure conduction assumption implies no natural convection inside and outside of the liquid chamber. As shown in Section 3.1, the heating signal can be decomposed into the DC and AC components and can be solved separately. The DC component of the heating source will lead to a steady state solution which can be easily found in a classical textbook [74]. Based on the given electrical current in our experiment and the electrical resistance of the heating strip, the total heating flux can be determined. The volume heating source term can then be obtained from the geometry of the heating strip and the above total heating flux. Simple steady-state heat conduction analysis in this case can be solved and the maximum temperature difference between the stainless steel strip and the surrounding fluid can be determined: it is approximately 8 °C. Note that this is the solution that considers heat conduction only. More study will be required to justify

the pure conduction assumption by calculating the natural convection heat transfer coefficient with the above given temperature difference and the geometry of the liquid chamber.

For natural convection with our geometry, a Rayleigh number less than 1000 implies primarily conduction heat transfer [74]. The formula of the Rayleigh number can be expressed as:

$$Ra_L \equiv \frac{g\beta(T_1-T_2)L^3}{\alpha\nu} \tag{4.1}$$

where L is the characteristic length, β is the volume thermal expansion coefficient, (T_1-T_2) is the temperature difference in the geometry, ν is the kinematic viscosity, and α is the thermal diffusivity of the liquid. With the characteristic length L of 1.5 mm for natural convection in a cavity and a temperature difference of 8 °C, the Rayleigh number calculated is about 439. Therefore, the natural convection component is small and the heat transfer mechanism can be approximated as pure conduction.

Second, in order to ensure that the semi-infinite material domain assumption applies, the thickness of the chamber needs to be much larger than the penetration depth of the thermal wave in our experiment [72]. The expression of the thermal wave penetration depth d_p is:

$$d_p = \sqrt{\frac{\alpha}{\omega}} \tag{4.2}$$

Where α is the thermal diffusivity of the liquid and ω is the operating frequency. According to our estimation with water as the test liquid, for example, the lower

frequency limit is set to 50 Hz, we decide the thickness of the liquid chamber to be 1.5 mm.

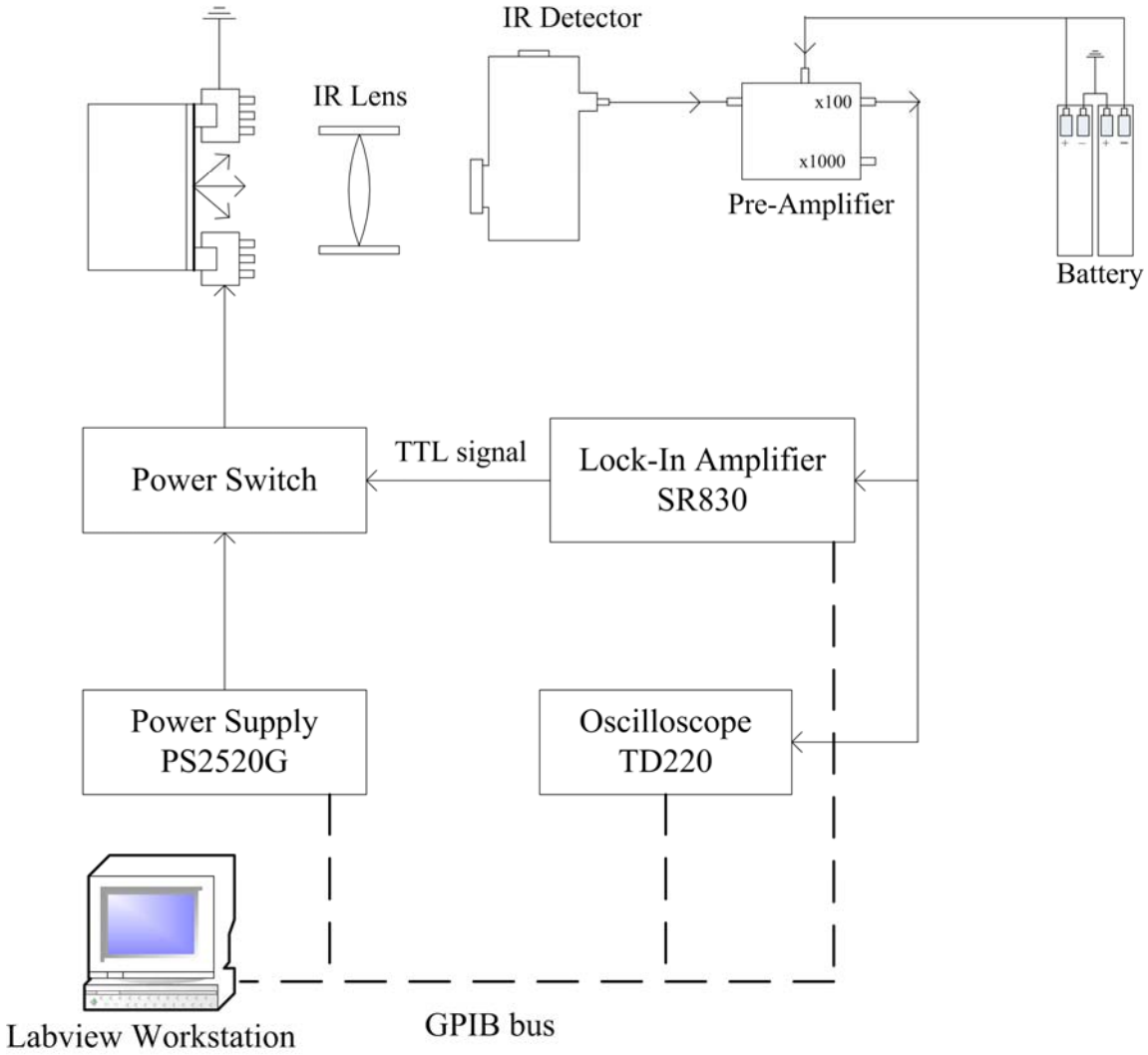

Figure 4.4: Apparatus schematic – liquid thermal conductivity measurement

Third, because the stainless steel strip is adhesively attached to the delrin support structure at its edge, this edge effect may invalidate our one-dimensional assumption and suggests a wider strip. However, a wider stainless steel strip lowers the electric

resistance. The electric resistance of the heating element needs to be high enough to secure a detectable temperature signal at the front surface of the stainless steel strip. Compromise between the above two considerations suggests a width of approximately 6 mm. Note that higher frequencies are favorable to the assumption of one-dimensional heat transfer. Low frequencies are where two-dimensional effects will emerge.

Also, during measurements, an acceptable point for acquiring the signal is located by matching the measurement to the model at a frequency within the measurement range. The alignment of the test cell, the infrared lens, and the infrared detector is achieved first by finding the strongest signal strength of the temperature response on the front surface of the stainless steel strip. After this, the positions of the infrared lens and detector will not be modified. The position of the test cell is adjusted to match the measured phase information to the model prediction. Then this measurement location is fixed through all other measurements. This process is validated using two independent test liquids.

4.1.4 Signal Path Analysis

One important issue that needs to be addressed is the signal transducing path. As shown in Section 4.1.2, the TTL trigger signal from the lock-in amplifier leads to the heating signal through the power switch. Then the temperature signal, in the form of radiation energy caused by the periodic heating source, is detected by the infrared detector and converted to a low-level voltage AC signal. A pre-amplifier boosts the low

voltage signal to a level compatible with the lock-in amplifier. Figure 4.5 shows the signal path of the experimental apparatus.

However, there are two factors that prevent the direct measurement of the phase difference between the heating signal and the temperature signal using the lock-in amplifier. The first is the temperature signal and its radiative nature in our experiment. The temperature signal is in the form of infrared radiation and needs to be converted to an electrical signal, such as a voltage signal, and this electrical signal must be compatible to the lock-in amplifier. The conversion may introduce some additional phase shift into the measurements. Second, the low signal strength and the high noise level of the heating signal precludes a direct use as the reference input to the lock-in amplifier as mentioned above.

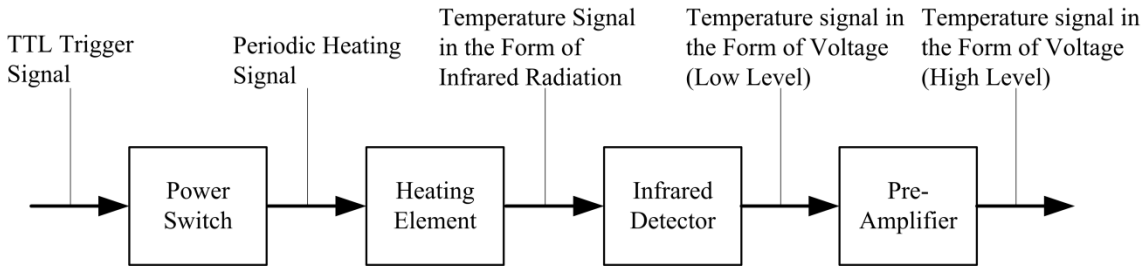

Figure 4.5: Schematic of the signal path – liquid thermal conductivity measurement

With the above considerations of the signal transducing path, the first step in the measurement process is to find the total phase shift of the signal path with respect to the TTL signal as reference and the pre-amplifier output as the signal input to the lock-in amplifier. After this, two compensation phase shifts need to be determined. One is the

phase difference between the TTL signal and the heating signal, which is caused by the power switch and can be directly measured. The other is the phase difference between the pre-amplifier output and the temperature signal, which is caused by the pre-amplifier and can be estimated from the electronic diagram of the pre-amplifier. Therefore, combining the above total phase shift and the two compensation phase differences together, the phase shift between the heating signal and the temperature signal can be determined. The phase shift data in the following Results section are all adjusted according to the above procedure.

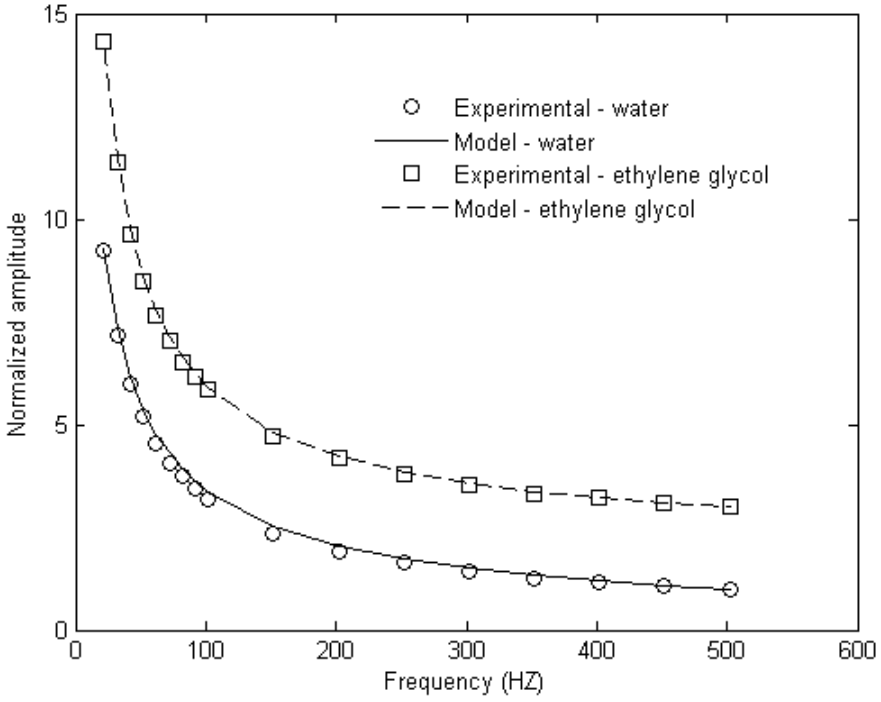

Figure 4.6: Normalized temperature amplitude – water and ethylene glycol (Experimental apparatus validation)

4.2 TEST RESULTS

The recorded temperature signal is the AC component with an operating frequency varying from 22 to 502 Hz. The maximum amplitude of the temperature oscillation is about 0.2 °C at the lower end of the frequency range. According to the steady-state heat conduction analysis of our two-layer structure, the absolute temperature on the stainless steel surface, or the DC component, is about 28 °C and 33 °C with water and ethylene glycol as the test liquid, respectively. This assumes an ambient temperature of 21 °C.

4.2.1 Validation of Experimental Apparatus

The experimental apparatus requires a validation using liquids with well-documented thermal properties. Water and ethylene glycol were chosen for the calibration of our apparatus.

The magnitudes of the AC temperature signal for water and ethylene glycol are shown in Figure 4.6, both the modeling result and the measurement data are given. For the modeling result, the amplitudes at different frequencies are normalized by the absolute value of the signal magnitude at the highest frequency, which is at the lowest level. The same principle is applied to the experimental data. In order to display clearly, the data of ethylene glycol in this figure is shifted up by two units. For both cases of

water and ethylene glycol, the normalized amplitude measurements match the model prediction very well as shown in Figure 4.6.

Figure 4.7 shows the phase shift data of the temperature signal. For both water and ethylene glycol, the experimental data fits the model well except in the low frequency range, especially below 50 Hz. At low frequency, the large penetration depth causes the phase shift measurement to diverge from the model because the semi-finite domain assumption of the liquid layer becomes problematic. For example, an operating frequency of 50 Hz will lead to a thermal wave penetration depth of about 0.3 mm in the case of water.

In the model developed for this study, shifting the magnitude of the thermal conductivity a small amount from the nominal value, the sensitivity of the amplitude and phase shift to the value of thermal conductivity can be assessed. This simple analysis shows that the phase shift is much more sensitive to the variance of thermal conductivity than the amplitude. Therefore, the phase shift data is employed below for linear regression analysis. More details are discussed in the error analysis section.

The procedure of finding the nominal value and the confidence interval of the measured thermal conductivity is as follow. First, the frequency range from 52 to 502 Hz is chosen by observation to avoid potential two-dimensional effects at low frequencies and low signal strengths at high frequencies. Second, the standard least square method is employed to find the nominal value of thermal conductivity by matching the experimental data to the model in Eq. (3.24). Third, the standard error of the fit is calculated with the experimental data and the model using the nominal value found in the

last step and, then, the 95% confidential interval of phase shift is obtained. Finally, the 95% confidence interval for the thermal conductivity was derived from the phase shift using the least square method again.

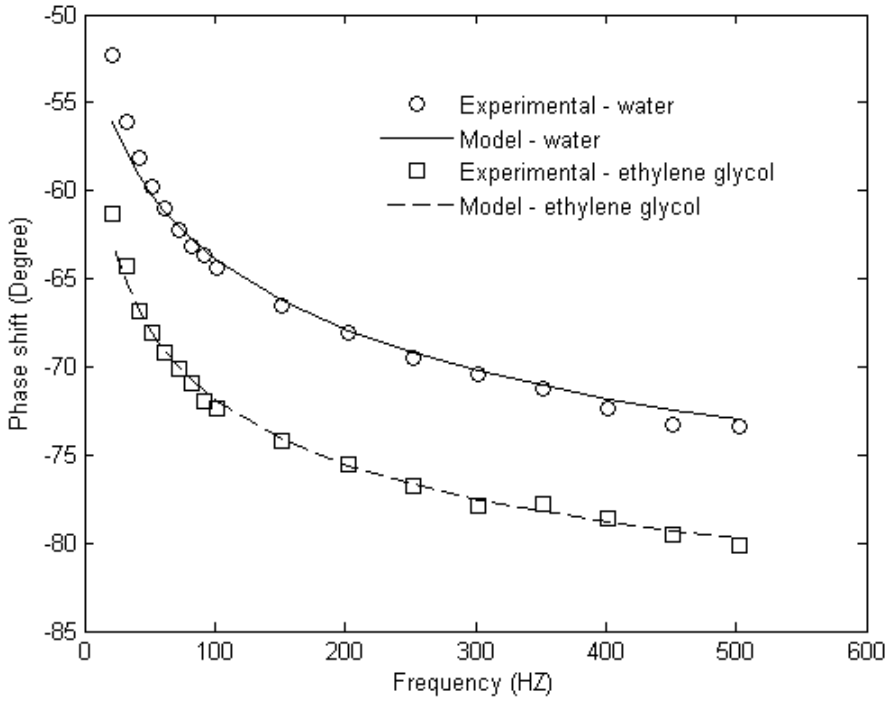

Figure 4.7: Phase shift – water and ethylene glycol (Experimental apparatus validation)

The nominal values of thermal conductivity for water and ethylene glycol measured here are 0.614 W/m·K and 0.253 W/m·K, respectively. The 95% confidential interval is below ±5% uncertainty for both cases. The thermal conductivity of water and ethylene glycol in the literatures [74] are 0.613 W/m·K and 0.252 W/m·K at 30 °C.

Another way to ascertain our measurement technique is to compare the temperature signal waveform recorded from the oscilloscope to that from the simulation model. Recall that the heating signal is a square wave and can be decomposed into a

series of sinusoidal functions of specific frequencies according to Fourier expansion. Because of the linearity of our heat transfer system, each sinusoidal component in the heating signal will generate a temperature oscillation sinusoidal signal with the same frequency. The total temperature response will be the sum of those temperature signal sinusoidal functions.

Figure 4.8 shows the temperature signal waveforms at 22, 52, 102, and 502 Hz from the experiment and the simulation for the water case. The experimental part is recorded using the oscilloscope and Labview, and the modeled curve is synthesized using the above method. Due to the high noise level in the experiment, the average mode of the data acquisition setting in the oscilloscope is chosen and the time constant is adjusted to the highest level during the data logging. The temperature scale is normalized by the maximum temperature difference for both the cases. Those two waveforms share almost the same shape.

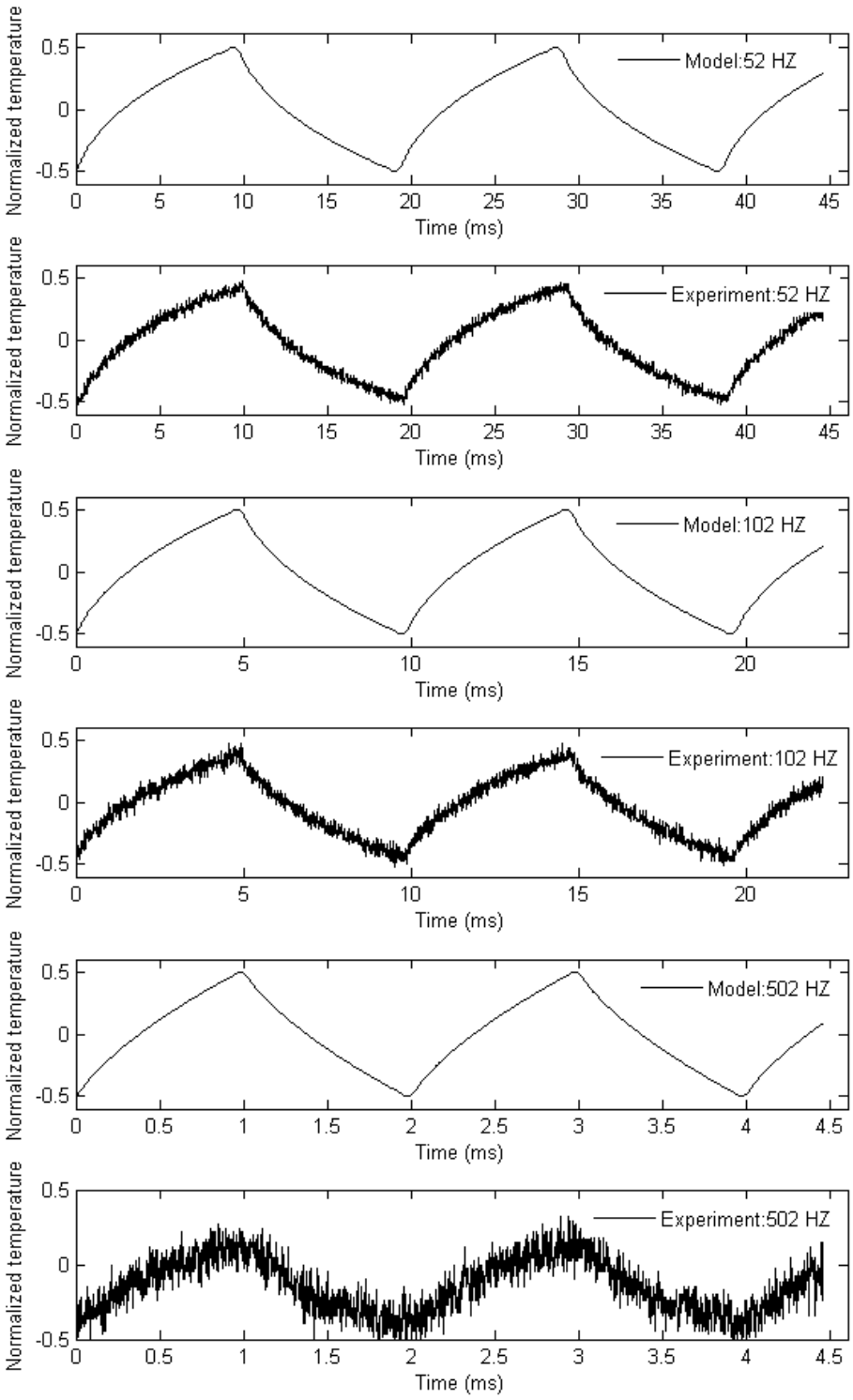

Figure 4.8: Waveforms of the temperature signal (Experimental apparatus validation)

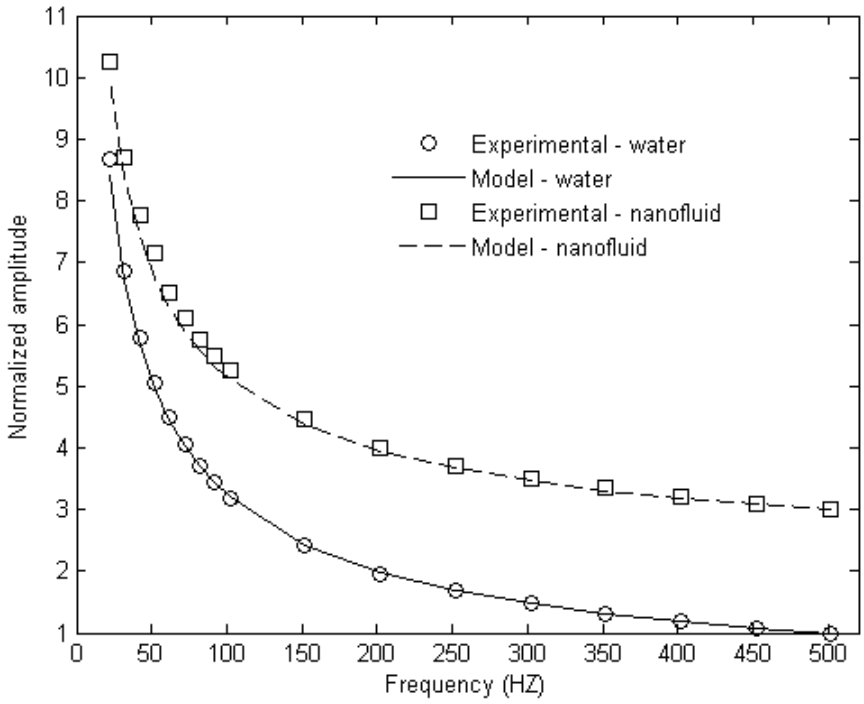

Figure 4.9: Normalized amplitude: water and nanofluid (Nanofluid thermal conductivity measurement)

4.2.2 Nanofluid

The test nanofluid consisted of an aqueous solution of gold nanoparticles dispersed throughout the liquid. The liquid/particle mixture was generated via the citrate chemical synthesis process [75]. The nominal concentration of gold is 0.058 g/L and the average particle size is 4.5 nm with a standard deviation of 1.5 nm. Before the thermal conductivity measurement, the test liquid sample was ultrasonicated for over two hours and a stable and uniform liquid was observed by visual inspection before the test. Since

our work focuses on the development of the measurement technique at this current stage, characterization and preparation of nanofluid will not be covered in this work.

Before conducting measurements on the nanofluid, deionized water was tested as before to calibrate the experimental apparatus and provide a reference standard for the nanofluid. After the measurement with water, the test chamber was purged with dry nitrogen and then recharged with nanofluid through the two supply lines. All the other experimental settings were kept the same during this process in order to avoid other unaccounted for errors introduced into the measurement results.

An implicit assumption so far is that the density and heat capacity of our test liquid are fixed. By observing the temperature expression for the front surface of the heating strip, or Eq. (3.24), we have determined that the thermal conductivity and heat capacity of the test liquid cannot be measured separately by our current apparatus. Because of the small volume fraction of nanoparticles, the density and heat capacity of the nanolfuid are assumed to be the same as that of the base fluid. Murshed et al. [n5] conducted the measurement of effective thermal diffusivity and thermal conductivity of nanofluids simultaneously using transient hot-wire technique and suggested that the effective heat capacity of nanofluids show little variance from the base fluid under small volume fraction. Therefore, thermal conductivity of the nanofluid is the only unknown in our model and can be predicted using the least squares curve fitting method from the experimental data. The procedure described in the last section is employed to obtain the nominal value of the nanofluid thermal conductivity. The only difference is that the frequency range chosen for the curving fitting is from 152 to 502 Hz. The reason will be

discussed in the following discussion section. The nominal value of the nanofluid thermal conductivity is found to be 0.799 W/m·K and the enhancement of the thermal conductivity of nanofluid is predicted to be 30.4% compared with water. Once the enhanced thermal conductivity is obtained, the amplitude and phase shift curves can be generated, as shown in Figure 4.9 and 4.10.

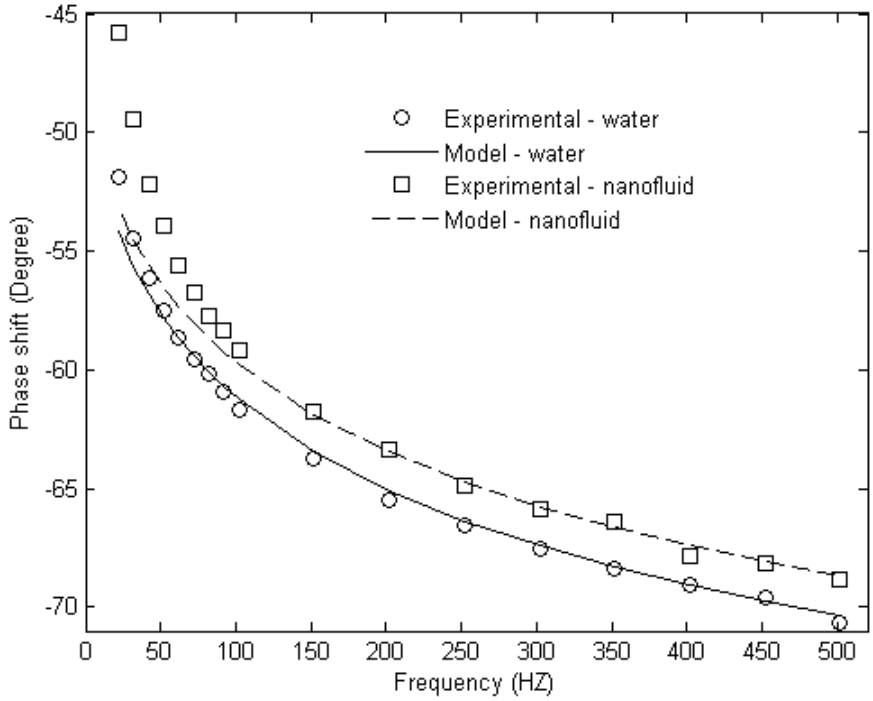

Figure 4.10: Phase shift – water and nanofluid (Nanofluid thermal conductivity measurement)

Figure 4.9 shows the normalized amplitude of the temperature signal for water and the nanofluid. Again, all the data points for the nanofluid here are shifted up two units for clear display. Both measurements fit the model well. As discussed above, this

amplitude information will not be used for the estimation of the thermal conductivity enhancement because it is not sensitive to the thermal conductivity of the liquid.

The phase shift data is presented in Figure 4.10. Again, the experimental data for pure water fits the theoretical prediction quite well although some small derivation appears in the low frequency zone. For the nanofluid, a good match is found in the high frequency zone, above 152 Hz in our case. However, for the low frequency regime from 22 Hz to 152 Hz, the derivation between the experimental data and the theoretical model grows when the operating frequency decreases. Although some error was expected due to the large penetration depth at low operating frequency, the magnitude of this discrepancy is higher than expected.

4.2.3 Discussion

Our strategy of understanding our experimental data is to apply the concept of the effective thermal conductivity to nanofluids modeling first, and then identify the divergence between the theoretical model and the experimental data. Combining with other information, this discrepancy may provide some insight of the heat transfer mechanism of nanofluids.

As shown in Figure 4.10, the curve fits the model of effective thermal conductivity quite well at the high frequency, above 152 Hz. By applying the same curve fitting method to the low frequency zone, we have a higher effective thermal conductivity compared with that given by the high frequency data. This suggests that the

heat transport process in nanofluid tends to be more effective under the low operating frequency than under the high operating frequency in our apparatus.

From the temperature expression in the Principle of Measurements section, or Eq. (3.24), the temperature and its gradient can be derived. As shown before, the temperature amplitude is very low with a maximum value of about 0.2 °C. However, the temperature gradient shows a strong variance in the operating frequency range, from about 6000 K/m to 3000 K/m in our case. For the transient hot-wire method, the governing formula of the temperature expression in the literature [33] indicates that the temperature gradient is almost constant during the measurement time.

Wen et al. [22] reported a high heat transfer enhancement at the entrance region of a laminar flow configuration with oxide particle nanofluids. Lee et al. [23] conducted a experimental study of convection heat transfer of nanofluid laminar flow in micro-channels. Heat transfer enhancement was observed due to higher thermal conductivity of nanofluids. Similar to the results of Wen et al., a higher heat transfer coefficient was found at the entrance region of the micro-channels. The highest temperature gradient normally occurs at the entrance region of pipe flow and for a constant heating flux configuration. In contrast, the temperature gradient in thermally fully-developed flow stays constant.

Based on the above experimental studies of convection heat transfer of nanofluids, and our phase sensitive measurement results, we find evidence that the temperature gradient could play a role in the heat transport process of nanofluids. For the transient hot-wire method, the governing formula of the temperature expression in the

literature [33] indicates that the temperature gradient is almost constant during the measurement time. Most reported measurements on nanofluids thermal conductivity using the transient hot-wire method are only effective thermal conductivity values. Information on the heating flux, the size of the hot wire, and other experimental setting is not described in detail. Therefore, a determination of the temperature gradient in these experiments cannot be made. We suggest that the effect of the temperature gradient should be taken into account in future experimental studies, especially for the problem of resolving the experimental inconsistencies. The above experimental study of convection heat transfer of nanofluid flow and our phase sensitive measurement both imply that the role of temperature gradients in the heat transport process of nanofluids should be carefully studied.

4.3 UNCERTAINTY ANALYSIS

The measurement procedure and the parameters involved provide a guideline of the error analysis. Eq. (4.1) gives the relative parameters in the phase shift measurement and Eq. (4.2) implies that the thermal conductivity of the liquid is found from the measured phase shift using the curve fitting method.

Eq. (4.1) states that the final phase shift used to calculate the thermal conductivity of the test liquid is a function of several parameters: the measured phase of the voltage signal from the pre-amplifier, the phase shift of the power switch, the phase shift of the pre-amplifier, thermal properties of the stainless steel, thermal properties of the liquid,

the thickness of the stainless steel, and the operating frequency. A scaling analysis of each of the above parameters will be performed to identify the main error sources first. Then, the model will be employed to find out how the error propagates from the phase shift data to the resulting value of thermal conductivity.

$$\psi = \psi\left[\psi_m, \psi_{ps}, \psi_{amp}, k_s, \rho_s, \left(c_p\right)_s, \rho_l, \left(c_p\right)_l, L, f\right] \tag{4.3}$$

$$k_l = k_l\left(\psi\right) \tag{4.4}$$

First, simple simulation shows that the thermal properties of the stainless steel are not sensitive to the phase shift of the temperature signal and can be ignored in the error analysis.

The power switch introduces an extra phase shift into the signal transferring path and needs to be quantified. With the heating signal as the input and the TTL trigger signal as reference, this phase shift can be measured. The standard deviation of this measurement result is very low and no uncertainty from this measurement will be considered.

The pre-amplifier brings phase shift into the measurement process. The phase shift can be calculated from the electrical diagram from the manufacturer. The calculation shows that very small error will enter into the final result and can be neglected also.

The 4 1/2 digit resolution of the TTL signal generated by the lock-in amplifier implies the error from the trigger frequency *f* is insignificant and does not need to be considered in the error analysis.

Since the thermal conductivity of the liquid is the desired property, the density and heat capacity are assumed to be constant at this development stage of the technique and no error from these liquid property values will be considered further.

Therefore, the above equations will be reduced to

$$\psi = \psi\left(\psi_m, L\right) \tag{4.5}$$

$$k_l = k_l\left(\psi\right) = k_l\left(\psi_m, L\right) \tag{4.6}$$

The tolerance of the stainless steel strip provided by the manufacturer is 2% and will be treated as systematic error. The error of the measured phase shift is the random uncertainty that will propagate into the final result. The 0.01 degree phase resolution suggests that the systematic error of the lock-in amplifier can be ignored compared with that of the random error. Using the root-sum-squares (RSS) method, the uncertainty in the mean value of the thermal conductivity, u_k, is estimated from:

$$u_k = \left[\left(\frac{\partial k}{\partial L}\Delta L\right)^2 + \left(t_{v,95}\frac{\partial k}{\partial \psi}\Delta\psi\right)^2\right]^{1/2} \tag{4.7}$$

By assigning different thickness, L, to the model, the sensitivity index of the thickness, $\partial k/\partial L$, can be determined. Using the same method, we can find the sensitivity index of the phase shift, $\partial k/\partial \psi$.

The uncertainty from the measurement of random error is fitted to be 0.0296 W/m·k, and that from the thickness tolerance of the stainless steel strip is 0.0288 W/m·k.

Therefore, the total uncertainty of the thermal conductivity measurement is 0.0413 W/m·k, or approximately 5% of the nominal value.

5. WALL SHEAR STRESS MEASUREMENTS

This chapter comprises two sections. Section one is about development and simulation of a wall shear stress sensor design. A wall shear stress sensor design with a heater and two temperature sensors on a silicon dioxide substrate is analyzed. The heater with a periodic source generates a temperature oscillation field which interacts with the flow field. The temperature sensors pick up the temperature response that contains the information of the velocity gradient at the wall. Based on the above sensor design, a two-dimensional conjugate heat transfer model is developed and solved numerically with a finite difference method. Two designs, with and without a heat sink under the silicon dioxide substrate, are studied. The effects of the two main design parameters, the operating frequency and the distance between the heater and the temperature sensor, are discussed. Section two is an experimental validation of the concept utilizing the thermal wave approach for wall shear stress measurements. A thin stainless steel strip adjacent to a flow field of water is heated by a periodic current. Different mass flow rates in the channel lead to different velocity gradients on the surface of the stainless steel strip. The temperature signal at the other surface of the stainless steel strip is monitored by an infrared detector. The experimental results show a dependence of the phase shift of the temperature signal on the mass flow rate. Due to the thin penetration depth of the thermal wave in our case, the results suggest that the phase information could be used for the measurement of the wall shear stress.

5.1. SENSOR DESIGNS AND SIMULATION

5.1.1 Assumption Discussion

Before the principle of our wall shear stress measurement design is introduced in the following sub-section, a fundamental assumption in many measurement techniques needs to be examined, which concerns the velocity profile adjacent to the measurement surface. For those indirect methods, such as the MEMS thermal sensor [44] and the optical shear stress sensor [57], determination of wall shear stress relies on the measurement of the velocity gradient at the wall. In order to correlate the measured velocity gradient directly to the wall shear stress, a linear velocity profile is normally assumed in the region where measurement is conducted.

For turbulent boundary layers with a finite shear stress, a linear velocity profile can be found in the so-called viscous sublayer according to the classical boundary layer theory [71], and therefore, the thickness of this constant velocity gradient zone can be determined. According to the universal law of the wall [71], for the wall shear stress ranging from 0.1 to 10 Pa, the thickness of the corresponding viscous sublayer will vary from 240 to 30 micrometers in air flow. This thickness is of great importance in the measurement techniques mentioned above and places an upper limit on the measureable wall shear stress due to the fact that flows with higher Reynolds number lead to higher wall shear stress and thinner viscous sublayers.

The optical shear stress sensor measures the flow velocity at a point away from the measurement surface [57]. If this point is located inside the viscous sublayer, the velocity gradient, or the wall shear stress, can be derived from the known linear relationship between the location of the measurement point and the measured flow velocity. Although some efforts tend to extend this technique to the logarithmic overlap layer by taking velocity measurements at more than one point [76], there exist other constraints for extensive applications of this technique, such as low seed density in the viscous sublayer. For the surface mounted thermal shear stress sensor, a similar situation occurs regarding the linear velocity regime. The temperature gradient normal to the flow direction shall decay to a negligible level at the edge of the viscous sublayer in order to avoid the effect of the outer sublayer and the turbulence in the main stream.

5.1.2 Sensor Design

This section introduces the basic design of our wall shear stress sensor and shows how the components function together to extract the information of the wall shear stress from the flow field. Figure 5.1 shows the schematic of the measurement system. Region one is the solid substrate and region two is the air flow field with a linear velocity profile, as shown in Figure 5.1 (a). The sensor system is embedded in the substrate at a downstream location. Figure 5.1 (b) shows the design of the sensor system in detail. A heater is located right below the solid/fluid interface and the distance between the heater and the interface is *d*. This distance is fixed to be 1 μm in this study

for simplicity. There are two temperature sensors mounted on the surface of the substrate, one upstream and another downstream relative to the heater. The distances between the heater and the two sensors are identical. The temperature signals from these two temperature sensors will be used to determine the velocity gradient in the flow field by measuring the phase difference between these two temperature sensors using a lock-in amplifier. There are several reasons for using two temperature sensors instead of one. First, the sensitivity of the temperature signal to the velocity gradient can be improved by using this configuration, especially for the phase information. The phase difference between the two temperature sensors can be strongly dependent on the velocity gradient. Second, the change of the flow direction can be easily detected with this design. Last, the effect of thermal perturbation on the velocity gradient measurement may be offset and minimized with this two-sensor design.

The measured temperature signal can be expressed as Eq. (5.1), in which T_{mag} is the magnitude of the temperature oscillation and ψ is the phase information. Further, Eq. (5.2) shows the design parameters of our shear stress sensor. The parameters that determine the temperature magnitude include the heating flux, q_0, the distance between the heater and the sensor, l, the velocity gradient, c, and the operating frequency, ω. The phase shift of the measured temperature signal will be a function of all the above parameters except for the heating flux.

$$T = T_{mag}\, cos(\omega t + \psi) \tag{5.1}$$

$$T_{mag} = T_{mag}(q_0, l, c, \omega) \qquad \text{and} \qquad \psi = \psi(l, c, \omega) \tag{5.2}$$

In order to secure a reasonable design at this preliminary development stage, the following procedure of determining the design parameters is employed. First, under a certain range of velocity gradient that holds engineering interest, the values of the operating frequency and the distance between the heater and the sensor are determined to ensure good sensitivity of the phase shift to the velocity gradient. Second, once the operating frequency and the distance between the heater and the sensor are determined, the heating flux can be adjusted to raise the temperature magnitude to a level that is detectable by commonly used temperature sensor, such as thermocouples and resistance temperature detectors (RTD). With the above parameters, the maximum temperature difference can be obtained through the steady-state solution and the effect of the radiation, natural convection, and the change of air thermal properties can be evaluated.

Figure 5.2 shows the signal processing diagram of the measurement system, which can be easily implemented with current instrumentation technology. Similar experimental setups can be found in previous studies on characterization of thin film thermal properties [1~3]. A TTL trigger signal from a lock-in amplifier or a function generator provides a periodic Joule heating source through the heater. The temperature fluctuation caused by the heating source propagates to the two temperature sensors and the temperature signal processor collects these two periodic temperature signals. With

the two temperature signals from the temperature signal processor as the input, the lock-in amplifier can find the phase difference between them.

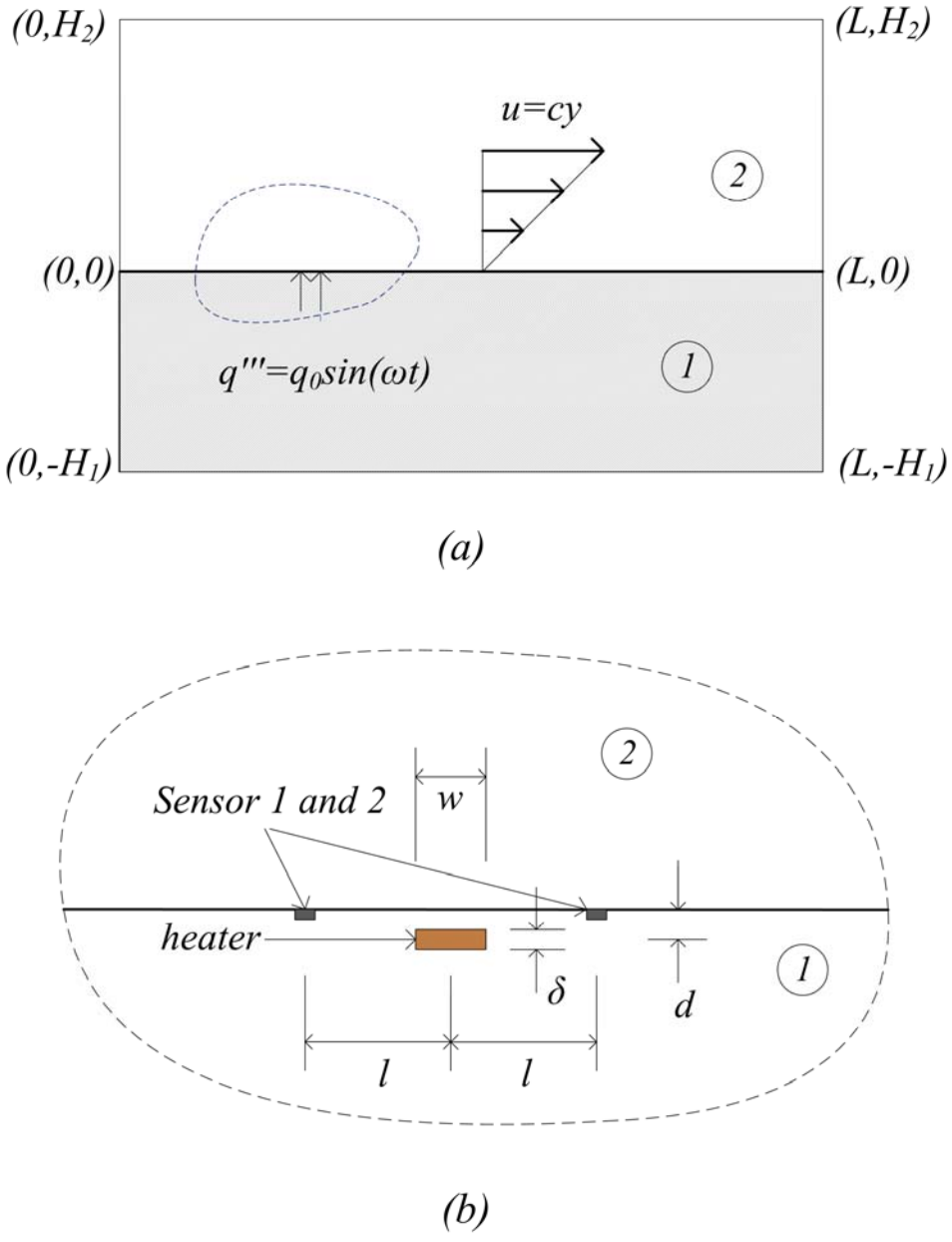

Figure 5.1 Wall shear stress measurement: (a) computation domain; (b) sensor design

As discussed in the Introduction, thermal interaction between the substrate and the heating element could be one of the major sources of error. MEMS based sensors use a vacuum cavity underneath the heating element to improve signal sensitivity [44]. In order to explore the effect of the substrate on our thermal wave based design, the simulation of the sensor design with a vacuum cavity underneath the heating element is also conducted using the numerical model developed below. The results show that the sensitivity of the frequency-dependent temperature signal to the velocity gradient is not much different from that of the design without a vacuum cavity. Meanwhile, the drawbacks related to the vacuum cavity, such as high temperature on the heating surface, remain. Therefore, the sensor designs discussed below will not cover this type of design.

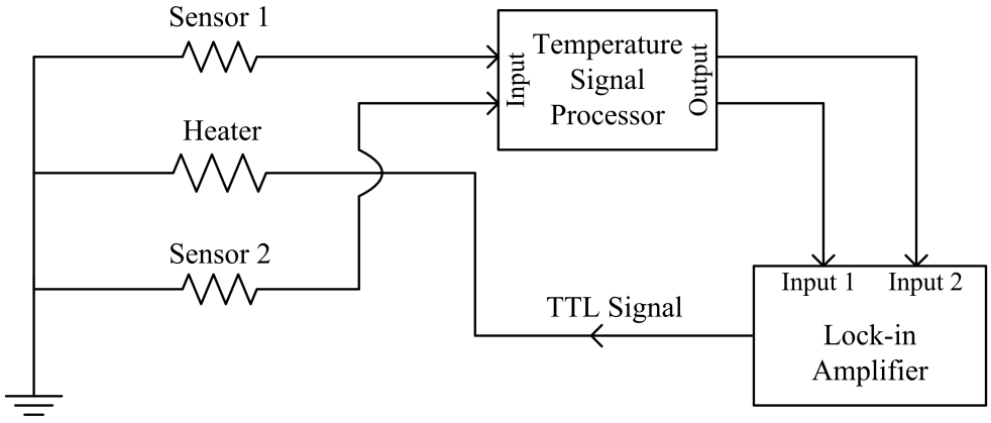

Figure 5.2 Wall shear stress measurement: Signal processing diagram

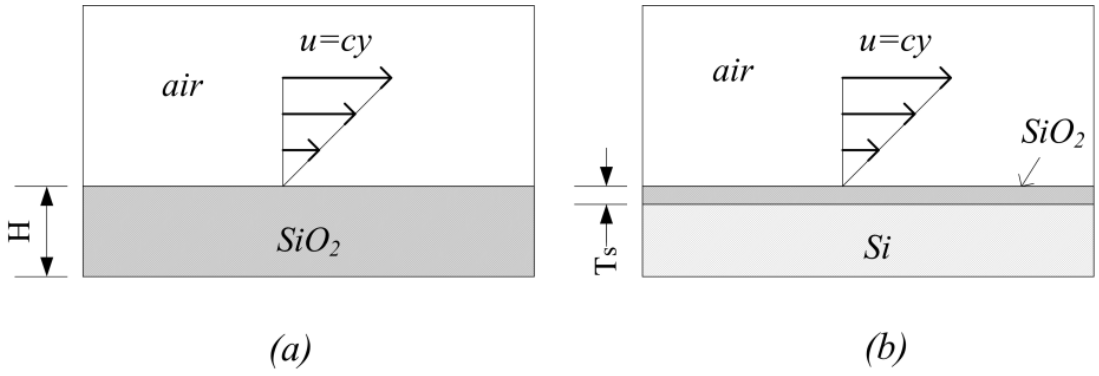

Figure 5.3 Wall shear stress sensor designs: (a) No heat sink; (b) With heat sink

Based on the above discussion, two designs with different substrate configurations will be studied in the following sections, as shown in Figure 5.3. Figure 5.3 (a) shows a sensor design with silicon dioxide only as the substrate. In Figure 5.3 (b), the substrate is a two-layered structure. A silicon dioxide layer is on top of the silicon substrate which functions as a heat sink. The locations of the heater and the sensors in the silicon dioxide layer are the same for both substrate configurations. The reason to add this heat sink feature into our study is two-fold. First is to lower the absolute operating temperature of the sensor to avoid the change in air thermal properties during the measurement. Second, the heat sink may provide some solution to minimize the thermal perturbation from ambient and the substrate by bypassing a portion of the disturbing heating flux. Also, the simulation results show that the thickness of the silicon dioxide layer has little effect on the sensitivity of the phase shift to the velocity gradient. At the current research stage, the thickness of the silicon dioxide layer is set to 20 μm in the development below.

5.1.3 Numerical Simulation Procedure

In this work, the standard finite difference method is employed to solve a conjugate heat transfer problem with a periodic heating source on the solid surface. Based on the discussion in the Principle of Measurements section, the AC part of the complete solution will be considered in this section. Furthermore, the solution at the fundamental frequency only will be found to explore the relationship between the temperature signal and the velocity gradient of the flow field.

As shown in Figure 5.1, this computational domain is divided into two regions. Region one is the solid and region two is the liquid with a linear velocity profile. The length L of the domain is 1.8 mm. The height of the solid domain is 0.12 mm and the height of the fluid domain is 0.24 mm. In order to illustrate the relationship between the temperature signal and the velocity gradient, we assume the following:

1. The working fluid is air and has constant thermal properties;
2. The solid substrate is silicon dioxide;
3. The heating source is on the solid-fluid interface, assumed to be 10^6 W/m^3;
4. The operating frequency of the heating source is either 400 or 800 HZ;
5. The velocity gradient is assumed to be 2×10^4, 6×10^4, 10×10^4, and 14×10^4 per second.

As discussed in Chapter Three, the method of complex combination can be employed to solve this particular problem and the governing equation for region one can be expressed as:

$$\alpha_1\left(\frac{\partial^2 T}{\partial x^2}+\frac{\partial^2 T}{\partial y^2}\right)=i\omega T \tag{5.3}$$

For region two:

$$\alpha_2\left(\frac{\partial^2 T}{\partial x^2}+\frac{\partial^2 T}{\partial y^2}\right)=i\omega T+cy\frac{\partial T}{\partial x} \tag{5.4}$$

The dimensions of the computational domain, L and H, are placed distant enough from the heating source so that the temperature signal near the boundaries decays to zero. The temperatures at the boundaries of the computation are all set to zero except that there is a heating source at the interface of the solid and fluid domains.

$$T\Big|_{x=L,y}=T\Big|_{x=0,y}=T\Big|_{x,y=0}=T\Big|_{x,y=H}=0 \tag{5.5}$$

The heating source applied can be expressed as:

$$q = -k\frac{\partial T}{\partial y}\Big|_{x=L_1\sim L_2,\,y=0} = q_0 \sin(\omega t) \tag{5.6}$$

A standard finite difference scheme is employed to discretize the computational domain, as described in Chapter Three. The nodes at the solid/liquid interface, however, need special treatment. At the interface, the upper half of the computational cell is assigned to be the liquid domain and the lower half is the solid domain. In the discretized energy conservation equation, the thermal properties in the *x* direction are the mean values of those of the two materials and no adjustment is required in the *y* direction. The total nodal numbers in the x and y directions are 200 and 200, respectively.

5.1.4 Simulation Results

This section presents the simulation results for the two sensor designs. The following discussion examines the effects of the operating frequencies and the distance between the heater and the temperature sensors on the wall shear stress measurements. In order to illustrate the possibility of using the thermal wave approach for wall shear stress measurement, the range of the velocity gradient in this study is chosen to be from 2×10^4 to 14×10^4 1/s, corresponding to a wall shear stress from 0.37 to 2.6 Pa in the case of air flow with constant thermal properties.

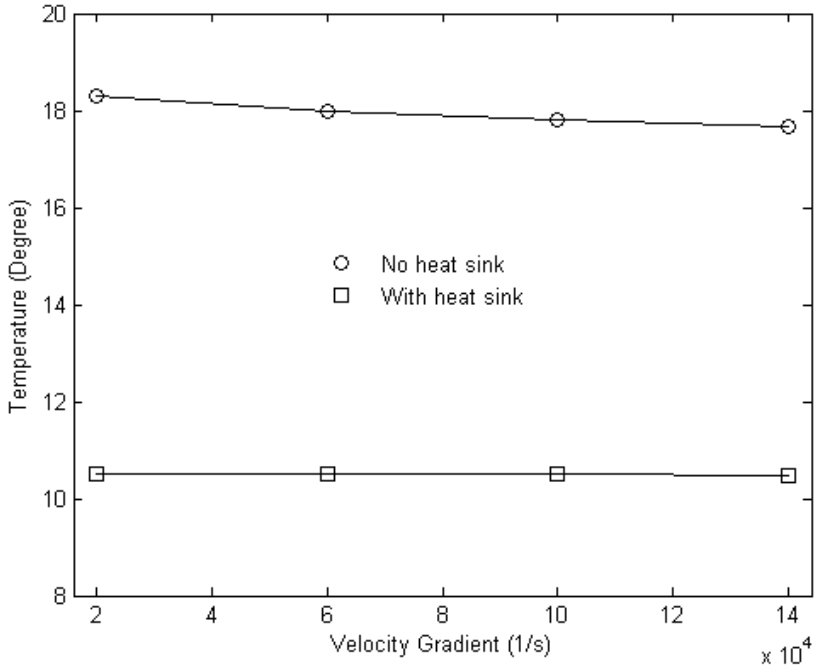

Figure 5.4 Maximum DC temperature difference in the wall shear stress sensor

A. Magnitude of the Temperature Signal

The magnitude of the temperature signal is of great importance in the study of the thermal based shear stress sensor. There are two types of temperature magnitudes in our particular case because the periodic heating source is a positive going square wave and can be decomposed into DC and AC parts. First is the absolute temperature in the DC part of the solution, which corresponds to the steady-state solution of the problem with a constant heating flux and is found in the conventional thermal shear stress measurements [44]. Second is the magnitude of the temperature oscillation observed in the AC part, as shown in Eq. (5.1). Figure 5.4 shows the maximum temperature

difference between ambient and the heater for different designs under various velocity gradients, which is the first type of temperature magnitude. This temperature magnitude does not show a strong dependence on the velocity gradient although the temperature declines slightly with the increase of the velocity gradient for the design without the heat sink. This partially explains why previous thermal shear stress sensor designs require a vacuum cavity under the heating element to improve the measurement sensitivity. However, the heat sink has a significant impact on the temperature magnitude, of which the temperature drops from 18 °C to 10 °C.

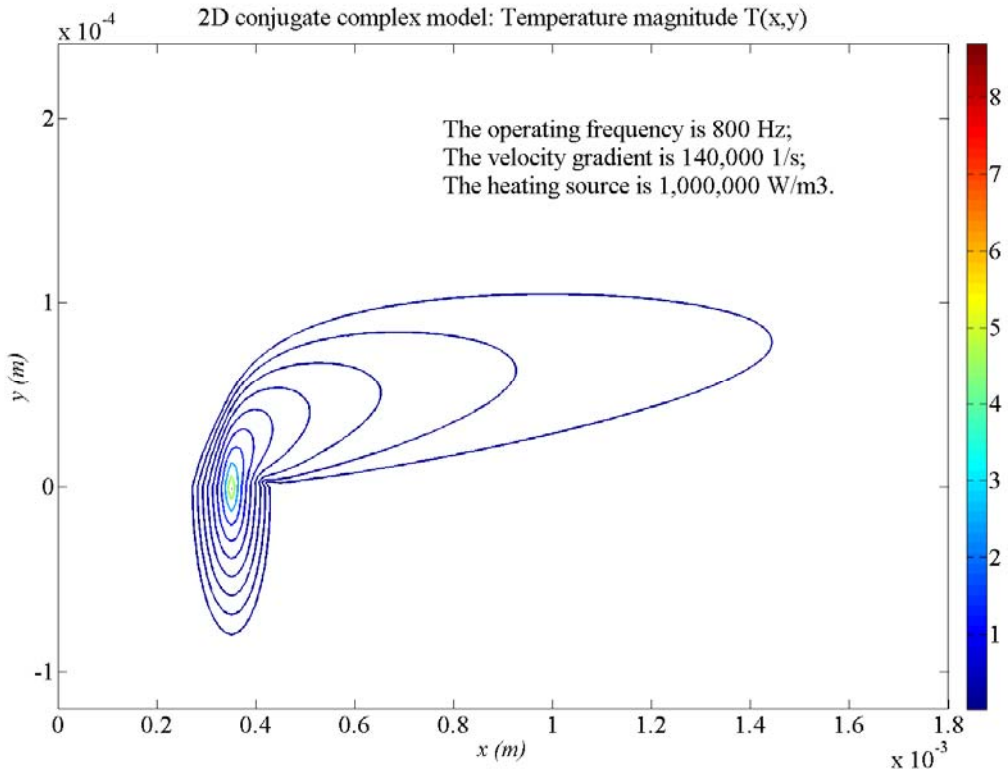

Figure 5.5 Contour plot of the temperature magnitude: design without the heat sink

Figure 5.5 and 5.6 are contour plots for the second temperature magnitude type. The lowest contour level is set to 0.3% of the maximum temperature magnitude in the computation domain, which is that of the heater. No distortion caused at the zero temperature boundary conditions suggest the validity of setting the computation domain size. Figure 5.5 shows the temperature magnitude contour plots of the design without the silicon heat sink. The operating frequency is 800 Hz, the velocity gradient in the air flow is 14×10^4 1/s, and the heating source is 10^6 W/m^3. Figure 5.6 shows the results of the design with the silicon heat sink under the silicon dioxide substrate.

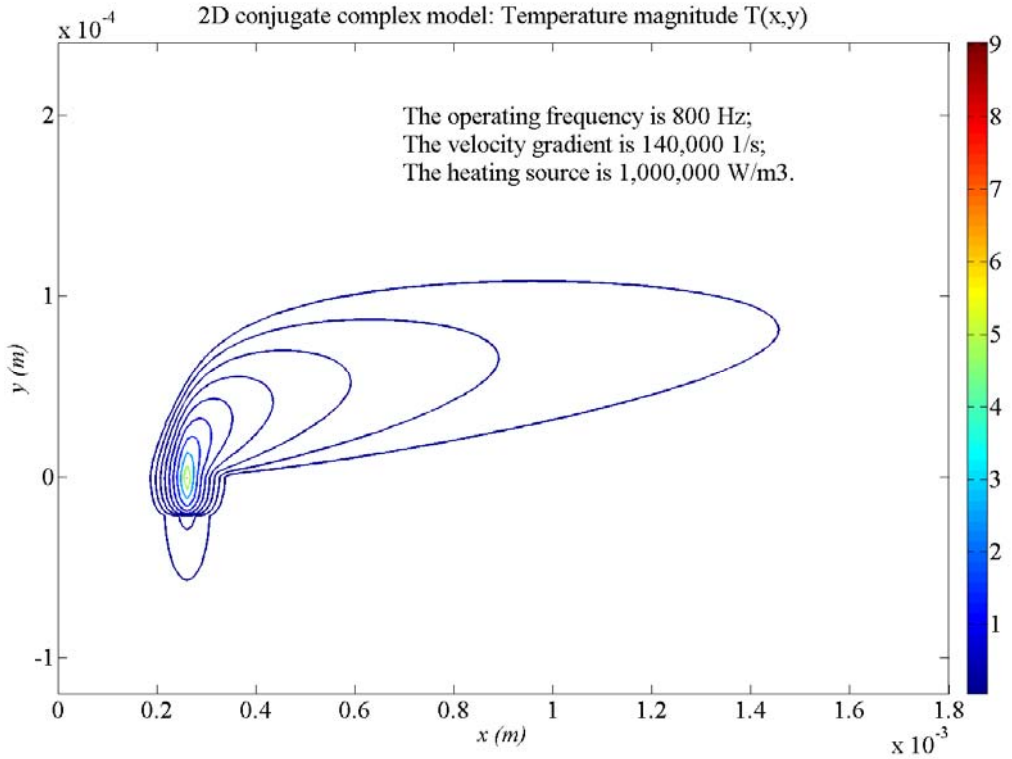

Figure 5.6 Contour plot of the temperature magnitude: design with the heat sink

B. Effect of the Operating Frequencies

This section shows the effect of the operating frequency on the measurement of wall shear stress. Two operating frequencies are studied, which are 400 Hz and 800 Hz, respectively. Both the magnitude and phase information of the temperature signal are presented. The distance between the heater and the sensor is fixed at 45 μm and the heating source is 10^6 W/m^3. This is the design case studied here. Figure 5.7 presents the simulation results of the sensor design without the heat sink and Figure 5.8 is with the heat sink. For both designs, higher frequencies lead to lower temperature magnitudes. For example, the temperature signal magnitude of the sensor design without the heat sink is about 0.54 °C at the operating frequency of 400 Hz. At the 800 Hz operating frequency, the magnitude drops to about 0.22 °C for the same sensor design. The sensitivity of the phase shift to the velocity gradient is higher when the operating frequency is 800 Hz for both designs. Although the design with the heat sink does not share the same sensitivity of the design without the heat sink, the level of sensitivity is still reasonable for practical measurements. For the operating frequency of 800 Hz, the range of the phase shift is about two degree for the design without the heat sink. The design with the heat sink shows a phase shift range of 1.8 ° under the same operating frequency. Another point is that the temperature magnitude does not vary much with increasing velocity gradient and suggests that this approach to measuring shear stress is undesirable.

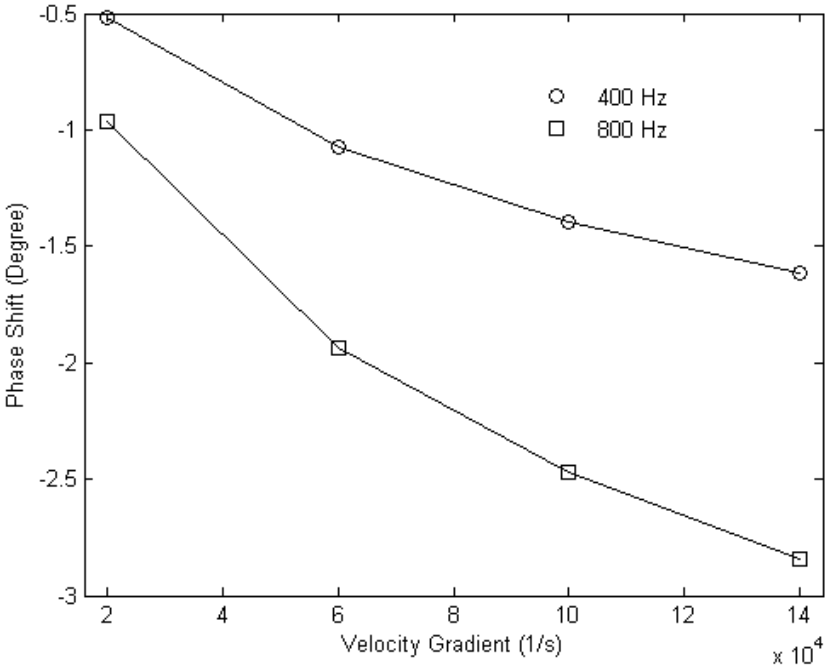

(a)

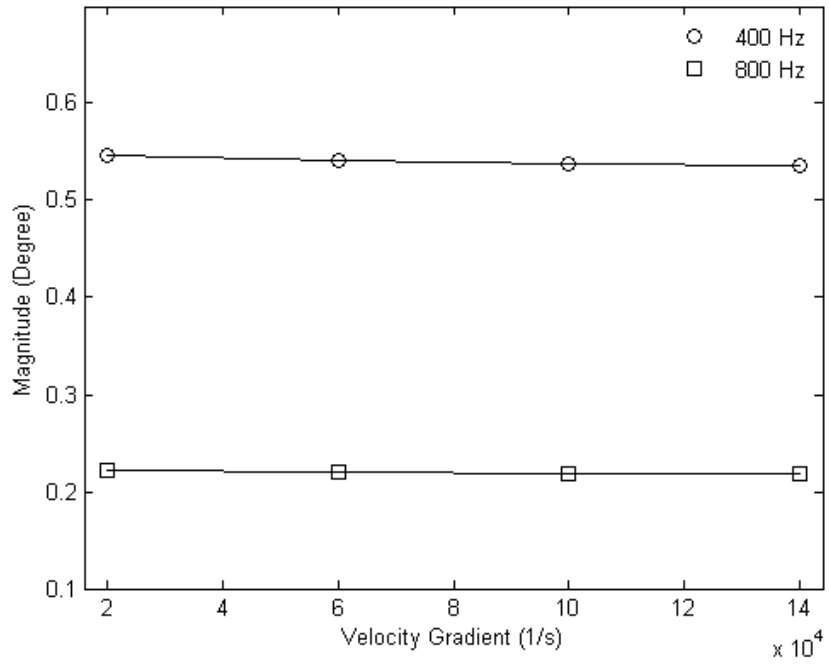

(b)

Figure 5.7 Effect of the operating frequency: Phase shift (a) and magnitude (b) of the temperature signal – wall shear stress sensor design without heat sink

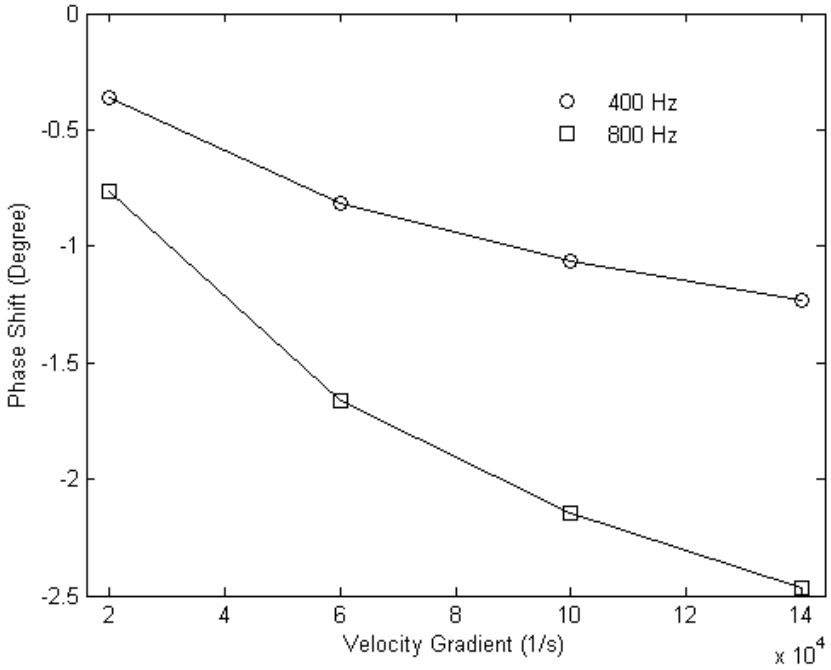

(a)

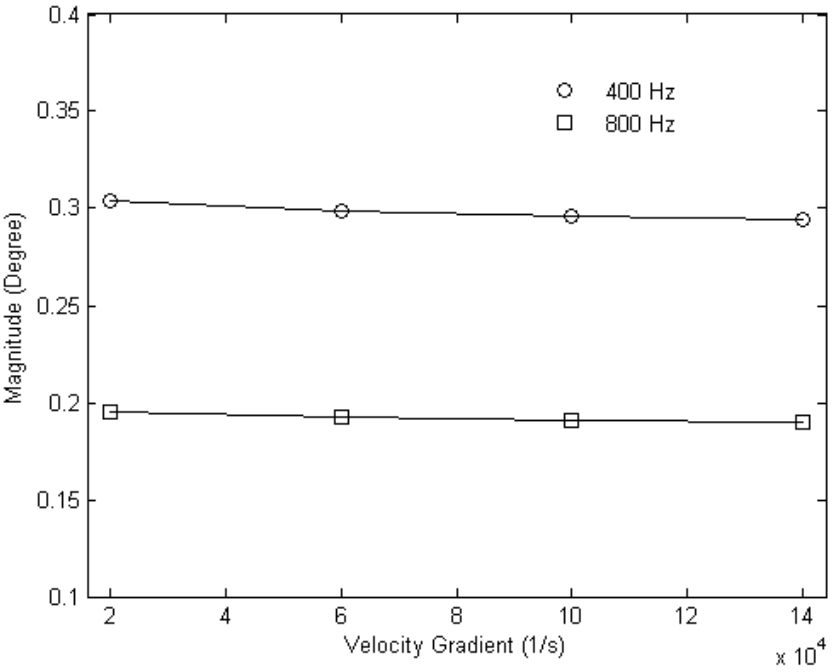

(b)

Figure 5.8 Effect of the operating frequency: Phase shift (a) and magnitude (b) of the temperature signal – wall shear stress sensor design with heat sink

C. Effect of the Distance between the Heater and the Temperature Sensors

Besides the operating frequency, the distance between the heater and the temperature sensor is another important design parameter of our thermal wave based shear stress measurement concept. In this study, two designs with the distance between the heater and the sensor being 45 and 72 μm respectively were investigated. In this study, the operating frequency is 400 Hz and the heating source is 10^6 W/m^3. The simulation is conducted for the designs with and without the heat sink. Figure 5.9 presents the results of the design with the heat sink and Figure 5.10 is without the heat sink. Again, the signal magnitude is not sensitive to the change of the velocity gradient. For both designs, the magnitude of the temperature signal declines rapidly when the sensors move away from the heater. For the sensor design with the heat sink, the temperature signal magnitude declines from 0.3 °C to 0.05 °C when the distance between the heater and the sensor increases from 45 to 72 μm. Also, the design with the heat sink tends to have a lower magnitude compared with that without the heat sink. However, since the heat sink can lower the maximum operating temperature of the sensor, the heating flux can be raised to a higher level to ensure a detectable temperature oscillation without causing a high absolute operating temperature. At the location farther away from the heater, the phase shift of the temperature signal shows a stronger dependence on the velocity gradient for both designs. Again, the sensitivity does not vary much for different designs concerning the heat sink.

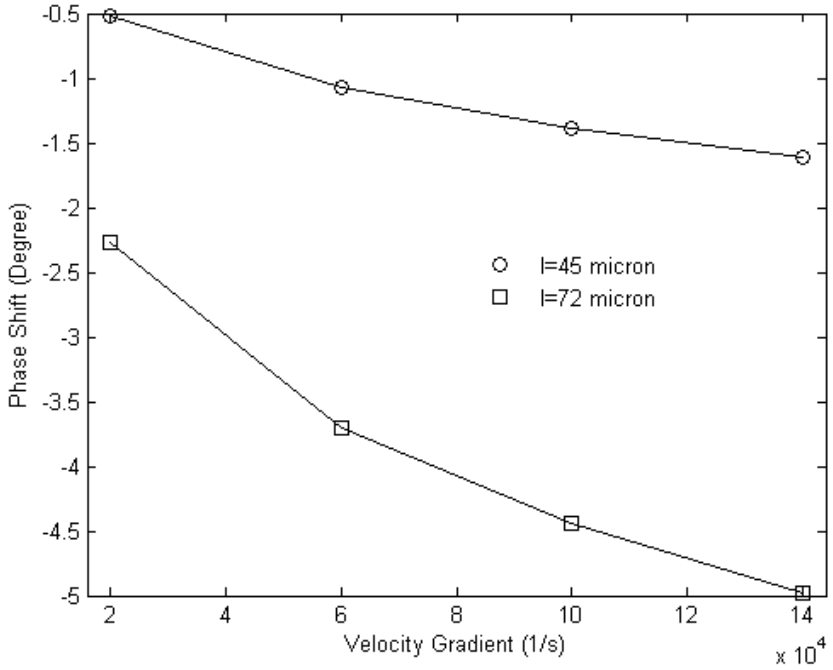

(a)

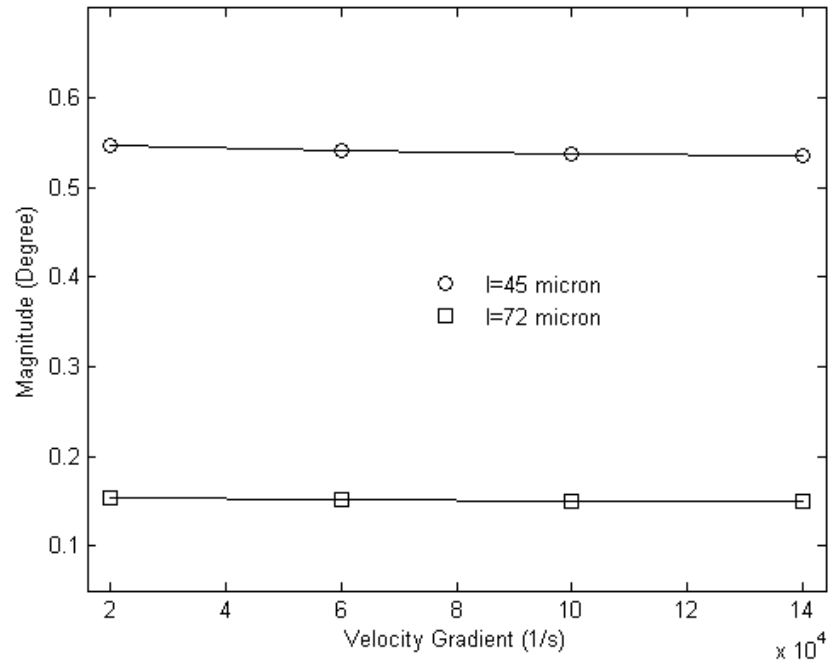

(b)

Figure 5.9 Effect of the distance between the heater and the sensor: Phase shift (a) and magnitude (b) of the temperature signal – wall shear stress sensor design without heat sink

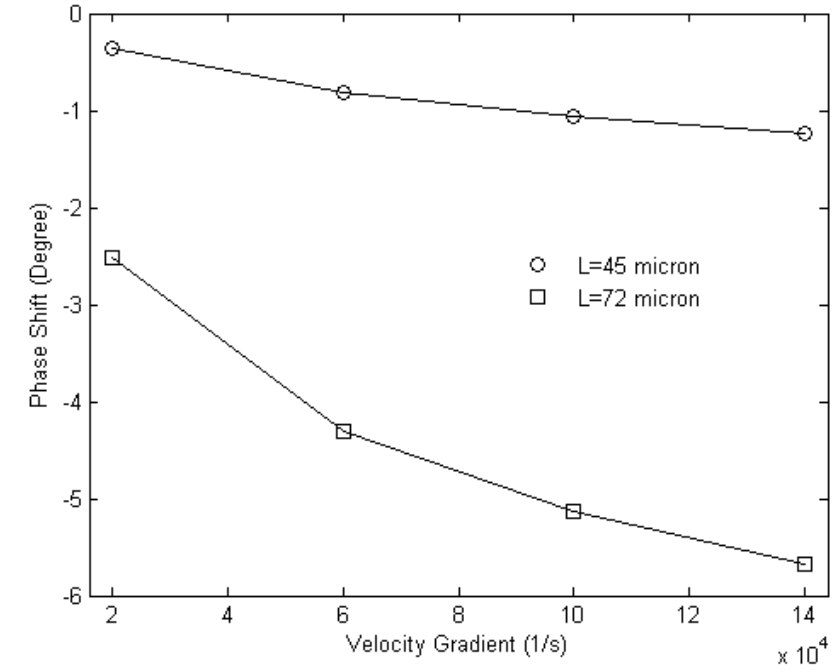

(a)

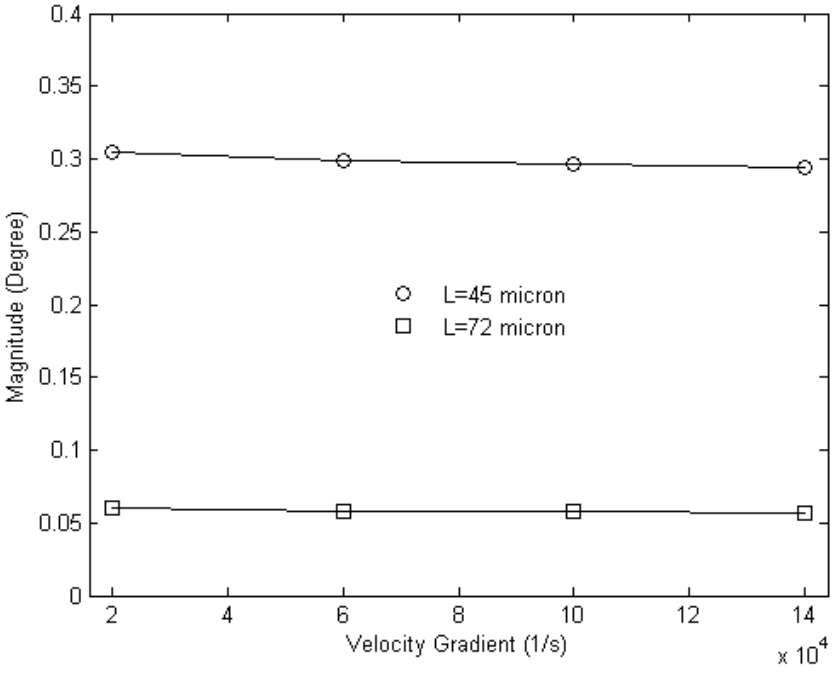

(b)

Figure 5.10 Effect of the distance between the heater and the sensor: Phase shift (a) and magnitude (b) of the temperature signal – wall shear stress sensor design with heat sink

5.1.5 Discussion

The above simulation results suggest that the design with the heat sink shares about the same sensitivity as that without the heat sink. However, Figure 5.4 indicates that the heat sink does lower the maximum temperature difference significantly. Low absolute operating temperature will not lead to a change in air thermal properties and can simplify the sensing and signal processing systems. Since the temperature signal used for our shear stress measurement will not be the magnitude, but the phase information, the heat sink design will help improve the performance of the entire sensor system.

As shown in Figure 5.5 and 5.6, the penetration depth of the thermal wave can be very thin and the magnitude of the temperature signal decays very fast to zero in both solid and flow domains. The linear velocity profile assumption discussed in the Principle of Measurements section tends to be valid because the thickness of the viscous sublayer in the range of interest could be larger than that of the thermal wave penetration depth. This suggests that the velocity fluctuation in the outer layer and the turbulence in the main stream will have no effect on the measurement results based on the thermal wave approach. Meanwhile, one important feature of this sensor design is that the thickness of the penetration depth of the temperature oscillation can be adjusted by varying the operating frequency.

In order to ensure the phase shift of the temperature signal as a practical candidate for the wall shear stress measurement, the magnitude of the periodic temperature signal needs to be detectable for the current temperature sensor technology and the dynamic response of the temperature sensors should be fast enough to provide an accurate temporal signal. The amplitude of the temperature oscillation at the sensor location in this study varies from about 0.1 to 0.6 °C and the range of the operating frequencies can be from 100 to 1000 Hz. The current temperature sensing and electronic signal processing techniques are able to offer a solution for this type of application [77~79]. Another important fact is that the magnitude is related to the energy storage mechanism in the heat transfer system and proportional to the heating source. However, the phase information is independent of the heating source and provides additional flexibility in the sensor design. The magnitude can be lifted to a reasonable level for compatibility with the electronic instrumentation system by adjusting the heating source without any effect on the phase information.

One issue concerning the dynamic response of our wall shear stress sensor design needs to be discussed. The fundamental assumption of our design so far is that there is no other time varying source terms or boundary conditions in this heat transfer system except for the periodic heating source imposed by the heater. However, in real sensor operation, there exist two main sources that will introduce additional time varying terms into the heat transfer system. First is the temperature drift from ambient conditions, such as changes in air temperature in the flow and temperature perturbations from the substrate. Second is a change in the velocity gradient, which will lead to a

different steady-state solution of the system. Therefore, these time varying terms will limit the response time of this type of wall shear stress sensor and the dynamic response of the sensor requires further study. For example, a thermal management study of the heat sink design can help in understanding how fast the temperature shift in the system will decay to a negligible level.

5.2 PRELIMINARY EXPERIMENTAL VALIDATION

In order to validate the concept of using the thermal wave approach for wall shear stress measurement, a simple experiment was designed and conducted with water as the working fluid. The electrical heating, the temperature sensing, and the signal processing systems were the same as that in Chapter Four and will not be included in this section. The only difference is the test cell. In the study of the wall shear stress measurement in this chapter, the test cell with a flow channel was used to provide a water flow field. A thin stainless steel strip adjacent to this flow field was heated by a periodic current. The temperature response on the central point of the stainless steel strip was recorded. The phase difference between this temperature signal and the heating signal was measured by the lock-in amplifier.

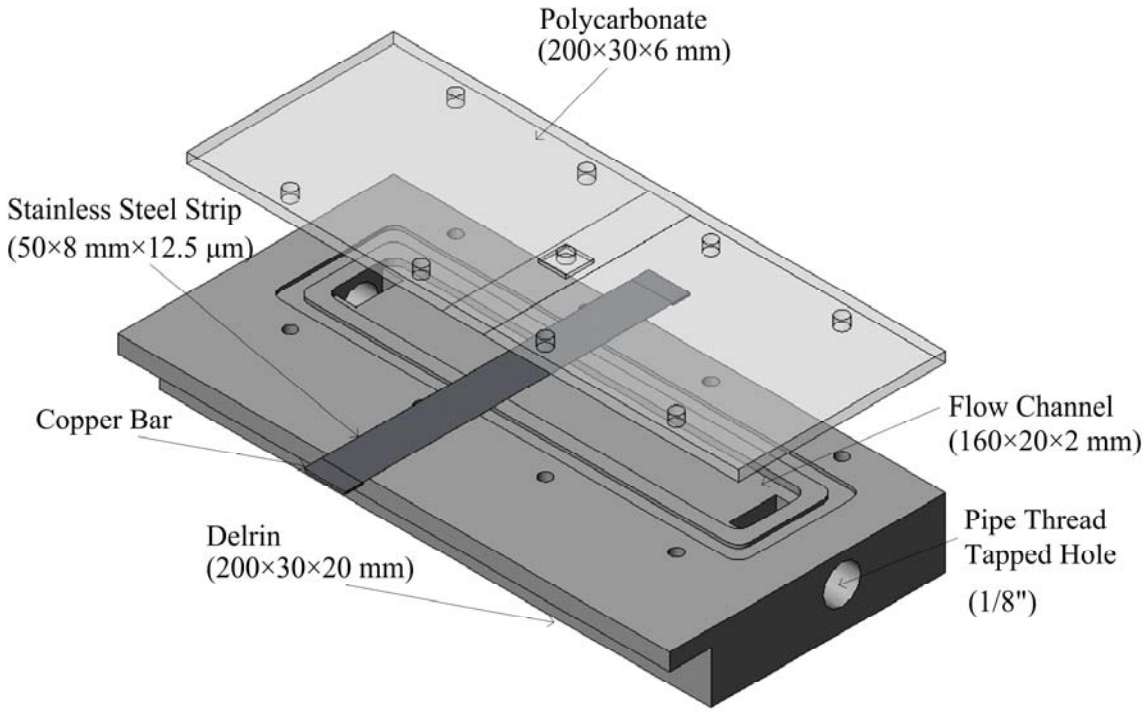

Figure 5.11 Design of the test cell – wall shear stress measurement

5.2.1 Experimental Setting

Fig. 5.11 shows the design of the test cell. An open-mouthed channel with a cross section of 2 mm × 20 mm and a length of 160 mm was machined out of a delrin plate (200×30×20 mm) and two pipe thread tapped hole (1/8") was drilled at the ends of the plate. These holes were connected to the shallow chamber and functioned as the inlet and outlet to the flow field. A polycarbonate plate (200×30×6 mm) was used to seal the front surface of the chamber. Epoxy was employed to seal the gap between the delrin and the polycarbonate plates. A thin stainless steel strip (40×8 mm×12.5 μm) was placed between the polycarbonate and delrin plates and at the central location of the channel.

At the center of the channel, a square hole was milled out of the polycarbonate plate in order to ensure the infrared temperature signal at the center point of the stainless steel strip could be detected, as shown in Figure 5.1.

The sizes of the flow channel were determined carefully and deserve further discussion. First, in order to avoid the edge effect of the flow channel, a uniform velocity profile needs to be ensured along the cross sectional direction at the central region of the channel. Therefore, the channel must be wide enough with the given height of the channel. Simple simulations show that a cross section of 2 mm × 20 mm was adequate in our study. Second, the channel needs to be long enough to prevent the effect of the entrance region so that a well-defined velocity profile can be predicted in the region around the stainless steel strip. With our test conditions, a channel length of 160 mm was found to be appropriate according to a classical entrance length formula [76].

Table 5.1 Test parameters – wall shear stress measurement

	Volume flow rate	Mean flow velocity	Reynolds number	Velocity gradient at wall
	(mL/s)	(m/s)		(1/s)
1	0	0	0	0
2	9.8	0.245	551	735
3	21	0.525	1180	1575

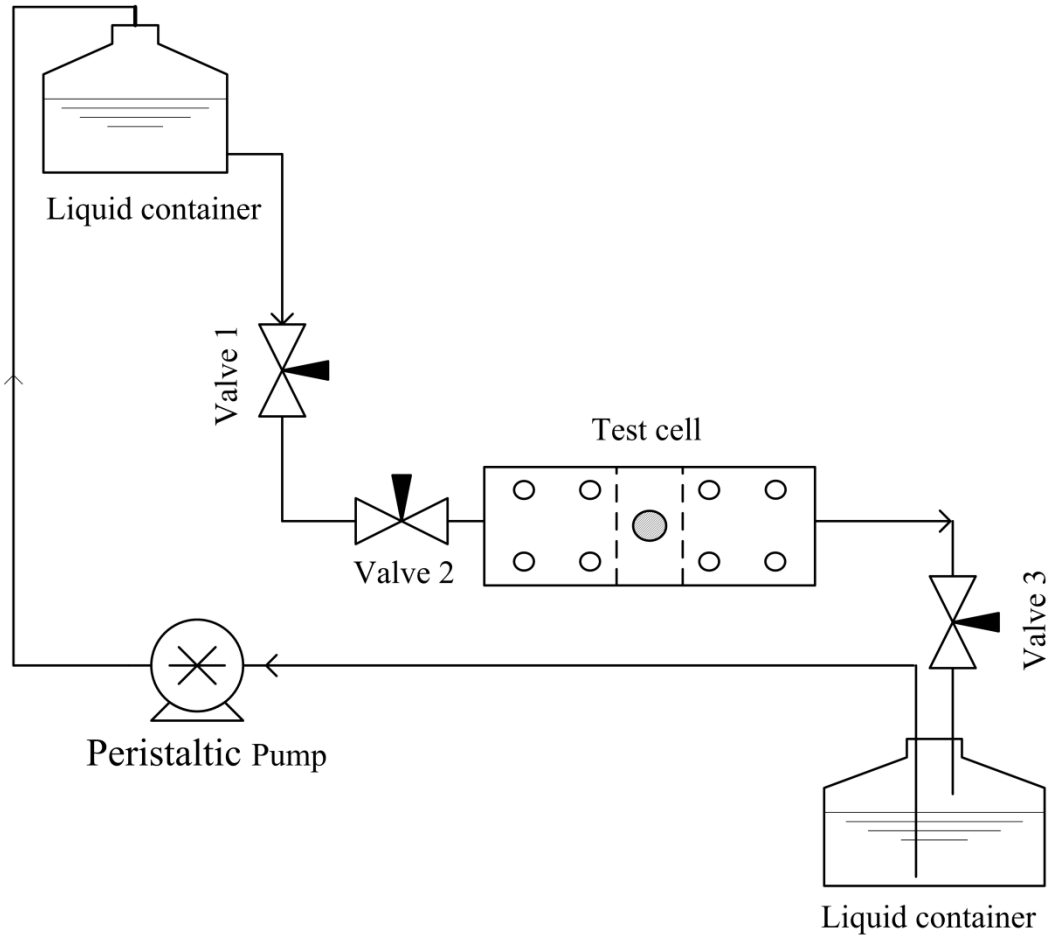

Figure 5.12 Schematic of the flow loop – Experimental validation of the wall shear stress measurement

Figure 5.12 is the schematic diagram of the flow loop which provides the flow to the test cell. An upstream tank, which was approximately 1 m higher than the test cell, provided the pressure head. Three valves on the delivery tubes were adjusted to supply two different mass flow rates, as shown in Figure 5.12. A downstream tank received the water flow from the test cell and a small pump lifted water from the downstream tank back to the upstream tank. The mass flow rate was measured using a graduated cylinder and a stop watch. Two volume flow rates, 9.8 mL/s and 21 mL/s, were tested in this

experiment. The mean velocity of the flow was calculated from the mass flow rate measured. The characteristic length for the Reynolds number was the height of the channel. Reynolds number (from zero to 1200) implies a laminar flow inside the channel and therefore, the velocity gradient at the wall was calculated based on a parabolic velocity profile in the channel [76]. Table 5.1 gives the test parameters based on the flow rate and the cross section of the channel. For every flow rate, data for three different operating frequencies, 202, 302, and 402 Hz, were tested and recorded.

5.2.2 Test Results

The recorded temperature signal was the AC component as discussed in Chapter Four. During the measurement of the temperature signal using the lock-in amplifier, all three valves on the test line were open and a constant mass flow rate was maintained by the constant pressure head from the upstream tank. Two different flow rates were obtained by adjusting two valves of the three valves. Due to the limited water storage capacity of the tanks, the measurements were not conducted continuously. Instead, after data for one set point was taken, one of the valves, such as Valve 3 in Figure 5.12, was fully closed and water from the downstream tank was pumped back to the upstream tank by the pump until there was enough water in the upstream tank for the next run. Then, Valve 3 was fully opened again to provide a flow rate which was the same as before. This procedure ensures the repeatability of our experiment. However, this procedure could potentially cause another problem in the measurement. According to the

discussion about the linearity in Chapter Three, the total solution can be decoupled into AC and DC parts from the AC and DC heating source terms or boundary conditions. The DC part of the solution will decay to the steady-state solution and has no effect on the measured temperature signal of the AC part. In the study of liquid thermal conductivity as presented in Chapter Four, no transient part of the solution was involved in the temperature signal measurement since it was always steady state during the experiment. Changing of the operating frequency will not cause a different steady-state solution. However, a change of the flow rate, or a change in the velocity gradient, will lead to a different steady-state state. During the process of changing the flow rate, a transient solution will occur. The measured temperature signal will not only contain the AC part, but also the transient part. Therefore, from opening Valve 3 again to taking the measurement, we need to have a time period to ensure that the transient solution decays to the steady-state solution. In our experiment, a five-minute period was used.

The maximum amplitude of the temperature oscillation was approximately 0.1°C at the lower end of the frequency range. According to steady-state heat convection in the two-dimensional channel flow, the absolute temperature on the stainless steel surface for the DC component was about 25°C.

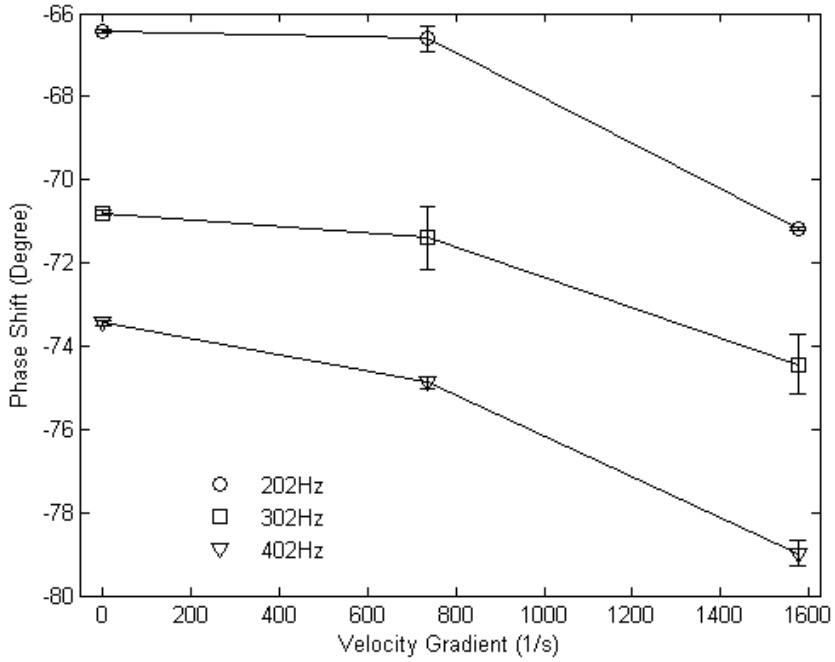

Figure 5.13 Wall shear stress experimental results – phase shift of the temperature signals vs. velocity gradient

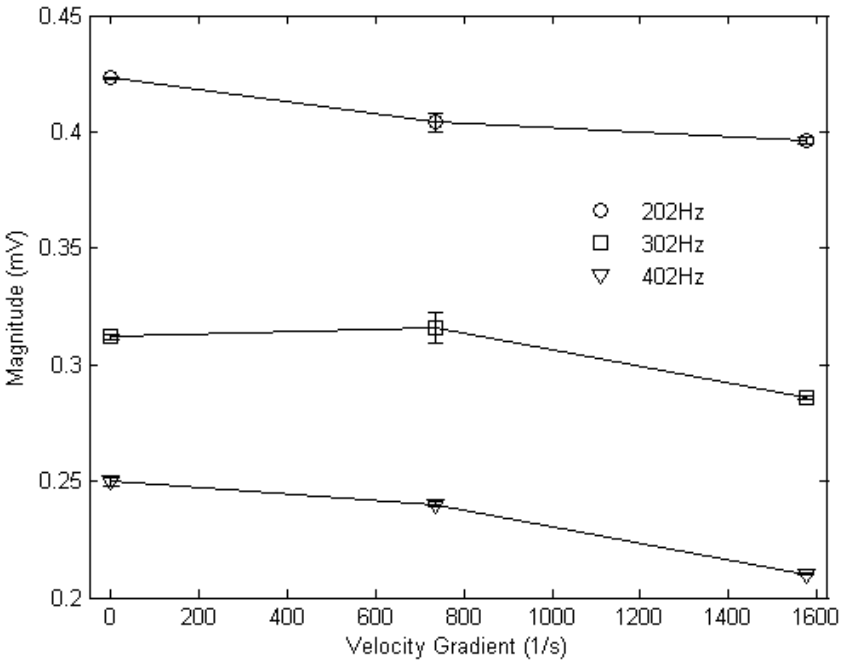

Figure 5.14 Wall shear stress experimental results – magnitude of the temperature signals vs. velocity gradient

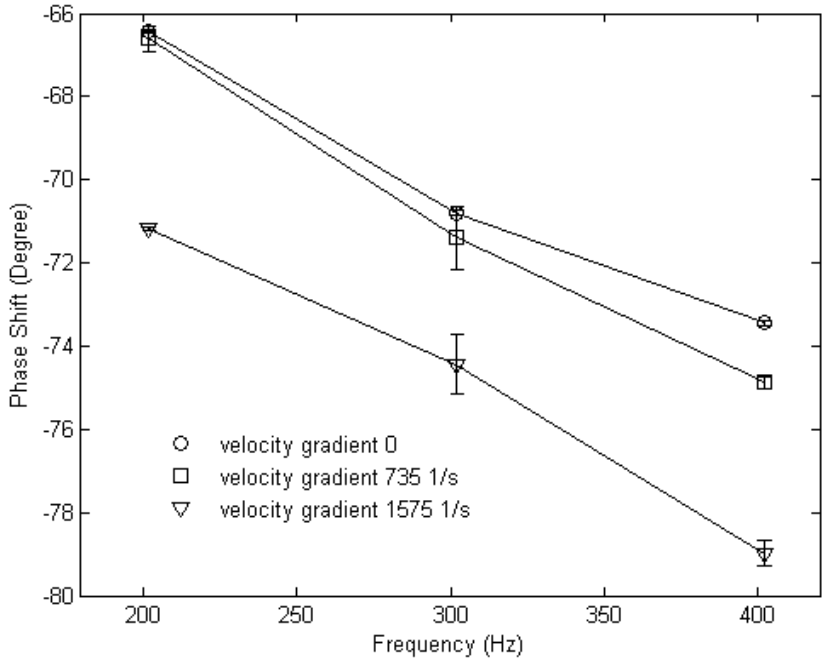

Figure 5.15 Wall shear stress experimental results – phase shift of the temperature signals vs. frequency

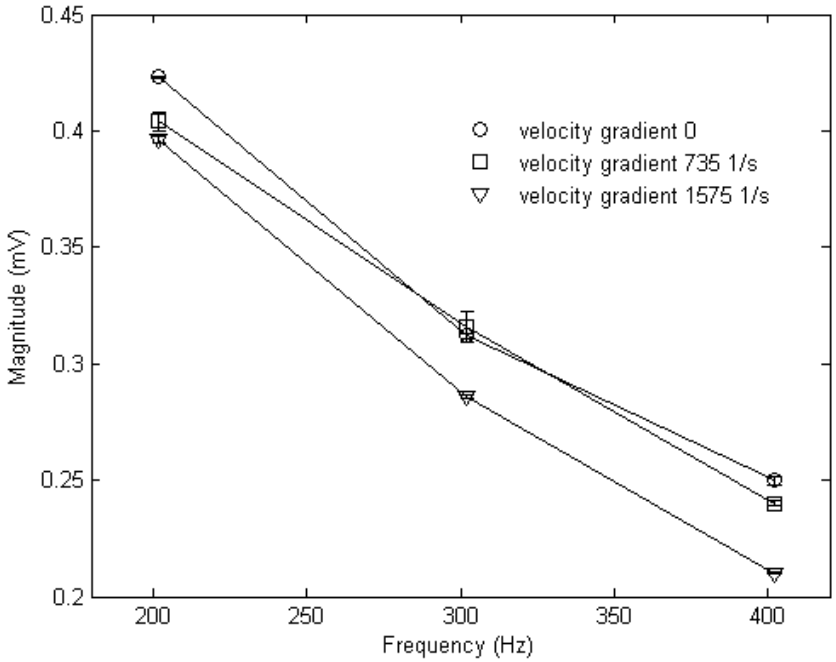

Figure 5.16 Wall shear stress experimental results – magnitude of the temperature signals vs. frequency

Figure 5.13 is the experimental results for the phase information. The trend of the phase shift varying with the velocity gradient is similar to that of the magnitude. The phase shift declines with the increasing velocity gradient. The higher operating frequency corresponds to the lower phase shift given the same velocity gradient. However, the sensitivity of the phase signal to the velocity gradient tends to be reasonably high compared with that of the magnitude signal, and suggests that the phase shift could be used in wall shear stress measurements. The standard deviation of the measurements is also displayed on the figure. The data at the operating frequency of 302 Hz shows a large standard deviation. However, our experimental data still show a strong dependence of the phase shift on the velocity gradient.

Fig. 5.14 shows how the magnitude of the temperature signal varies with the velocity gradient under different operating frequencies. The higher the operating frequency, the lower the magnitude is. Under the same operation frequency, the magnitude decreases with the increasing velocity gradient. It can also be noted that the sensitivity of the magnitude to the velocity gradient is not high although a high operating frequency seems to lead to higher sensitivity. The standard deviation of the magnitude is very low in our measurements.

Figure 5.15 and 5.16 present the experimental data from another perspective. The curves with the zero velocity gradient will be the same as that in the study of liquid thermal conductivity. Figure 5.15 shows the magnitude of the temperature signal. This magnitude declines rapidly with increasing operating frequency. Figure 5.16 is the phase shift of the temperature signal under various velocity gradients. Clearly shown in Figure

5.15 and 5.16, is one interesting fact that the temperature signals, both the magnitude and phase shift, do not vary much from the zero velocity gradient to the velocity gradient of 735 1/s. However, the temperature signal at the velocity gradient of 1575 1/s, especially the phase shift, demonstrates strong divergence from that at zero and 735 1/s velocity gradients.

5.2.3 Discussion

The assumption of the linear velocity profile on the heating strip needs further discussion. The strategy to understand this issue is to compare the penetration depth of the thermal wave to the velocity profile in the flow channel. Based on the thermal properties of water and the operating frequency in our experiment, the penetration depth of the thermal wave in our test is about 10 micrometers given that the operating frequency is 202 Hz. With a higher operating frequency, the formula of the thermal wave penetration depth will give a lower value, as discussed in Chapter Three. The Reynolds number of the channel flow in our experiment implies a laminar flow pattern as shown in the last section. Since the flow channel has a high aspect ratio as discussed in Section 5.2.1, the flow pattern at the center of the channel can be approximated as a two-dimensional flow with a parabolic velocity profile. Further, since the height of the channel is 2 mm and much higher than the thermal wave penetration depth, it will be reasonable to assume that the flow velocity profile near the wall can be approximated as a linear velocity profile. If the thickness of this linear velocity gradient region is larger

than the thermal wave penetration depth, the velocity gradient at the wall can be considered as the only flow parameter that could have impact on the temperature signal.

The parabolic velocity profile in the laminar channel flow implies that the change in the velocity gradient will be proportional to the change in the distance in the channel height direction. As mentioned above, the thermal wave penetration depth is only about 10 μm. Therefore, a thickness of the linear velocity gradient region which is of the same order of magnitude as that of the penetration depth can be found in our channel flow. Figure 5.17 (a) shows that the height of the channel is much larger than the penetration depth of thermal wave. This fact suggests that under the steady state DC part of the solution, the sustained part of the solution will be limited in the region with a characteristic length of the penetration depth. As shown in Figure 5.17 (b), with appropriate approximation, the thickness of the linear velocity gradient region is larger than the penetration depth with our channel geometry and the operating frequency in the experiment. Therefore, the linear velocity profile assumption in our experimental study should be valid in light of the above discussion.

Another important issue that needs our attention is about the edge effect of the delrin plate on the stainless steel strip. As discussed in Chapter Four, the contact between the delrin plate and the stainless steel strip will make the one-dimensional assumption problematic in the study of the liquid thermal conductivity measurement. The width of the stainless steel strip needs to be large enough to ensure that the temperature response at the center of the stainless steel strip is not influenced by the heat conduction from the edge. A procedure has been developed to find the central location

of the stainless steel strip for determining the location of the temperature signal measurement as discussed in Chapter Four.

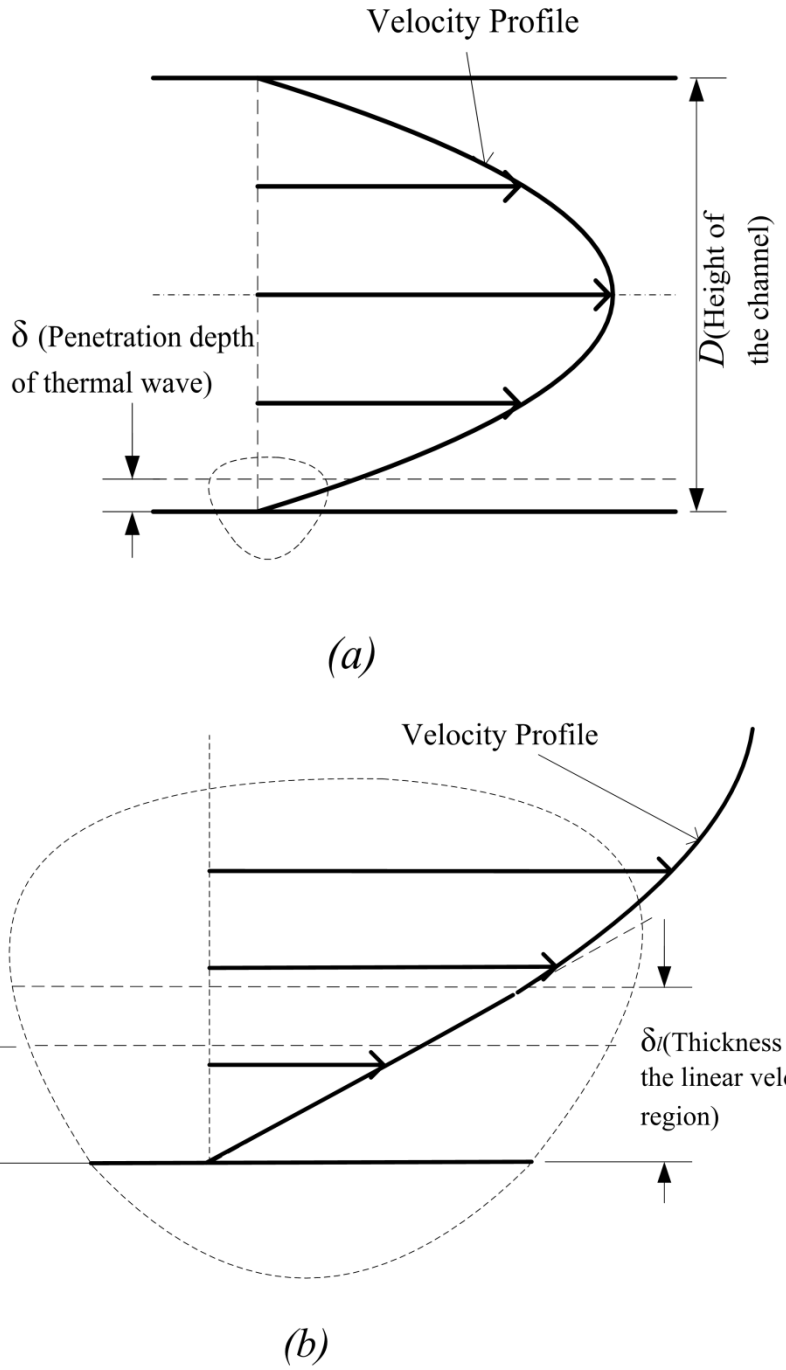

Figure 5.17 Penetration depth of thermal wave vs. thickness of the linear velocity region. (a) Velocity profile in the laminar channel flow; (b) Velocity profile near the wall.

In the case of the wall shear stress study, the existence of the flow field on the stainless steel strip implies that the above procedure of finding the central point will not be applicable. Meanwhile, the distribution of the temperature signal on the stainless steel strip will vary depending on different operating frequencies. The measured temperature signal from the infrared detector is a synthesized signal on the stainless steel strip. All the above factors suggest that this current experimental study is at its early stage and more works need to be done to relate the measured temperature signal to the wall shear stress.

6. CONCLUSIONS AND FUTURE WORKS

This dissertation covers two research topics which are based on similar heat transfer phenomenon. First is to extend the previous study of material thermal property characterization from solid to the liquid material domain. Second is utilization of the thermal wave approach for flow property measurement near surfaces.

6.1 NANOFLUIDS THERMAL CONDUCTIVITY MEASUREMENTS

Heat transfer enhancement study of nanofluids demands new and independent experimental techniques for thermal property determination. Previous experimental studies of nanofluids thermal conductivity show inconsistent results and the dominant experimental technique is the transient hot-wire method. In this thesis, a phase detection technique based on the thermal wave approach is developed to measure the thermal conductivities of liquids with application of nanofluids. A periodic Joule heating source generated from a time-varying electrical current passing through a thin stainless steel strip produces a temperature fluctuation on the front surface of the stainless steel strip. An infrared detector monitors this temperature fluctuation on the front surface. The temperature signal is recorded by both an oscilloscope and a lock-in amplifier, the latter of which gives magnitude and phase information about the signal. A one-dimensional, two-layered transient heat conduction model was developed to predict the temperature response on the front surface of the stainless steel strip. This temperature response,

including the phase and magnitude, is a function of the thermal properties of the measured liquid. The phase information shows high sensitivity to the change of thermal properties of the liquid layer and is employed to match experimental data to find thermal conductivities. The validity of this measurement technique is assessed by using water and ethylene glycol. A gold nanolfuid with a concentration of 0.058 g/L and average particle size of 4.5 nm is also tested.

Results show about 30% enhancement of thermal conductivity compared with that of the base fluid. One interesting fact in our measurement results is that the thermal transport behavior of the nanofluids is different from that of pure liquids. At low frequency in our experiment, higher effective thermal conductivity was found by matching the experimental data to the model. The study of heat transfer enhancement of nanofluids in channel flow convection and our experimental data imply a potential relationship between the effective thermal conductivity of nanofluids and the temperature gradient.

Our work suggests a need for carefully examining the role of the measurement techniques in the heat transfer experimental study of nanofluids. The experimental technique developed in this dissertation can offer a good reference for the conventional transient hot-wire method in the study of nanofluid thermal conductivity. Also, it provides important experimental information that cannot be provided by the transient hot-wire method, such as the different thermal transport performance under different operating frequencies. Combined with theoretical studies, these results can help explore the heat transfer mechanism of nanofluids. Our experimental study could be important

for building an empirical formula of effective thermal conductivity and expediting the process of nanofluid applications in heat transfer, as well.

Based on the above discussion, one plan for future work in this area should be the study of the temperature gradient effect on the thermal conductivity enhancement. The systematic study in this direction may help elucidate the problem of inconsistent experimental data from different groups and different techniques. One example will be to measure the effective thermal conductivity of nanofluids under different power levels using the transient hot-wire method. The resultant data can be compared with those from the phase-sensitive technique developed in this thesis.

Another important issue in the current theoretical study of nanofluid heat transfer mechanisms is that the Brownian motion of nanoparticles in the base fluid is proposed to be the main mechanism of heat transfer enhancement. The capability of decoupling the DC and AC part of the heating source in our experimental technique provides a good tool for the study of this topic. Running the test under different temperatures using our phase-sensitive technique can easily separate the effect of temperature and temperature gradient on the effective thermal conductivity. This type of study can provide valuable experimental data for exploration of nanofluid heat transfer mechanisms.

6.2 WALL SHEAR STRESS MEASUREMENTS

Measurements of the wall shear stress could have significant impact on both fundamental research and industry application. The traditional thermal shear stress

sensors are based on the simple heat convection principle and have several drawbacks which prevent this kind of sensor from wider application. Emerging micromachining techniques are thought to provide solutions for the problems of thermal shear stress sensors. Although the small time and length scale of MEMS-based sensors do improve the performance of shear stress measurements in terms of spatial and temporal resolution and sensitivity, fundamental limitations, such as temperature drift and thermal interaction between the heater and the support structure, are not resolved.

A wall shear stress measurement approach independent of the temperature magnitude is proposed in this work. The basic principle of this phase-sensitive thermal sensor is: by imposing a periodic heating flux with a known frequency on the wall surface, the responding wall temperature signal at the same frequency will not be at the same phase as the heating signal. This phase shift will be a strong function of the flow velocity gradient on the wall when the heating signal is in a certain frequency range and can be used to indicate the level of wall shear stress measured. This approach utilizes the phase shift, rather than magnitude, of the temperature signal as the primary measured quantity for wall shear stress. Decoupling the AC part from the DC part of the heat transfer solution offers flexibility in sensor design through thermal management.

In this study, a wall shear stress sensor design with a heater and two temperature sensors on a silicon dioxide substrate is analyzed. The heater with a periodic heating source generates a temperature oscillation field which interacts with the flow field. The two temperature sensors pick up the temperature response that contains the information on the velocity gradient at the wall. Based on the above sensor design, a two-

dimensional conjugate heat convection model is developed with a periodic heating flux at the solid/fluid interface and a linear velocity profile in the fluid domain. Two designs are studied, one with a silicon heat sink under the silicon dioxide substrate and another without the heat sink. The effects of the two main design parameters, the operating frequency and the distance between the heater and the temperature sensor, are discussed. A reasonable sensitivity of the phase information to the velocity gradient suggests a practical sensor design.

A preliminary experimental test is conducted to prove the concept of utilizing the thermal wave approach for the measurement of wall shear stress. A thin stainless steel strip adjacent to a flow field of water is heated by a periodic current. Different mass flow rates in the channel lead to different velocity gradients on the surface of the stainless steel strip. The temperature signal at the other surface of the stainless steel strip is monitored by an infrared detector. The experimental results show a dependence of the phase shift of the temperature signal on the mass flow rate. Due to the thin penetration depth of the thermal wave in our case, the results suggest that the phase information could be used for the measurement of wall shear stress.

Future work in the area of wall shear stress measurement would be to construct a MEMS wall shear stress sensor using microfabrication technology as described above and conduct field testing. The heater can be constructed using a thin film of Nichrome deposited by Physical Vapor Deposition (PVD). Temperature sensors could be either thermocouples or RTDs. The two important experimental parameters are the operating frequency and the distance between the heater and the sensor. The experimental

procedure can start from the thermal property characterization described in Chapter Four to calibrate the experimental apparatus. The second step shall be utilizing the channel flow for wall shear stress measurement for both laminar and turbulent flows. At this stage, the estimation of the thermal wave penetration depth can be important to ensure the validity of the linear velocity profile assumption. The third step could be field testing of the boundary layers, on a flat plate or airfoil. This type of research will be important for separation control of low-Reynolds-Number laminar flow.

BIBLIOGRAPHY

[1] Zhang, X., C.P. Grigoropoulos, 1995, "Thermal Conductivity and Diffusivity of Free-Standing Silicon Nitride Thin Films", Rev. Sci. Instrum., **66**, pp.1115-1120

[2] Indermuehle, S.W., R.B. Peterson, 1999, "A Phase-Sensitive Technique for the Thermal Characterization of Dielectric Thin Films," ASME J. Heat Transfer, **121**, pp. 528-536

[3] Chen, G., C.L. Tien, X. Wu, J.S. Smith, 1994, "Thermal Diffusivity Measurement of GaAs/AlGaAs Thin-Film Structures", ASME J. Heat Transfer, **116**, pp. 325-331

[4] Garimella, S.V., and C.B. Sobhan, 2003, "Transport in Microchannels – A Critical Review," Annu. Rev. of Heat Transfer, **13**, pp. 1-50

[5] Masuda,H., A. Ebata, K. Teramae, N. Hishinuma, 1993, "Alteration of Thermal Conductivity and Viscosity of Liquid by Dispersing Ultra-Fine Particles," Netsu Bussei, **7**, No.4, pp. 227–233

[6] Choi, U.S., 1995, "Enhancing Thermal Conductivity of Fluids with Nanoparticles, Developments and Applications of non-Newtonian Flows," eds. D.A. Siginer and H. P. Wang, The American Society of Mechanical Engineers, New York, FED – Vol. 231/MD – Vol.66, pp. 99-105

[7] Keblinski, P., S.R. Phillpot, S.U.S. Choi, J.A. Eastman, 2002, "Mechanisms of Heat Flow in Suspensions of Nano-sized Particles (Nanofluids)", Int. J. Heat Mass Transfer, **45**, pp. 855-863

[8] Maxwell, J.C., 1873, *Electricity and Magnetism*, Clarendon Press, Oxford, UK

[9] Lee, S., S.U.S. Choi, S. Li, J.A. Eastman, 1999, "Measuring Thermal Conductivity of Fluids Containing Oxide Nanoparticles," ASME J. Heat Transfer, **120**, pp. 280-289

[10] Zhang, X., H. Gu, M. Fujii, 2006, "Experimental Study on the Effective Thermal Conductivity and Thermal Diffusivity of Nanofluids," Int. J. Thermophys., **27**, pp. 569-580

[11] Das, S.K., N. Putra, P. Thiesen, W. Roetzel, 2003, "Temperature Dependence of Thermal Conductivity Enhancement for Nanofluids," ASME J. Heat Transfer, **125**, pp. 567-574

[12] Putnam, S. A., D. G. Cahill,; P. V. Braun, Z. Ge, R. G. Shimmin, 2006, "Thermal Conductivity of Nanoparticle Suspensions," J. Appl. Phys., **99**, pp. 084308-1~6

[13] Naughton, J. W., M. Sheplak, 2002, "Modern Developments on Shear-Stress Measurement", Progress in Aerospace Sciences, **38**, pp.515–570

[14] Murshed, S.M.S, K.C. Leong, C. Yang, 2006, "Determination of the Effective Thermal Diffusivity of Nanofluids by the Double Hot-wire Technique", J. Phys. D: Applied Physics, **29**, pp. 5316-5322

[15] Eastman, J.A., S. Choi, S. Li, W. Yu, L.J. Thompson, 2001, "Anomalously Increased Effective Thermal Conductivities of Ethylene Glycol-based Nanofluids Containing Copper Nanoparticles," Appl. Phys. Lett., **78**, pp. 718-720

[16] Choi, S.U.S., Z.G. Zhang, W. Yu, F.E. Lockwood, E.A. Grulke, 2001, "Anomalous Thermal Conductivity Enhancement in Nano-tube Suspension," Appl. Phys. Lett., **79**, pp. 2252-2254

[17] Liu, M.S., M. Lin, I.T. Huang, C.C. Wang, 2006, "Enhancement of Thermal Conductivity with CuO for Nanofluids," Chem. Eng. Technol., **29**, pp. 72-77

[18] Liu, M., M. Lin, C.Y. Tsai, C.C. Wang, 2006, "Enhancement of Thermal Conductivity with Cu for Nanofluids Using Chemical Reduction Method," Int. J. Heat Mass Transfer, **49**, pp. 3028-3033

[19] Bang, I.C., S.H. Chang, 2005, "Boiling Heat Transfer Performance and Phenomena of Al_2O_3 – Water Nano-Fluids from a Plain Surface in a Pool," Int. J. Heat Mass Transer, **48**, pp. 2407–2419

[20] Vassallo, P., R. Kumar, S. D'Amico, 2004, "Pool Boiling Heat Transfer Experiments in Silica-Water Nano-Fluids", Int. J. Heat Mass Transer, **47**, pp. 407–411

[21] Wang, Z.L., D.W. Tang, S. Liu, X.H. Zheng, N. Araki, 2007, "Thermal-Conductivity and Thermal-Diffusivity Measurements of Nanofluids by 3ω Method and Mechanism Analysis of Heat Transport", Int. J. Thermophys, **28**, pp. 1255-1268

[22] Wen, D., Y. Ding, 2004, "Experimental Investigation into Convective Heat Transfer of Nanofluids at the Entrance Region under Laminar Flow Conditions," Int. J. Heat Mass Transfer, **47**, pp. 5181–5188

[23] Lee, J., I. Mudawar, 2007, "Assessment of the Effectiveness of Nanofluids for Single-Phase and Two-Phase Heat Transfer in Micro-Channels," Int. J. Heat Mass Transfer, **50**, pp. 452–463

[24] Kim, S.H., S. R. Choi, D. Kim, 2007, "Thermal Conductivity of Metal-Oxide Nanofluids: Particle Size Dependence and Effect of Laser Irradiation", ASME J. Heat Transfer, **129**, pp. 298–307

[25] Vadas, P., 2006, "Heat Conduction in Nanofluid Suspensions", ASME J. Heat Transfer, **128**, pp. 465- 477

[26] Jang, S.P., S.U.S. Choi, 2004, "Role of Brownian Motion in the Enhanced Thermal Conductivity of Nanofluids, Appl. Phys. Lett. **84**, pp. 4316-4318

[27] Xie, H., M. Fujii, X. Zhang, 2003, "Effect of Interfacial Nanolayer on the Effective Thermal Conductivity of Nanoparticle-fluid Mixture," Int. J. Heat Mass Transfer, **48**, pp.2926-2932

[28] Patel, H.E., S.K. Das, T. Sundararajan, A.S. Nair, B. George, T. Pradeep, 2003, "Thermal Conductivities of Naked and Monolayer Protected Metal Nanoparticle Based Nanofluids: Manifestation of Anomalous Enhancement and Chemical Effects," Appl. Phys. Lett., **83**, pp. 2931-2933

[29] Zhu, H., C. Zhang, S. Liu, Y. Tang, Y. Yin, 2006, "Effects of Nanoparticles Clustering and Alignment on Thermal Conductivities of Fe3O4 Aqueous Nanofluids," Appl. Phys. Letts., **89**, pp. 023123-1–3

[30] Buongiorno, J., 2006, "Convective Transport in Nanofluids," ASME J. Heat Transfer, **128**, pp. 240-250

[31] Prasher, R., P. Bhattacharya, P.E. Phelan, 2005, "Thermal Conductivity of Nanoscale Colloidal Solutions (Nanofluids)," Phys. Rev. Letts., **94**, 025901

[32] Eapen,J., W.C. Williams, J. Buongiorno, L. Hu, S. Yip, 2007, "Mean-Field Versus Microconvection Effects in Nanofluids Thermal Conduction", Phys. Rev. Letts, **99**, pp. 095901-1–4

[33] Healy, J.J., J.J. deGroot, J. Kestin, 1976, "The Theory of the Transient Hot-Wire Method for Measuring Thermal Conductivity", Physica, **82C**, pp. 392-408

[34] Putnam, S.A., D.G.Cahill, 2004, "Micron-Scale Apparatus for Measurements of Thermodiffusion in Liquids," Rev. Sci. Instrum., **75**, pp.2368–2372

[35] Cahill, D.G., 1989, "Thermal Conductivity Measurement from 30 to 750 K: 3ω method," Rev. Sci. Instrum., **61**, pp.802–808

[36] Borca-Tasciuc, D.-A., G. Chen, 2005, "Anisotropic Thermal Properties of Nanochanneled Alumina Templates," J. Appl. Phys., **97**, pp. 084303-1–9

[37] Borca-Tasciuc, T., Kumar, A.R., G. Chen, 2001, "Data Reduction in 3ω method for thin-film thermal conductivity determination," Rev. Sci. Intrum., **72**, pp. 2139–2147

[38] Bodzenta, J., 2008, "Thermal Wave Methods in Investigation of Thermal Properties of Solids", Eur. Phys. J. Special Topic, **154**, pp. 305-311

[39] Angstrom, A. J., 1861, Neue Methode das Warmeleitungsvermogen der Korper zu. bestimmen. Ann. Phys. Chem., **114**, pp. 513-530

[40] Saenger, K.L., 1989, "An Interferometric Calorimeter for Thin-Film Thermal Diffusivity Measurements", J. Appl. Phys., **65**, pp.1447 – 1452

[41] DeVecchio, D., D.Russell, P. Taborek, 1995, "Measurement of Thermal Diffusivity of Small, High Conductivity Samples Using a Phase Sensitive Technique", Rev. Sci. Instrum, **66**, pp. 3601–3605

[42] Yang, G., A.D. Migone, K.W. Johnson, 1991, "Automated Apparatus for the Determination of the Specific Heat and the Thermal Diffusivity of Nonconducting Solids Using ac Techniques", Rev. Sci.Instrum., **62**, pp. 1836-1839

[43] Yu, X.Y., L. Zhang, G. Chen, 1996, "Thermal-Wave Measurement of Thin-Film Thermal Diffusivity with Different Laser Beam Configurations," Rev. Sci. Instrum, **67**, pp. 2312–2316

[44] Lin, Q., F. Jiang, X-Q, Wang, Y. Xu, Z. Han, Y-C. Tai, J. Lew, C-M. Ho, 2004, "Experiments and Simulations of MEMS Thermal Sensors for Wall Shear-Stress Measurements in Aerodynamic Control Applications," J. Micromech. Microeng., **14**, pp.1640–1649

[45] Xu, Y., F. Jiang, S. Newbern, A. Huang, C-M. Ho, Y-C. Tai, 2003, "Flexible Shear-Stress Sensor Skin and its Application to Unmanned Aerial Vehicles," Sensors and Actuators A, **105**, pp. 321–329

[46] Schobeiri, M.T., B. Ozturk, D. E. Ashpis, 2003, "On the Physics of Flow Separation along a Low Pressure Turbine Blade under Unsteady Flow Conditions," Proceeding of the ASME turbo Expo 2003, Atlanta, Georgia, USA

[47] Le Page, Y.G., K.W. Holappa, 2000, "Hydrodynamics of an Autonomous Underwater Vehicle Equipped with a Vectored Thruster," Oceans 2000 MTS/IEEE Conference and Exhibition, **3**, pp. 2135–2140

[48] Dorgan, A.J., E. Loth, E. Frazzoli, 2005, "Autonomous Control of Micro Aircraft Vehicle Falling through an Atmospheric Boundary Layer," AIAA J., **43**, pp. 768–775

[49] Soundararajan, G., M. Rouhanizadeh, H. Yu, L. DeMaio, E.S. Kim, T.K. Hsiai, 2005, "MEMS Shear Stress Sensors for Microcirculation," Sensors and Actuators A, **118**, pp. 25–32

[50] Haritonidis, J.H., 1989, "The Measurement of Wall Shear Stress", in *Advances in Fluid Mechanics Measurements*, edited by M. Gad-el-Hak, Spring-Verlag, pp. 229–261

[51] Fernholz, H.H., G. Janke, M. Schober, P.M. Wagner, D. Warnack, 1996, "New Developments and Applications of Skin-Friction Measuring Techniques", Meas. Sci. Technol., **7**, pp. 1396–1409

[52] Barlian, A.A., S. Park, V. Mukundan, B.L. Pruitt, 2006, "Design and Characterization of Microfabricated Piezoresistive Floating Element-Based Shear Stress Sensors," Sensors and Actuators A, **134**, pp. 77–87

[53] Preston, J.H., 1954, "The Determination of Turbulent Skin Friction by Means of Pitot Tubes," J. Royal Aeronaut. Soc., 58, pp. 109–121

[54] Winter, K.G., 1977, "An Outline of the Techniques Available for the Measurement of Skin Friction in Turbulent Boundary Layers," Prog. Aerospace Sci., **18**, pp. 1–57

[55] Hanratty, T.J., J.A. Campbell, 1983, "Measurements of Wall Shear Stress" in Fluid Mech. Measurements, (ed. R.J. Goldstein). Hemisphere Publ. Corp., pp. 559–615

[56] Tanner, L.H., L.G. Blows, 1975, "A Study of the Motion of Oil Films on Surfaces in Air Flow, with Application to the Measurement of Skin Friction", J. Phys. E., **9**, pp. 194-202

[57] Fourguette, D., D. Modarress, F. Taugwalder, D. Wilson, M. Koochesfahani, M. Gharib, 2001, "Miniature and MOEMS Flow Sensors," AIAA Paper, 2001-2982

[58] Goldstein, S., 1996, *Fluid Mechanics Measurements*, 2nd ed. (New York: Hemisphere)

[59] Tucker C., N. Chen, J. Engel, Y. Yang, S. Pandya, C. Liu, 2006, "High-Sensitivity Bi-Directional Flow Sensor Based on Biological Inspiration of Animal Haircell Sensors", IEEE Sensors Conference, Korea

[60] Schmidt, M.A., R. T. Howe, S. D. Senturia, J. H. Haritonidis, 1988, "Design and Calibration of a Microfabricated Floating-Element Shear-Stress Sensor," IEEE Trans. Electron Devices, **35**, pp. 750–757

[61] Shajii, J., K.Y. Ng, M.A. Schmidt, 1992, "A Microfabricated Floating-Element Shear-Stress Sensor Using Wafer-Bonding Technology," J. Microelectromech. Syst., **1**, pp. 89–94

[62] Jiang, Z., V. Modi, K.R. Farmer, Jr., 2005, "A Microfabricated Wall Shear-Stress Sensor with Capacitative Sensing," J. Microelectromech. Syst., **14**, pp. 167–175

[63] Pan, T., D. Hyman, M. Mehregany, E. Reshoko, S. Garverick, 1999, "Microfabricated Shear Stress Sensors: 1. Design and Fabrication," AIAA J., **37**, pp. 66–72

[64] Hyman, D., T. Pan, E. Reshoko, M. Mehregany, 1999, "Microfabricated Shear Stress Sensors: 2. Testing and Calibration," AIAA J., **37**, pp. 73–78

[65] Padmanabhan, A., H. Goldberg, K. D. Breuer, M. A. Schmidt, 1996, "A Wafer-Bonded Floating Element Shear Stress Microsensor with Optical Position Sensing by Photodiodes," J. Microelectromech. Syst., **5**, pp. 307–315

[66] Jiang, Z., V. Modi, 2001, "Near Wall Measurements for a Turbulent Impinging Slot Jet," ASME J. Fluid Engr., **123**, pp. 112–120

[67] Chao, J., W. Shyy, S.S. Thakur, M. Sheplak, R. Mei, 2005, "Effect of Conjugate Heat Transfer on MEMS-Based Thermal Shear Stress Sensor," Numer. Heat Transfer A, **48**, pp. 197–217

[68] Sheplak, M., V. Chandrasekaran, A. Cain, T. Nishida, L.N. Cattafesta, 2002, "Characterization of a Silicon-Micromachined Thermal Shear-Stress Sensor," AIAA J., **40**, pp. 1099–1104

[69] Chandrasekaran, V., A.Cain, T. Nishida, L. N. Cattafesta, M. Sheplak, 2005, "Dynamic Calibration Technique for Thermal Shear-Stress Sensors with Mean Flows," Experiments in Fluids, **39**, pp. 56–65

[70] Xu, Y., Q. Lin, G. Lin, R.B. Katragadda, F. Jiang, S. Tung, Y-C. Tai, 2005, "Micromachined Thermal Shear-Stress Sensor for Underwater Applications," J. Microelectromech. Syst., **14**, pp. 1023–1030

[71] Schlichting, H., K. Gersten, 2000, *Boundary-Layer Theory*, 8th ed., Springer

[72] Myers, G.E., 1998, *Analytical methods in conduction heat transfer*, 2nd ed., AMCHT, Madison, WI

[73] Goldstein, S., 1996, *Fluid Mechanics Measurements*, 2nd ed., New York: Hemisphere

[74] Incropera, F.P., D.P. Dewitt, T.L. Bergman, 2006, *Fundamental of heat and mass transfer*, 6th ed., Wiley, John & Sons

[75] Jackson, J.E., B.V. Borgmeyer, C.A. Wilson, P. Cheng, J.E. Bryan, 2006, "Characteristics of Nucleate Boiling with Gold Nanoparticles in Water," Proceedings of IMECE2006, ASME international mechanical engineering congress and exposition, Nov. 5–10, Chicago, IL

[76] Fourguette, D., Gonzalez, P. Modarress, D., Arik,E., Wilson, D., Koochesfahani, M., 2004, "Optical Measurement of Wall Shear Stress with Emphasis on Flows Near Separation," 24th AIAA Aerodynamic Measurement Technology and Ground Testing Conference, Portland, OR

[77] Chu, D., Wong, W.K., Goodson, K.E., Pease, R.F. W., "Transient Temperature Measurements of Resist Heating Using Nanothermaocouples," J. Vac. Sci. Technol., **B21**, 2003, pp. 2985 – 2989

[78] Zhang, X., Choi, H., Datta, A., and Li, X., 2006, "Deaign, Fabrication and Characterization of Metal Embedded Thin Film Thermocouples with Various Film Thicknesses and Junction Sizes," J. Micromech. Microeng., **16**, pp. 900 – 905

[79] Choi, H., Li, X., 2007, "Fabrication and Application of Micro Thin Film Thermocouples for Transient Temperature Measurement in Nanosecond Pulsed Laser Micromachining of Nickel," Sensors and Actuators A, **136**, pp. 118 - 124

APPENDICES

APPENDIX A

One-Dimensional Conduction Code

```
% Self-heating source layer model for stainless steel layer

clear all;

% Define the thickness of the stainless steel layer on the substrate

L=12.5e-6;

% The depth of the water

Dep=1e-3;

% Define the thermal properties of the layers

k1=15.1;     %Thermal conductivity of stainless steel
k2=0.826;    %Thermal conductivity of water
rh1=8055;   %Density of stainless steel
rh2=1000;   %Density of water
cp1=480;    %Heat capacity of stainless steel
cp2=4160;   %Heat capacity of water

%Define the parameters from the above primary variables

a1=k1/(rh1*cp1);    %Thermal diffusivity of stainless steel
a2=k2/(rh2*cp2);    %Thermal diffusivity of water

%Define the oscillating frequency of the heat flux, frequency unit is
%radian

n=100;
fs=20;   % Starting frequency
fe=500;    % Ending frequency;
f=linspace(fs,fe,n);
ome=linspace(2*fs*pi,2*fe*pi,n);

%Define the complex variables xi

x1=((ome./a1).*i).^0.5;
x2=((ome./a2).*i).^0.5;

%Define the heat source term

G0=0.56e9*a1./(i.*ome.*k1);
```

```
% Calculate A1 and B1.

for p=1:n
   T1=exp(-x1(p)*L)+exp(x1(p)*L);
   T2=(k1*x1(p))/(k2*x2(p));
   T3=exp(x1(p)*L)-exp(-x1(p)*L);
   A1(p)=(-G0(p))/(T1+T2*T3);
   B1(p)=A1(p);
   A2(p)=T2*(-T3)*A1(p)/(exp(-x2(p)*L));

   % ps is the temperature at the front side of the stainless steel layer

   ps(p)=A1(p)+B1(p)+G0(p);
   mag(p)=abs(ps(p));
   ph(p)=(360/(2*pi))*angle(ps(p));

   % ps2 is the temperature at the backside of the stainless steel layer.

   ps2(p)=A1(p)*exp(-x1(p)*L)+B1(p)*exp(x1(p)*L)+G0(p);
   mag2(p)=abs(ps2(p));
   ph2(p)=(360/(2*pi))*angle(ps2(p));

   % ps22 is the temperature at the backside of the stainless steel layer but using another
formula.

   ps22(p)=A2(p)*exp(-x2(p)*L);
   mag22(p)=abs(ps22(p));
   ph22(p)=(360/(2*pi))*angle(ps22(p));

   % psw is the temperature in the water layer at 1 mm deep

   psw(p)=A2(p)*exp(-x2(p)*Dep);
   magw(p)=abs(psw(p));
   phw(p)=(360/(2*pi))*angle(psw(p));

   % xn is the estimation of the penetration depth

   xn(p)=(2*pi*a2/f(p))^(1/2);

end;

pht=transpose(ph);
magt=transpose(mag);
```

```
plot(f,ph);
hold on;
plot(f,ph2);
hold off;

%plot(f,magw);
%hold on;
%plot(f,mag,'r');
%hold on;
%plot(f,mag2,'b');
%hold off;
%plot(f,ph-ph2);
```

```
% Self-heating source layer model for stainless steel layer

clear all;

% Define the thickness of the stainless steel layer on the substrate

L=12.5e-6;

% The depth of the water

Dep=1e-3;

% Define the thermal properties of the layers

k1=15.1;     %Thermal conductivity of stainless steel
k2=0.59;    %Thermal conductivity of water
rh1=8055;   %Density of stainless steel
rh2=1000;   %Density of water
cp1=480;    %Heat capacity of stainless steel
cp2=4160;   %Heat capacity of water

%Define the parameters from the above primary variables

a1=k1/(rh1*cp1);    %Thermal diffusivity of stainless steel
a2=k2/(rh2*cp2);    %Thermal diffusivity of water

%Define the oscillating frequency of the heat flux, frequency unit is
%radian

n=100;

%fs=51;   % Starting frequency
%fe=150;    % Ending frequency;
%f=linspace(fs,fe,n);
%ome=linspace(2*fs*pi,2*fe*pi,n);

omeo=80;
for nn=1:10
   f(nn)=(2*nn-1)*omeo;
   ome(nn)=2*pi*(2*(nn-1)+1)*omeo;
end;

%Define the complex variables xi
```

```
x1=((ome./a1).*i).^0.5;
x2=((ome./a2).*i).^0.5;

%Define the heat source term

g00=0.56e9;
for t=1:nn
   g0(t)=(1/(2*t-1))*g00;
   G0(t)=g0(t)*a1./(i.*ome(t)*k1);
end;

% Calculate A1 and B1.

for p=1:nn
   T1=exp(-x1(p)*L)+exp(x1(p)*L);
   T2=(k1*x1(p))/(k2*x2(p));
   T3=exp(x1(p)*L)-exp(-x1(p)*L);
   A1(p)=(-G0(p))/(T1+T2*T3);
   B1(p)=A1(p);
   A2(p)=T2*(-T3)*A1(p)/(exp(-x2(p)*L));

   % ps is the temperature at the front side of the stainless steel layer

   ps(p)=A1(p)+B1(p)+G0(p);
   mag(p)=abs(ps(p));
   ph(p)=(360/(2*pi))*angle(ps(p));

   % ps2 is the temperature at the backside of the stainless steel layer.

   ps2(p)=A1(p)*exp(-x1(p)*L)+B1(p)*exp(x1(p)*L)+G0(p);
   mag2(p)=abs(ps2(p));
   ph2(p)=(360/(2*pi))*angle(ps2(p));

   % ps22 is the temperature at the backside of the stainless steel layer but using another
formula.

   ps22(p)=A2(p)*exp(-x2(p)*L);
   mag22(p)=abs(ps22(p));
   ph22(p)=(360/(2*pi))*angle(ps22(p));

   % psw is the temperature in the water layer at 1 mm deep

   psw(p)=A2(p)*exp(-x2(p)*Dep);
   magw(p)=abs(psw(p));
```

```
   phw(p)=(360/(2*pi))*angle(psw(p));

   % xn is the estimation of the penetration depth

   xn(p)=(2*pi*a2/f(p))^(1/2);
end;

pht=transpose(ph);
magt=transpose(mag);

t=linspace(0,0.02,500);
fnt=linspace(0,0,500);

for i=1:nn
   for j=1:500;
   ft(j)=abs(ps(i))*sin(ome(i)*t(j)+angle(ps(i)));
   end;
   fnt=fnt+ft;
end;

plot(t,fnt);
%plot(f,ph);
%plot(f,ph2);
%hold on;
%hold off;
%plot(f,magw);
%hold on;
%plot(f,mag,'r');
%hold on;
%plot(f,mag2,'b');
%hold off;
%plot(f,ph-ph2);
```

APPENDIX B

Two-Dimensional Convection Code

```
% 2D complex number conjugate heat transfer problem - for air

clear all;

% Set the length and height of the geometry we want to copmpute
% region one is substrate and region two is water

L=1.8e-3;H1=0.12e-3; H2=0.24e-3;H=H1+H2;

% Define the thermal properties of the working fluid – air

k2=0.0257;    %Thermal conductivity of air
rh2=1.205;   %Density of air
cp2=1005;   %Heat capacity of air
mu2=1.85e-5;  %viscosity of air

% Define the thermal properties of the substrate - silicon dioxide

k1=1.38;    %Thermal conductivity of silicon dioxide
rh1=2200;   %Density of silicon dioxide
cp1=740;   %Heat capacity of silicon dioxide

% Define the velocity gradient on the wall - c;

c1=0;
c2=14e4;

% Define the surface heating flux;

q0=1e6;

% The frequency being modeled

f=800; ome=2*pi*f;

%Thermal diffusivity of water and substrate

a1=k1/(rh1*cp1); a2=k2/(rh2*cp2);

% Set numbers of points in grid;

num_pts=201;
Nx=num_pts; Ny=num_pts; Ntot=Nx*Ny;
```

```
% section one Ny1 and section two Ny2

Ny1=(Ny-1)/2+1; Ny2=Ny-Ny1;

% First, place a 2-D computational grid.

x=linspace(0,L,Nx); dx=x(2)-x(1);
y1=linspace(-H1,0,Ny1); dy1=y1(2)-y1(1);
y2=linspace(0,H2,Ny2+1); dy2=y2(2)-y2(1);
y=[y1 y2(2:Ny2+1)];

% Form a 2-D regular mesh such that XG(i,j)=x(i), YG(i,j)=y(j)

[XG,YG]=form_2D_mesh(x,y);

% Compute value of f(x,y) at each grid point and make a filled contour plot

for p=1:Nx
   for q=1:Ny
      FG(p,q)=0.0;
   end;
end;

%figure; contourf(XG,YG,FG,min(Nx,Ny));colorbar;
%xlabel('x');ylabel('y');title('f(x,y)');

% allocate memory for the matrix and RHS vector

A=spalloc(Ntot,Ntot,5*Ntot); b=zeros(Ntot,1);

% we next specify equations for each boundary point.
%BC # 1

p=1;
for q=1:Ny
   n=get_label(p,q,Nx,Ny);
   A(n,n)=1; b(n)=0;
end;

%BC # 2

p=Nx;
for q=1:Ny
   n=get_label(p,q,Nx,Ny);
```

```
   A(n,n)=1; b(n)=0;
end;

%BC # 3

q=1;
for p=2:(Nx-1)
   n=get_label(p,q,Nx,Ny);
   A(n,n)=1; b(n)=0;
end;

%BC # 4

q=Ny;
for p=2:(Nx-1)
   n=get_label(p,q,Nx,Ny);
   A(n,n)=1; b(n)=0;
end;

% Setting the linear equation for the interior points - section one

factor_x1=a1/(dx^2); factor_y1=a1/(dy1^2);
factor_cent1=2*(factor_x1+factor_y1)+i*ome;
for p=2:(Nx-1)
   for q=2:(Ny1-1)
      n=get_label(p,q,Nx,Ny);
      A(n,n-Ny)=factor_x1+c1*YG(p,q)/(2*dx); A(n,n+Ny)=factor_x1-
c1*YG(p,q)/(2*dx);
      A(n,n-1)=factor_y1; A(n,n+1)=factor_y1;
      A(n,n)=-factor_cent1;b(n)=FG(p,q);
   end;
end;

% Setting the linear equation for the interface

rc1=rh1*cp1; rc2=rh2*cp2;    % the volume heat capacity
km=(k1+k2)/2;   % The average thermal conductivity of the composite at the interface
factor_xi=km/(dx^2); factor_yi=2/(dy1+dy2);
factor_centi=2*factor_xi+2*(dy1*k2+dy2*k1)/(dy1*dy2*(dy1+dy2))+i*ome*(rc1*dy1
+rc2*dy2)/(dy1+dy2);
q=Ny1;

for p=2:(Nx-1)
   n=get_label(p,q,Nx,Ny);
```

```
   A(n,n-Ny)=factor_xi; A(n,n+Ny)=factor_xi;
   A(n,n-1)=k1*factor_yi/dy1; A(n,n+1)=k2*factor_yi/dy2;
   A(n,n)=-factor_centi;b(n)=FG(p,q);
end;

% Setting the linear equation for the interior points - section two

factor_x2=a2/(dx^2); factor_y2=a2/(dy2^2);
factor_cent2=2*(factor_x2+factor_y2)+i*ome;

for p=2:(Nx-1)
   for q=(Ny1+1):Ny-1
      n=get_label(p,q,Nx,Ny);
      A(n,n-Ny)=factor_x2+c2*YG(p,q)/(2*dx); A(n,n+Ny)=factor_x2-
c2*YG(p,q)/(2*dx);
      A(n,n-1)=factor_y2; A(n,n+1)=factor_y2;
      A(n,n)=-factor_cent2;b(n)=FG(p,q);
   end;
end;

% Setting the heating elements -----This code needs to be generalized
% laterly.

q=Ny1-1; % Interior heating - 10 micron below the interface
hef=40; het=40; % hef - heating element front point; het - heating element trailing point

for p=hef:het
   n=get_label(p,q,Nx,Ny);
   b(n)=-q0;
end;

% Now we solve using Gaussian elimination

phi=A\b;

% We now extract the results of the calculation into the 2-D grid format
% and make a filled contour plot

PHIG=zeros(size(XG));
for p=1:Nx
   for q=1:Ny
      n=get_label(p,q,Nx,Ny);
      PHIG(p,q)=abs(phi(n));
   end;
```

```
end;
figure; MA=max(max(PHIG));MI=0.003*MA;LMA=log10(MA);LMI=log10(MI);
V=logspace(LMA,LMI,10);contour(XG,YG,PHIG,V);colorbar;%contour(XG,YG,PHI
G,min(Nx,Ny)); set('ShowText','on');

xlabel('x (m)');ylabel('y (m)');title('2D conjugate complex model: Temperature
magnitude T(x,y)');
figure;surf(XG,YG,PHIG);

% Get the phase shift and amplitude of temperature signal at the heating
% surface and the interface

qs=Ny1-1;qi=Ny1;qa=Ny1+1;%qs - phase in silicon dioxide; qi - phase at the interface;
qa - phase in air

for p=1:Nx
   n=get_label(p,qs,Nx,Ny);
   P_MS(p)=abs(phi(n));P_PS(p)=(180/pi)*angle(phi(n));
   n=get_label(p,qi,Nx,Ny);
   P_MI(p)=abs(phi(n));P_PI(p)=(180/pi)*angle(phi(n));
   n=get_label(p,qa,Nx,Ny);
   P_MA(p)=abs(phi(n));P_PA(p)=(180/pi)*angle(phi(n));
end;
dsd=10; dsf=hef-dsd;    dst=het+dsd;%dss -display distance; dsf -display front point; dst
-display trailing point
PS_Rs=P_PS(dsf:dst);PS_Ri=P_PI(dsf:dst); PS_Ra=P_PA(dsf:dst);XX=XG(dsf:dst,1);
MS_Rs=P_MS(dsf:dst);MS_Ri=P_MI(dsf:dst); MS_Ra=P_MA(dsf:dst);

figure; plot(XX,PS_Rs,'k');hold on;plot(XX,PS_Ri,'k--'); hold on;plot(XX,PS_Ra,'k-
.');hold off;
figure; plot(XX,MS_Rs,'k');hold on;plot(XX,MS_Ri,'k--'); hold on;plot(XX,MS_Ra,'k-
.');hold off;
xx=(XX*1e3)';

% save the results to a .mat file
%
%save Complex_2D_conjugate_FD.mat;
```